

**NUMERICAL STUDY OF TLD WITH AND WITHOUT  
SUBMERGED SCREEN**

**NUMERICAL INVESTIGATION  
OF  
SLOSHING MOTION INSIDE TUNED LIQUID DAMPERS  
WITH AND WITHOUT SUBMERGED SCREENS**

**By**

**MORTEZA MARIVANI, M.Sc, B.Sc**

**A Thesis**

**Submitted to the School of Graduate Studies**

**In Partial Fulfillment of the Requirements**

**for the Degree**

**Doctor of Philosophy**

**McMaster University**

**© Copyright by Morteza Marivani, August 2009**

Doctor of Philosophy (2009)

McMaster University

Department of Mechanical Engineering

Hamilton, Ontario

TITLE: Numerical Investigation of Sloshing Motion inside Tuned Liquid Dampers with  
and without Submerged Screens

AUTHOR: Morteza Marivani, B.Sc. (Sharif University of Technology), M.Sc. (Tarbiat  
Modarres University)

SUPERVISOR: Dr. Mohamed S. Hamed

NUMBER OF PAGES: xxiii, 150

## **Abstract**

A numerical algorithm has been developed to solve the sloshing motion of liquid in a Tuned Liquid Damper (TLD) outfitted by slat screens under large and random amplitude of excitation. It is based on the finite-difference method. The free surface has been reconstructed using volume of fluid method. Donor-acceptor technique has been used for tracking the volume fraction field. The effect of slat screen has been included and modeled using the partial cell treatment method.

The algorithm is an integrated fluid-structure model where the response of the structure is determined considering the effects of TLD. The structure is assumed as a single degree of freedom system (SDOF) and its response is calculated using the Duhamel integral method.

The algorithm has been validated against experimental data for the cases with and without screens. An excellent agreement was obtained between numerical and experimental results.

An extensive parametric study has been carried out investigating the effect of slat screens and screen pattern on the TLD performance and on the structure response. A new parameter termed as slat ratio was introduced to characterize the slat screens based on their pattern. Results indicated that screen pattern has a significant effect on the TLD performance and it could lead up to 33% reduction in structure response. It was found that decreasing the slat ratio will increase the damping effect of a TLD outfitted by slat screen.

The validity of the most commonly used approach, Baines and Peterson model, to calculate pressure drop of slat screens has been investigated. A correlation factor as a function of Reynolds number and solidity ratio of screen has been proposed to improve the results of this model. A new concept termed as effective solidity ratio has been proposed to account for the physical significant of screen pattern on TLD performance.

Keywords: Finite difference, Volume of fluid, Tuned liquid damper, Free surface, Sloshing motion, Deformation, Damping device, Slat screen.

**To my ever love, my wife, *Roshanak*  
And my lovely daughter, *Proshat***

## Acknowledgements

I wish to express my appreciation and sincere gratitude to my research supervisor, Dr. Mohamed S. Hamed. His valuable guidance, interest, support, and encouragement throughout the course of this thesis are greatly appreciated.

I would also like to express my appreciation to Dr. M. Lightstone, Dr. M. Tait, and Dr. P. Wood for their valuable comments and advice throughout the course of this research work. Special thanks go to Dr. Tait for providing valuable experimental results. This work was made possible by the facilities of the Shared Hierarchical Academic Research Computing Network (SHARCNET).

I would also like to express my sincere appreciation to Dr. R. Tavakoli at Sharif University of Technology for the fruitful discussions I had with him. His priceless support during the development stage of the algorithm is greatly acknowledged.

I would like to thank Dr. C.W. Hirt at Los Alamos National Laboratory, Dr. M. Bussman, and Dr. N. Ashgriz at University of Toronto, and Dr. L. Pengzhi at the Center for Applied Coastal Research.

I would like also to express my sincere thanks to all my colleagues and gratefulness for the friendships made during my time at McMaster. I would like to sincerely thank my close colleagues Salam Ali and Ramin Amid for their support and friendship. I would like also thank Hassan H. Morsy for his help during writing of my thesis.

Finally, I would like to thank my dear family, my wife and my daughter for their support and understanding. I am much indebted to my wife Roshanak for all her love, support, and patience during these years. Without any doubt, I could not have brought this work to this degree of completion without her sustained encouragement.

This thesis is dedicated to Roshanak for her understanding, sacrifice and support.

# Table of Contents

	<b>Page</b>
Abstract.....	iii
Acknowledgment .....	vi
Table of Content .....	vii
List of Tables.....	xi
List of Figures.....	xii
Nomenclature.....	xx
Chapter 1: Introduction and Literature Review	
1.1 Introduction.....	1
1.2 Classification of Structural Vibration Control Device .....	1
1.3 Tuned Liquid Damper.....	3
1.4 Applications of Tuned Liquid Dampers.....	6
1.5 Numerical Research on Tuned Liquid Dampers.....	8
1.6 Research Objectives.....	14
1.7 Organization of Thesis.....	15
Chapter 2: Mathematical Formulation	
2.1 Governing Equations and Boundary Conditions.....	17
2.2 Partial-Cell Treatment Method.....	20
2.3 Motion Equation of Structure.....	22
2.3.1 External Force.....	22

2.3.2	Earthquake Ground Motion.....	24
2.4	Fluid-Structure Interaction Model.....	26
Chapter 3: Numerical Algorithm		
3.1	Flow Chart of Algorithm .....	29
3.2	Discretization of the Governing Equations .....	32
3.3	Partial-Cell Treatment.....	36
3.4	Continuity Equation Approximation.....	37
3.5	Volume of Fluid Method.....	41
3.6	Velocity Boundary Conditions.....	47
3.6.1	Mesh Boundaries.....	47
3.6.2	Free Surface Boundaries.....	48
3.6.3	Internal Obstacle Boundaries.....	49
3.7	Conditions for Numerical Stability.....	49
3.8	Sloshing Force and Structure Response .....	50
Chapter 4: Validation of the Numerical Algorithm		
4.1	The Broken-Dam Problem.....	54
4.2	Sloshing Motion of Wave under the Effect of Gravity.....	57
4.3	Sloshing of Shallow Layer in a TLD.....	59
4.4	Sloshing of Shallow Layer in a TLD with a Slat Screen.....	62
4.5	TLD-Structure Interaction.....	66
Chapter 5: Numerical Results		
5.1	Introduction.....	74

5.2	TLD Performance without Screens .....	75
5.2.1	TLD Subjected to Harmonic Excitation .....	75
5.2.2	TLD Subjected to Random Excitation .....	80
5.3	Effect of Slat Screen on TLD Performance and Structure Response .....	83
5.3.1	TLD-Structure System Subjected to Harmonic Excitation .....	83
5.3.2	TLD-Structure System Subjected to Random Excitation .....	89
5.4	Effect of Number of Screens on TLD Performance and Structure Response .....	92
5.4.1	Case of Harmonic External Excitation .....	93
5.4.2	Case of Random External Excitation .....	98
5.5	Effect of Screen Pattern .....	101
5.5.1	Characteristic Dimension of Slat Screen .....	102
5.5.2	Effect of Screen Pattern on Flow Inside the TLD and on the Structure Response .....	102
5.5.2.1	Harmonic External Excitation .....	102
5.5.2.2	Random External Excitation .....	107
5.5.3	Effect of Screen Pattern on Pressure Drop through Screen .....	111
5.5.4	Proposed Modification to Baines and Peterson's Equation .....	123
5.5.5	Effect of Screen Pattern on Natural Frequency of the TLD .....	127
5.6	Determination of Effective Solidity Ratio .....	138
Chapter 6: Summary, Conclusions and Future work		
6.1	Summary and Conclusions .....	141

6.2 Future work .....	144
References.....	145
Vita.....	149

## List of Tables

<b>Table</b>	<b>Description</b>	<b>Page</b>
Table 4-1	Grid dependence test for the case of TLD with no screen.....	60
Table 4-2	Grid dependence test for the case of TLD with screen.....	63
Table 4-3	Structure properties.....	67
Table 4-4	TLD properties.....	67
Table 5-1	Different screen patterns at $S=0.4$ .....	113
Table 5-2	Different screen patterns at $S=0.5$ .....	113
Table 5-3	Different screen patterns at $S=0.6$ .....	113

## List of Figures

<b>Figure</b>	Description	<b>Page</b>
Figure 1-1	Schematic of a Tuned Mass Damper.....	2
Figure 1-2	Schematic of a Tuned Liquid Damper.....	3
Figure 1-3	Details of a slat screen .....	5
Figure 1-4	One King West building, Toronto, ON .....	7
Figure 2-1	Model Problem .....	17
Figure 2-2	Single degree of freedom structure for external force .....	22
Figure 2-3	Free body diagram for external force.....	23
Figure 2-4	Single degree of freedom structure for ground motion .....	25
Figure 2-5	Free body diagram for ground motion.....	25
Figure 2-6	Schematic of coupling between TLD and SDOF structure.....	27
Figure 2-7	Typical free surface during one period of sloshing.....	28
Figure 3-1	Finite difference mesh with variable rectangular mesh.....	29
Figure 3-2	Location of variables in a typical mesh cell.....	30
Figure 3-3	The flow char of the algorithm.....	32
Figure 3-4	A computational Cell.....	34
Figure 3-5	Partial flow factor for an obstacle cell .....	37
Figure 3-6	Geometric parameters of a surface cell.....	40
Figure 3-7	Donor-acceptor cell configuration.....	42
Figure 3-8	Example of free surface shapes during the advection of F.....	44

Figure 3-9	Boundary condition near the left wall .....	47
Figure 3-10	Boundary condition on free surface.....	48
Figure 4-1	The layout of the broken dam problem.....	54
Figure 4-2	Horizontal position of free surface as function of time versus experimental data.....	55
Figure 4-3	Vertical position of the free surface as function of time versus experimental data.....	56
Figure 4-4	Free surface profile at various times.....	56
Figure 4-5	Initial geometry of the sloshing problem.....	57
Figure 4-6	Position of the interface at the left boundary as a function of time.....	58
Figure 4-7	Development of the free surface during the first period of the sloshing motion.....	59
Figure 4-8	Model Problem .....	59
Figure 4-9	Surface deformations at a location 5% of tank length from the left wall (i.e., $x = 0.0483$ m) compare with experimental data reported in [57] .....	61
Figure 4-10	The forced sinusoidal excitation used for code validation compared with the real excitation used in the experiment reported in [57] .....	61
Figure 4-11	Slat screen layout.....	62
Figure 4-12	Comparison between measured [57] and predicted surface	

	deformations at $x = 0.0483$ m for the cases of the TLD without and with a screen .....	64
Figure 4-13	Comparison between measured [57] and predicted surface deformations at $x = 0.0483$ m for the case of the TLD with a screen.....	64
Figure 4-14	Details of the flow through the screen at various times.....	65
Figure 4-15	Schematic of TLD-Structure Model.....	66
Figure 4-16	Schematic of TLD used in the experiment [57].....	67
Figure 4-17	Tank set-up side view [57].....	67
Figure 4-18	Damping screen [57].....	68
Figure 4-19	External excitation function [57].....	68
Figure 4-20	Comparison of experimental [57] and numerical time histories of free surface response at $x=0.0483$ m .....	69
Figure 4-21	Comparison of experimental [57]and numerical normalized TLD force.....	69
Figure 4-22	Comparison of experimental and numerical structural acceleration time histories.....	70
Figure 4-23	Variation of the normalized sloshing force $F$ , as function of excitation frequency ratio .....	72
Figure 4-24	Variation of the normalized sloshing force $F$ , as function of excitation frequency ratio.....	73
Figure 5-1	The TLD configuration .....	75

Figure 5-2	The response of the structure with and without the TLD .....	76
Figure 5-3	The time history of sloshing force ( $F_{TLD}$ ) and excitation force ( $F_e$ ) .....	76
Figure 5-4	Time history of the free surface deflection at $x = 0.05 \times L$ .....	77
Figure 5-5	Free surface profile in TLD at selected times which fluid height at the left side is maximum .....	78
Figure 5-6	Free surface profile and streamlines showing the flow pattern at different times .....	79
Figure 5-7	The response of the structure with and without TLD for random excitation .....	80
Figure 5-8	Time history of (a) the free surface deflection at $x=0.05 \times L$ and (b) the sloshing force .....	81
Figure 5-9	Free surface profile and streamlines showing the flow pattern at different times .....	82
Figure 5-10	The screen configuration and its location .....	84
Figure 5-11	Comparison of time history of the free surface deflection at $x=0.05 \times L$ in the TLD with and without screen.....	85
Figure 5-12	Comparison of the time history of (a) the resultant force and (b) the structure deflection for the cases of with and without screen.....	86
Figure 5-13	Comparison of the time history of the structure deflection with TLD outfitted by one screen at the middle and without a TLD..	87

Figure 5-14	The flow field inside the TLD for the cases of (a) without and (b) with a slat screen at $t=26.2$ s, $36.7$ s & $37.7$ s. The TLD-Structure is subjected to harmonic excitation.....	88
Figure 5-15	Comparison of time history of the free surface deflection in the TLD with and without screen.....	89
Figure 5-16	The time history of structure response under random excitation for the case of using a TLD with and without screen .....	90
Figure 5-17	The flow field inside the TLD for the cases of (a) without and (b) with a slat screen at $t=29.54$ s & $46.36$ s. The TLD-Structure is subjected to random excitation.....	91
Figure 5-18	Locations of two screens placed in the TLD .....	93
Figure 5-19	Comparison of time history of the free surface deflection at $x=0.0483$ m in a TLD with one and two screens.....	94
Figure 5-20	Comparison of time history of structure deflection in the cases of TLD with one and two screens.....	94
Figure 5-21	Comparison of time history of sloshing force for the cases of TLD with one and two screens.....	95
Figure 5-22	Comparison of time history of resultant force for the cases of TLD with one and two screens.....	96
Figure 5-23	The flow field inside the TLD for the cases of with (a) two screen and (b) one screen at $t=20.1$ s & $23.8$ s .....	97
Figure 5-24	Comparison of time history of the free surface deflection at	

	$x=0.0483\text{m}$ in the case of TLD with one and two screens.....	98
Figure 5-25	Comparison of time history of the sloshing force in the case of TLD with one and two screens.....	98
Figure 5-26	Comparison of time history of the structure deflection in the case of TLD with one and two screens.....	99
Figure 5-27	The flow field inside the TLD for the cases of with (a) two screen and (b) one screen at $t=15\text{ s}$ & $21\text{ s}$ & $42.6\text{ s}$ .....	100
Figure 5-28	Characteristic dimensions of the slat screen .....	102
Figure 5-29	Location of the two slat screens having the same solidity ratio and different slat ratio .....	103
Figure 5-30	Effect of SR on flow pattern inside a TLD subjected to a harmonic excitation.....	104
Figure 5-31	Effect of SR on deformation of free surface at $x=0.0483\text{m}$ .....	105
Figure 5-32	Effect of SR on the sloshing force inside the TLD.....	105
Figure 5-33	Effect of SR on structure response.....	106
Figure 5-34	Effect of SR on structure acceleration.....	107
Figure 5-35	Effect of SR on free surface deformation at $x=0.0483\text{m}$ .....	108
Figure 5-36	Comparison of flow pattern around the slat screens.....	108
Figure 5-37	Effect of SR on sloshing force inside the TLD.....	109
Figure 5-38	Effect of SR on structure response.....	110
Figure 5-39	Effect of SR on the acceleration of the structure.....	111
Figure 5-40	Time history of pressure drop for different solidity ratios and	

	D=4mm .....	114
Figure 5-41	Time history of averaged velocity at the screen location for different solidity ratios and D=12mm .....	115
Figure 5-42	Free surface profile at t=59s for (a) S=0.4, SR=0.25 and (b) S=0.6, SR=0.167.....	115
Figure 5-43	Variation of the maximum pressure drop through screen with time using various solidity ratios .....	117
Figure 5-44	Vorticity field for the case of S=0.5, D=5 mm (SR=0.0833).....	118
Figure 5-45	Vorticity field for the case of S=0.5 and D=30 mm (SR=0.5) ...	119
Figure 5-46	Vorticity field for S=0.4.....	120
Figure 5-47	Vorticity field for S=0.5.....	121
Figure 5-48	Vorticity field for S=0.6.....	122
Figure 5-49	Pressure ratio curve for different solidity ratios .....	123
Figure 5-50	Pressure ratio scaled curve for different solidity ratios.....	124
Figure 5-51	Comparison of the values of $C_m$ determined from algorithm and the proposed correlation at different S and SR, (a) S=0.4 , (b) S=0.5 , (c) S=0.6 .....	125
Figure 5-52	Comparison of the values of $C_m$ determined from algorithm and the proposed correlation at different amplitudes and S (a) S=0.4 , (b) S=0.5 , (c) S=0.6 .....	126
Figure 5-53	Configuration of slat screens used in the frequency sweep analysis .....	129

Figure 5-54	Variation of the maximum free surface deflection at $x=48.3$ mm as a function of frequency of external excitation for a TLD equipped with one screen having the same $S$ and two different slat ratios.....	129
Figure 5-55	Flow pattern around the screen with $S=0.42$ , (a) $D=25$ mm & (b) $D=10$ mm at $t= 25$ s.....	130
Figure 5-56	Sloshing force at different frequencies for the case of screen with $D=10$ mm .....	131
Figure 5-57	Flow patterns around two screens with the same solidity ratio and different slat ratios (a) $D=25$ mm and $SR=0.5$ , (b) $D=20$ mm, $SR=0.2$ .....	133
Figure 5-58	Effect of $SR$ on the average velocity at the screen for $f=0.54$ Hz and $A=2.5$ mm .....	134
Figure 5-59	Effect of screen pattern on free surface deflection at $x=48.3$ mm	134
Figure 5-60	Effect of screen pattern on sloshing force for $f=0.54$ Hz and $A=2.5$ mm .....	135
Figure 5-61	Flow patterns around the screen with $S=0.42$ and $D=10$ mm at different times .....	136
Figure 5-62	Flow patterns around the screen with $S=0.42$ and $D=25$ mm at different times .....	137
Figure 5-63	Effective solidity ratio as function of slat height for a TLD equipped with one screen placed in the middle .....	139

## Nomenclature

### List of Symbols

A	Amplitude of external dynamic excitation, m
$A_S$	Total area of solid in a slat screen, $m^2$
$A_t$	Total projected area of a slat screen, $m^2$
c	Damping coefficient of TLD (or TMD), kg/s
$C_S$	Damping coefficient of structure, kg/s
$C_C$	Contraction factor
$C_m$	Correlation factor
d	Distance between free surface and center of the neighbor fluid cell
$d_C$	Distance between the center of the free surface cell and the center of the neighbor fluid
dh	Deflection of free surface relative to the height of the initial flat free surface, m
D	Slat height, mm
$D_0$	Distance between two adjacent slats, mm
$D_t$	Distance of last slat from free surface, mm
$D_b$	Distance of first slat from tank bottom, mm
F	Volume of fluid per unit volume of cell (i,j)
$F_e$	External excitation force, N
FUX	Convective term of the u in the x- direction
FUY	Convective term of the u in the y- direction

FVX	Convective term of the v in the x- direction
FVY	Convective term of the v in the y- direction
$F_{TLD}$	Sloshing force, N
$F'$	Normalized sloshing force
$f_w$	Natural frequency of TLD, Hz
f	Excitation frequency of TLD, Hz
$g_x$	Horizontal acceleration, $m/s^2$
$g_y$	Gravitational acceleration, $m/s^2$
h	Height of the initial flat free surface, m
k	Stiffness coefficient of TMD, N/m
$K_S$	Stiffness coefficient of structure, N/m
L	Length of tank, m
$L_v$	Irrotational length, mm
m	Mass of TLD ( or TMD), kg
$M_S$	Mass of structure, kg
$N_S$	Number of slats
p	Pressure, Pa
P	Total momentum of fluid, kg.m/s
Re	Reynolds number, = $U_c D_o / \nu$
S	Solidity ratio, = $A_S / A_t$
$S_S$	Total solid height of the slat screen, mm
SR	Slat ratio, = $D / S_S$

$S_{\text{eff}}$	Effective solidity ratio, = $S_{\text{add}} + S_{\text{phys}}$
$S_{\text{add}}$	Additional solidity ratio
$S_{\text{phys}}$	Physical solidity ratio
$t$	Time, s
$u, v$	Velocity components in the horizontal and vertical directions, respectively
$U_C$	Characteristic velocity, m/s
$U_S$	Velocity at screen, m/s
VISX	Diffusion term of $u$ in the $x$ - direction
VISY	Diffusion term of the $v$ in the $y$ - direction
$x, y$	Cartesian coordinates

### Greek symbols

$\eta$	Distance coefficient factor, = $d_C / d$
$\rho$	Density, $\text{kg/m}^3$
$\nu$	Kinematics viscosity, $\text{m}^2/\text{s}$
$\mu$	Mass ratio, = $m / M_S$
$\beta$	Pressure correction coefficient
$\varepsilon$	Convergence criteria
$\alpha$	Upwind fraction factor
$\tau_{ij}$	Shear stress, $\text{N/m}^2$
$\sigma$	Surface tension, $\text{N/m}$
$\theta$	Partial flow factor

- $\varphi$  Phase angle, rad/s
- $\omega_r$  Relaxation parameter
- $\omega_n$  Natural frequency of structure, rad/s
- $\omega_D$  Damped frequency of structure, rad/s
- $\omega$  Frequency of excitation, rad/s
- $\kappa$  Local free surface curvature
- $\xi$  Damping ratio
- $\beta_w$  Excitation frequency ratio

## **Chapter 1: Introduction and Literature Review**

### **1.1 Introduction**

In recent years, the construction of the lightly damped, flexible tall structures has magnified their sensitivity to dynamic excitations and has created concern in the structural engineering community. Large structures are frequently exposed to severe dynamic loading from several sources such as earthquakes and high speed winds. The ability to damp the response of structures to external excitations, and consequently maintain their integrity and ensure human comfort, is one of the important objectives that engineers strive to achieve today.

### **1.2 Classification of Structural Vibration Control Devices**

Structural vibration control devices are often classified into three main categories, namely: active, semi-active, and passive, based on their power requirements (Soong and Dargush, 1997). Active control systems require external power supply to exert a control force determined according to the feedback from the structural motion. Passive vibration control systems require no external power supply to operate. They depend on energy absorbing materials and elements to mitigate the vibration. Passive systems include visco-elastic dampers, chain dampers, tuned mass dampers and tuned liquid dampers. Semi-active control systems have external power requirement that are orders of magnitude less than the typical power requirement of active systems and are often viewed as controllable passive systems.

The simplicity, stability, low cost, and reliability of passive control systems have made them the method of choice for structural motion control. The basic function of the passive damping control systems is to absorb or consume a portion of the input energy of the external excitation such as wind or earthquake excitations. Therefore, the energy dissipation demand of the primary structure decreases.

The family of passive damping devices which limit the dynamic response through modifying the frequency response of a structure are called dynamic vibration absorbers (DVA). The most commonly used passive DVA is the tuned mass damper (Kareem and Kijewski 1999). A simple tuned mass damper (TMD) consists of a mass, a spring, and a dashpot. The system is designed such that it resonates at a frequency near the natural modal frequency of the primary structure, see figure 1-1. The resulting inertial forces which are developed by the mass of the TMD ( $m$ ) are approximately anti-phase with the external forces and thus they reduce the structural motion.

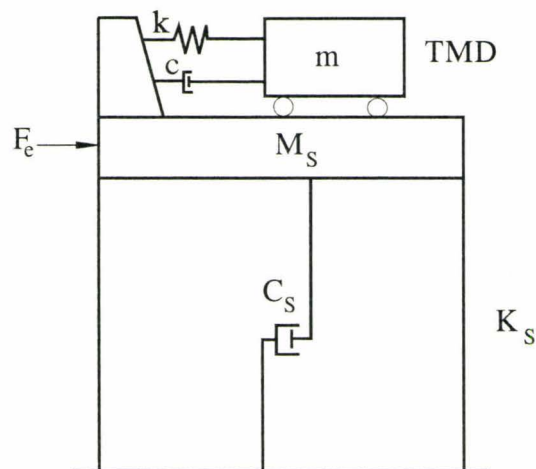


**Figure 1-1: Schematic of a Tuned Mass Damper (TMD), ( $m, k, c$ ), attached to a structure, ( $M_s, K_s, C_s$ ), exposed to an external force  $F_e$ .**

### 1.3 Tuned Liquid Dampers

A tuned liquid damper (TLD) has operating principles very similar to a tuned mass damper. A TLD is a tank partially filled with a liquid, such that due to the external excitation, the liquid sloshes inside the tank. The liquid, which is often water, acts as the mass, spring, and dashpot, as shown in figure 1-2. In the same way, the liquid motion imparts inertia forces approximately anti-phase to the external dynamic forces, thereby reducing structural motion. As such, the attachment of TLDs modifies the frequency response of the structure in a way similar to increasing the structure effective damping.

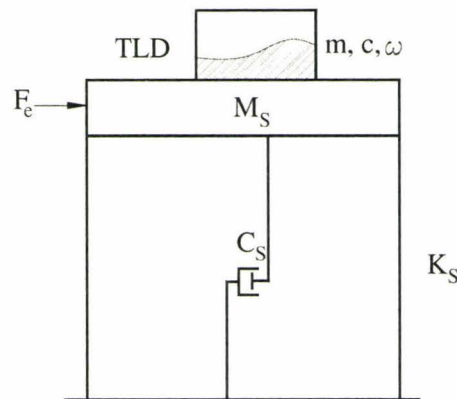


**Figure 1-2: Schematic of Tuned Liquid Damper (TLD), ( $m, c, \omega$ ), attached to a structure, ( $M_s, K_s, C_s$ ), exposed to an external force  $F_e$ .**

The use of TLDs has increased due to their many advantages over other conventional damping devices. TLDs can be used for both small (wind) and large amplitude (earthquake) vibrations. They are easy to install to existing structures, and do not require high maintenance and operating cost. Moreover, TLDs can be used as water tanks for the building, either to be used for regular water supply or water supply for fire

emergencies. TLDs were used to stabilize marine vessels against rocking and rolling motions (Matsuuara et al., 1986), offshore platforms (Vandiver and Mitone, 1978; Lee and Reddy, 1982), and to stabilize tall structures (Kareem and Sun, 1987; Noji et al., 1988; Fujii et al., 1990; Wakahara et al., 1992; Wakahara 1993; Reed et al., 1998, Tait et al., 2005). Although the construction of a TLD is simple, the liquid sloshing motion inside a TLD has a highly nonlinear and complex nature. The free surface slopes can approach infinity and the liquid may encounter the top cover in case of enclosed tanks. Since the main mechanism of damping in a TLD is based on the sloshing motion of the fluid, the sloshing motion must be well understood. The complexity of the sloshing motion is due to the fact that it depends on the interaction of various parameters.

The design parameters of a TLD are:

1. The mass ratio, defined as the ratio of the effective mass of the liquid to the generalized mass of the structure.
2. The natural frequency of the liquid sloshing motion, and
3. The inherent damping of the TLD.

Typically the values of the mass ratio (liquid mass/structure mass) for tall structures range approximately between 1% and 5%. The higher the mass ratio, the more force is generated by the sloshing fluid. The upper limit of the mass ratio is because of practical limitations. TLDs are installed in buildings with limited space and weight availabilities, and they should be designed with that in mind. The TLD is tuned such that its natural frequency of sloshing almost matches the natural frequency of the structure's vibration mode of interest. The optimum inherent damping corresponds to typical

damping ratios in the range between 5% and 15%. The main source of damping in TLDs without additional damping devices is due to viscous dissipation in the boundary layer at the walls and the bottom of the tank, and from free surface contamination. The inherent damping of a TLD without additional damping devices is usually significantly less than the optimal value. Moreover, the response of an under-damped TLD is more non-uniform, less controllable and less predictable. Using higher viscosity liquids, such as oil, is not common because of cost and environmental concerns and also because TLDs are usually, as mentioned before, used as water storage tanks.

Several approaches have been applied to increase the inherent damping of TLDs by using roughed elements (Fujino et al., 1988), surface contaminants (Tamura et al, 1995) and nets or screens (Noji et al., 1988; Warnitchai and Pinkaew, 1998; Kaneko and Ishikawa, 1999; Tait 2004; Hamelin and Tait 2007). Considerable attention has been given recently to the use of slat screens in TLDs (Tait et al., 2005; Hamelin 2007). A slat screen consists of horizontal slats spaced apart uniformly. Figure 1-3 shows a schematic of a typical slat screen.

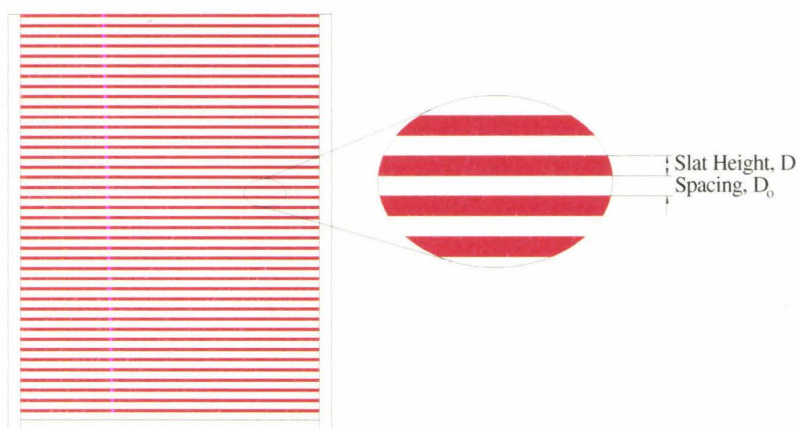


**Figure 1-3: Details of a slat screen.**

The reason for selecting slat screens as additional damping devices is that their installation in a TLD is simple and their damping characteristics could be easily changed during operation, by simply varying the spacing between the slats. This flexibility gives one the ability to change a TLD from being a passive damping device to a semi-active damping device, and to vary the amount of damping of a TLD based on the value of the external excitation force. It has also been shown (Warnitchai and Pinkaew, 1998) that screens are effective in both small and large amplitude excitations. It has been recently reported experimentally that the amount of damping can be changed by changing the slat height and spacing (Hamelin 2007).

## **1.4 Application of Tuned Liquid Dampers**

TLDs have been used in numerous structures around the world and have been proven to be very effective. Nagasaki Airport Tower was constructed in 1974, and in 1987 the effect of a TLD on the response of this tower was investigated. A set of 25 cylindrical vessels containing water were installed on the tower. It was found that without the TLDs the structure had a damping ratio of 0.93%. When the number of vessels increased from 7, 14, 19 to 25 the amount of damping was 2.2%, 3.1%, 4.1% to 4.7%. (Tamura et al., 1995)

The Yokohama Marine Tower is another structure which was equipped with a TLD. It was found that the damping ratio of this structure with a TLD was seven times larger than its damping without a TLD (Tamura et al., 1995). Shin-Yokohama Prince Hotel is another structure which was equipped with a TLD, in which case a 50%

reduction in the acceleration was obtained. There are examples where a large number of tanks were installed to act as TLDs, like the case of the Tokyo International Airport Tower with a height of 77.6 m. A total of 1400 tanks containing water and floating particles were installed on this tower. The TLD increased the average damping ratio of this structure from 1.2% to 7.6% (Tamura et al., 1995).

The most recent application of TLDs in Canada is on the One King West building in Toronto, Ontario, shown in figure 1-4. This is a newly constructed residential-commercial building built in downtown Toronto. The 51-storey structure is the most slender structure in the world with an aspect ratio (length to width) of 11:1. It is considered as the tallest residential building in Canada [18]. Two insulated concrete TLDs equipped with damping screens have been installed on the 51<sup>st</sup> floor of this building.

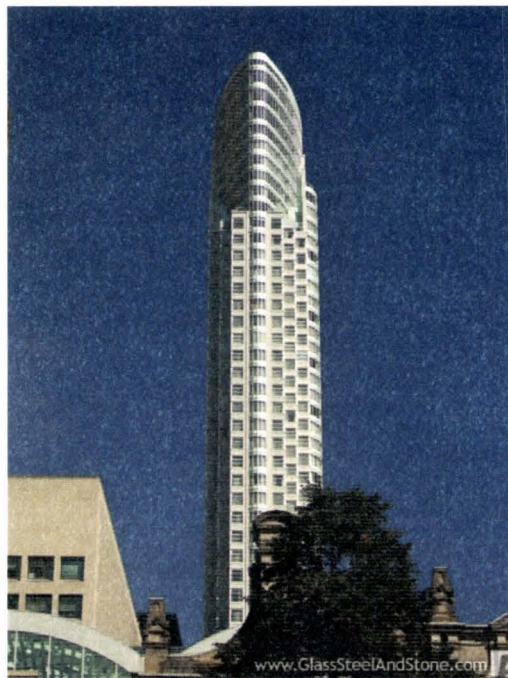


**Figure 1-4: One King West building, Toronto, Ontario, Canada.**

## 1.5 Past Efforts in TLD Research

As mentioned before, the liquid sloshing motion inside the TLD has a nonlinear behavior, especially under large amplitudes of excitation. The free surface can fold and merge (wave breaking) depending on the amplitude of the sloshing motion, which leads to highly unpredictable patterns of motion. Many factors contribute to the amplitude of the sloshing motion inside the tank. It depends on the external excitation, its nature, and its frequency. It also depends on the TLD design, i.e. on the geometry of the tank, the depth of the liquid layer, and the properties of the contained liquid (Koh et al., 1994; Celebi and Akyildiz, 2002).

The sloshing behavior of liquids in TLDs subjected to external dynamic excitations has been studied extensively through numerous experimental investigations. Chester (1968) carried out a series of experiments in order to validate the analytical theory for sloshing motion of liquid under very small amplitude of sloshing. Earthquake response behavior of ground-supported liquid storage tanks was studied experimentally by Clough et al. (1978). Fujii et al. (1990) studied the effect of a tuned sloshing damper on the response of two actual tall towers (Nagasaki airport tower and Yokohama marine tower) under wind-induced vibrations. They found the reduced vibration levels after installation of TLDs were in the range acceptable from the view point of comfort and serviceability. Sun et al. (1995) studied experimentally liquid motions in shallow liquid dampers (TLDs). In their study, liquid motions were investigated in TLDs with different tank shapes and different liquid viscosities and the complex non-linear characteristics were observed. Reed et al. (1998) investigated dissipation of energy of rectangular tuned

liquid dampers under large amplitude of excitations. Tait and El Damatty (2005) carried out extensive experimental research on the performance of tuned liquid dampers with and without submerged slat screens under a wide range of external excitations. Hamelin (2007) revealed experimentally the importance of the pattern of slat screen on the damping ratio of TLDs.

Numerical modeling has also been used to investigate the sloshing behavior of liquids in tanks. Most of these investigations have been carried out by using simplified linear theories that are applicable only to small interfacial deformations.

Potential-flow theory, which considers inviscid, irrotational flows, has been widely used by many researchers (Nakayama and Washizu, 1981; Nakayama, 1983; Ohyama and Fujii, 1989; Tosaka and Sugino, 1991; Chen et al., 1996; Warnitchai and Pinkaew, 1998; Dutta and Laha, 2000). This theory does not account for the effect of fluid properties on the sloshing motion. It also can not be used to model the flow field around any obstacles inside the TLD, because such solid obstacles act as bluff bodies and create vortices during the sloshing which can not captured by an irrotational flow model.

Shallow-water wave theory has also been applied by other researches (Shimizu and Hayama, 1987; Sun L.M., 1991; Reed et al., 1998; Kenko S. and Ishikawa M., 1999; Tait et al. 2005). In these investigations, the wave height or the amplitude of the interfacial deformation was assumed to be small compared to the mean depth of the liquid layer, and the horizontal velocity was assumed uniform throughout the liquid layer. This theory can not be used to model the flow field around and obstacles inside the TLD. A number of studies (Sun et al., 1989; Fujino et al., 1992; Sun and Fujino, 1994; Sun et

al., 1995) combined the shallow-water theory with the boundary layer theory, where the effect of liquid viscosity was considered only within boundary layer. Improvements over the predictions of the potential-flow theory were achieved by Zang et al. (2000) who solved a linearized form of the Navier-Stokes equations by neglecting the convective acceleration terms. They indicated that liquid viscosity has an important effect on the sloshing motion near rigid walls, especially under excitation frequencies near resonance.

As indicated previously, the linear theory is applicable only when the amplitude of the interfacial deformations are small. This is valid in cases of the external excitations have small amplitudes or have a frequency of excitation away from the natural frequency of the TLD. Consequently, when the excitation frequency is near the natural frequency of the TLD, or the excitation amplitude is high, the linear theory is inadequate (Lepelletier and Raichlen, 1988).

A TLD is usually designed to operate at or near the natural frequency of the structure in order to maximize the absorbed and dissipated energy, and thus maximize the benefit of the use of the TLD. In order for a numerical model to predict accurately the sloshing motion inside a TLD, the numerical model should: (1) Account for all physical effects (inertia and viscosity), and (2) It should be able to solve the moving boundary problem while allowing for all conditions leading to small to large interfacial deformations. In this case, not only the transport of the momentum and mass are coupled but also the formation, evolution, and the dynamics of the interface play a major role in defining the system response. Actually, the main difficulty in solving such a moving-boundary problem is in the determination of the location of the liquid free surface as an

integrated part of the solution of the system of equations governing the fluid flow problem.

Algorithms for moving-boundary problems were reviewed by Floryan and Rasmussen (1989). These algorithms track the moving free surface either by using fixed grids (Eulerian scheme), adaptive grids (Lagrangian scheme), or by applying analytical mapping techniques.

The Lagrangian scheme (Ramaswamy et al., 1986; Bellet and Chenot, 1993; Thé et al., 1994) is characterized by the mesh system which moves or deforms as the calculation proceeds. The mesh boundaries coincide with the free surface, and thus the free surface can be represented with accuracy. However, overly distorted meshes due to a change of fluid domain may result in numerical errors. Therefore, the Lagrangian scheme can not be used to handle large deformation of the free surface as is expected at the sloshing motion of liquid in TLDs, operating at their natural frequencies. Only problems with gentle surface variations were considered using this scheme.

Yamamoto and Kawahara (1999) solved the Navier-Stokes equations in the form of arbitrary Lagrangian-Eulerian (ALE) formulation. In the ALE method, the remeshing technique has been used to maintain the computational stability. The remeshing means at every computational step, a new finite element mesh is reformed. To compute a large amplitude-sloshing problem, computation often tends to be unstable in this technique because of the unevenness of nodal points formed on the free surface. The smoothing technique was introduced using a smoothing factor, which was introduced in order to reduce the instability. Finding a proper value for this factor is the major issue of this

technique because it is very difficult to choose a unique constant for the entire of computation.

Hamed and Floryan (1998) and Siddique et al. (2004) applied the analytical mapping technique for modeling of moving boundary at the free surface. In this approach, an analytical mapping function, which was determined as part of the solution, was used to transfer the irregular physical domain to a rectangular computational domain. The main limitation to finding the mapping function was to assume continuity of the free surface which is not a valid assumption in the case of having a submerged screen in TLDs. Although this approach was successful in dealing with fairly large free surface deformations, it could not be used to resolve the details of the flow through submerged screens due to surface discontinuities.

In Eulerian schemes (Torrey et al., 1986; Poo and Ashgriz, 1990; Koth et al., 1994; Rudman, 1997; Scardovelli and Zaleski, 1999; Tavakoli et al. 2006), computational meshes are generated beforehand and fixed during the entire computation. Therefore, it is free of difficulties due to the deformation of the meshes. However, special treatment is necessary to track the moving free surface as the motion of fluid does not coincide with the calculation mesh. The Marker And Cell (MAC) method (Harlow and Welch, 1965; Chan and Street, 1970; Lemos, 1992) follows the moving free surface by tracking the movement of imaginary markers. Eulerian fluid properties required to solve Navier-Stokes equations, are retrieved from the instantaneous positions of the marker particles. This method is computationally expensive. Moreover, difficulties arise when the interface stretches considerably which requires the addition of fresh marker particles during the

flow simulation. In the Volume of Fluid method (Hirt and Nichols, 1981; Nichols et al., 1985; Reed et al., 1994; Koth et al., 1996; Lin et al., 1997; Rider, 1998; Bassman, 2000; Min Soo Kim, 2003; Babaei et al., 2006, Lin, 2007) the cell volume fraction is used to transport the interface of free surfaces. This method has the ability to handle large surface deformations and surface folding and merging which is expected for free surface motion in TLDs operating in their natural frequencies. The volume of fluid (VOF) method is also much easier to use and less computationally intensive.

For modeling of submerged screens in TLDs, Kaneko et al. (1999) and Tait et al. (2005) used a nonlinear model based on the shallow water wave theory to simulate sloshing motion in a TLD outfitted by damping screens. In these works, liquid was assumed to be inviscid and incompressible, and the flow was assumed as irrotational. The screen was modeled as a hydraulic resistance with the pressure drop calculated by an equation developed by Baines and Peterson (1951). Having irrotational flow through the screen was the main assumption of this equation which is not valid in a wide range of applications. This approach accounts for the effect of screen solidity, however, it does not account for the effect of screen pattern, and hence it does not provide any details of the flow through the screen. The effect of screen pattern has been recently studied by Hamelin (2007) and found to have an important effect on the amount of damping and the natural frequency of the TLD.

Although it has been shown that screens could play a major role in improving the performance of TLDs, (Warnitchai and Pinkaew, 1998; Tait, 2004; Tait et al., 2005 Hamelin, 2007), no numerical effort has been reported to consider the proper influence of

screen on the sloshing motion of liquid in TLDs and structure response for the large excitation amplitudes.

## 1.6 Research Objectives

The main objectives of this research are:

- i. To develop an integrated fluid-structure numerical algorithm to simulate the sloshing motion of water in TLDs with and without screens considering a wide range of excitations, from low amplitudes (wind) to high amplitudes (earthquakes) and to calculate the response of the structure under the effect of the TLD. Most of the previous research was limited to small amplitude sloshing in TLDs.
- ii. To understand the characteristics of the flow through screens by resolving the flow field around them. None of the numerical researches on TLD could account for the proper effect of screens on the performance of TLD.
- iii. To investigate the effect of screen pattern on the TLD performance and on structural response.
- iv. To propose a new correlation accounting for the effect of screen pattern on pressure drop due to the screen and modify Baines and Peterson equation. This equation has been used extensively in all of the numerical researches on TLD outfitted with a submerged screen. It was important to investigate the validity of this equation and obtain a correction factor to extend its validity range.

## 1.7 Organization of Thesis

Chapter 2 describes the physical sloshing problem, the mathematical formulation, and the complete set of boundary conditions. The method of partial cell treatment for modeling the screen is presented. The chapter also includes the description and derivation of the equation of motion of the structure under external forces and ground motion. The interaction of the fluid model and the structure model is discussed and the method of calculating sloshing force is explained at the end of this chapter.

In chapter 3 the complete numerical scheme is presented. A schematic of the computational domain with the discretized form of the governing equations in the presence of the partial cell treatment method is presented. The volume of fluid method and the donor and acceptor algorithm are discussed in full detail. An iterative process to calculate the pressure field is described and the numerical stability conditions are presented. The full computational procedure and the flow chart for the entire numerical algorithm is also presented in this chapter.

Chapter 4 presents several problems used to validate the numerical algorithm. In this chapter numerical results of algorithm for each case have been compared to experimental results.

Chapter 5 presents the numerical results of the carried out analyses. It starts with the effect of TLD (with no screens) on the structure's response under both random and harmonic excitations. Then the effect of a slat screen on the performance of the TLD and structure response is investigated. The effect of the number of screens is studied by adding another screen into the TLD. Then the screen characteristic parameters are

introduced and the effect of screen pattern on TLD performance and structure response is illustrated. In this chapter the limitations of the previous mathematical model for calculation of pressure drop at slat screens are explained. Subsequently, a new correction factor, as a function of Reynolds number and solidity ratio, is presented. Finally the effect of screen pattern on the natural frequency of the TLD was studied and the concept of “Effective Solidity Ratio” is presented.

Chapter 6 presents the summary and conclusions of this research. It also presents future work.

## Chapter 2: Mathematical Formulations

The TLD considered in this study is a rigid rectangular tank of width  $L$  and height  $H$  filled with water to a stationary depth  $h$ , as shown in figure 2-1. The coordinate system is attached to the tank with the origin located at the bottom left corner. The tank is subjected to a general external excitation in the horizontal ( $x$ ) direction, defined as a source term ( $g_x$ ) in the momentum equation in ( $x$ ) direction. By neglecting the end effects, the motion of the liquid inside the tank can be assumed two-dimensional in the  $x$ - $y$  directions. Geometrical details of the slat screen considered in this work have been shown in figure 1-3. The screen consists of horizontal slats uniformly spaced. The advantage of this type of screens is that the required optimal damping can be easily adjusted by changing screen pattern (i.e., by changing slat height and/or slat spacing).

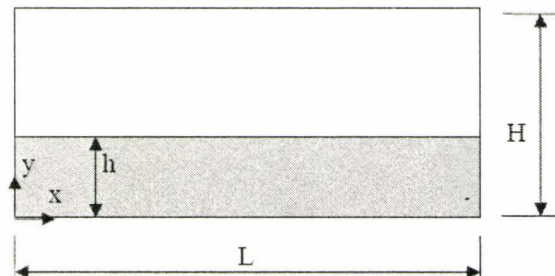


Figure 2-1: Model Problem –  $h$  is the fluid height,  $H$  is the tank height,  $L$  is the tank length.

### 2.1 Governing Equations and Boundary Conditions

The two dimensional, incompressible free surface fluid flow problem has been modeled using an Eulerian frame of reference [26; 28; 30; 63]. The fixed points  $\vec{x}$  in the domain ( $\vec{x} = x\hat{i} + y\hat{j}$ ) are described using Cartesian coordinates. The velocity field  $\vec{V}$  is

function of space and time, i.e. ,

$$\vec{V} = u(x, y, t)\hat{i} + v(x, y, t)\hat{j}$$

The governing equations of the incompressible, Newtonian, laminar flow in the Cartesian coordinate system shown in figure 2-1 are the following continuity and momentum equations:

$$\frac{\partial u}{\partial x} + \frac{\partial v}{\partial y} = 0 \quad (2.1)$$

$$\frac{\partial u}{\partial t} + u \frac{\partial u}{\partial x} + v \frac{\partial u}{\partial y} = -\frac{1}{\rho} \frac{\partial p}{\partial x} + g_x + \frac{1}{\rho} \frac{\partial \tau_{xx}}{\partial x} + \frac{1}{\rho} \frac{\partial \tau_{xy}}{\partial x} \quad (2.2)$$

$$\frac{\partial v}{\partial t} + u \frac{\partial v}{\partial x} + v \frac{\partial v}{\partial y} = -\frac{1}{\rho} \frac{\partial p}{\partial y} + g_y + \frac{1}{\rho} \frac{\partial \tau_{yy}}{\partial y} + \frac{1}{\rho} \frac{\partial \tau_{xy}}{\partial y} \quad (2.3)$$

The time evolution of liquid region is computed solving the following equation,

$$\frac{\partial F}{\partial t} + u \frac{\partial F}{\partial x} + v \frac{\partial F}{\partial y} = 0 \quad (2.4)$$

where  $F$  is the local volume fraction of liquid phase. In the cells occupied with the liquid phase,  $F$  is unity, and in the cells occupied with the gas phase,  $F$  is zero. For the cells containing the interface bounding the liquid and gas phases,  $F$  lies between zero and unity. The  $F$  function is utilized to determine which cells contain a boundary and where the fluid is located in those cells. The derivatives of  $F$  are used to determine the mean local surface normal, and the cell  $F$  value is used to construct a line cutting the cell that will approximate the interface. Since  $F$  is a step function, its derivatives must be computed in a special way.

Using the standard finite difference technique to solve equation (2.4) would lead to smearing the value of  $F$  and the interfaces would lose their definition. The fact that  $F$  is a step function allows us to use a form of donor-acceptor differencing that preserves the discontinuous nature of  $F$ . The details of this method are described in chapter 3.

Equations (2.1)-(2.3) are subject to the no-slip velocity boundary condition, i.e., zero tangential velocity at the wall. The normal component of the velocity at the wall is also set to be zero due to the non-penetrating wall boundary condition.

There are generally two approaches to model fluid flow; two-phase and one-phase approach. In the two-phase approach the governing equations are solved in both phases by solution of the variable density Navier-Stokes equations. In the one phase approach, which has been used in this research, the momentum equations are only solved in the liquid phase (water) and the effect of the gas phase (air) is taken into account through free surface conditions. On the free surface, the continuity of velocity and stress components must be satisfied. Continuity of velocity is a purely kinematical constraint, and is called the kinematical boundary condition. Continuity of the stress vector is also required to prevent the material surface from acquiring an infinite acceleration, and is called the dynamic boundary condition. The exact surface stress boundary condition at the free surface, in tensor form can be written as [26;31]:

$$(\sigma\kappa - p_s)\hat{n}_i = (\delta_{ik} - \hat{n}_i\hat{n}_k)\frac{\partial\sigma}{\partial x_k} - \tau_{ik}\hat{n}_k \quad (2.5)$$

where  $\sigma$  is the fluid surface tension,  $\hat{n}_i$  is the unit force normal to the surface ( into the fluid ) and  $\kappa$  is the local free surface curvature. For two dimensional flows, projecting

equation (2.5) along the unit normal  $\hat{n}$  and unit tangent  $\hat{t}$  results in an equivalent set of scalar boundary conditions. These are the normal stress boundary condition given by:

$$p_s - \sigma\kappa = 2\mu n_k \frac{\partial u_k}{\partial n} \quad (2.6)$$

and the tangential stress boundary condition given by:

$$\mu \left( t_i \frac{\partial u_i}{\partial n} + n_k \frac{\partial u_k}{\partial s} \right) = \frac{\partial \sigma}{\partial s} \quad (2.7)$$

where,  $\frac{\partial}{\partial s} = \hat{t} \cdot \nabla$  is the surface derivative and  $\frac{\partial}{\partial n} = \hat{n} \cdot \nabla$  is the normal derivative. The

viscous effects at the free surface have been neglected and the liquid is treated as an ideal fluid. Since the surface tension,  $\sigma$ , is assumed to be constant, and the curvature radius of the free surface is expected to be large under conditions of interest in this study, the surface pressure ( $\sigma\kappa$ ) effect has been ignored at the free surface. Thus the normal stress boundary condition becomes:

$$p_s = 0 \quad (2.8)$$

Equation (2.8) is called the inviscid free surface normal stress condition. Our validation showed that it is an acceptable approximation for the conditions considered in this study.

## 2.2 Partial Cell Treatment Method

The partial cell treatment method has been used to model screens within the TLD and fully resolve the flow field through them. The simplicity of the partial cell treatment method for modeling complex geometric regions is very attractive. The basic concept is to indicate the fraction of the cell volume and the fraction of each cell face open to flow,

and to use this information to modify the spatially discretized equation in partial cells [26;30;31]. The parameter which is used to indicate this fraction is called “partial flow flag” and is represented by  $\theta$ . Since the obstacles are assumed to be fixed, and all the calculations are performed in the static obstacle frame, the volume fraction  $\theta$  is a time independent scalar field. It can be defined as a step function, i.e.,

$$\theta(\vec{x}) = \begin{cases} 1.0 & \text{in the fluid} \\ 0.0 & \text{in the obstacle} \end{cases} \quad (2.9)$$

$\theta$  is a perfect step function only when the obstacle boundaries coincide with the mesh lines representing lines of constant  $x$  and  $y$ . In general, the obstacle boundaries cut the cells arbitrarily. This makes the  $\theta$  values to be in the range between 0 and 1, which is also necessary to avoid a “stair-step” model of a curved interior obstacle boundary. Those cells having a value of  $\theta$  between 0 and 1 are termed as the “Partial flow cells” because a portion  $\theta$  of their finite difference volume is open to flow and the remaining portion  $1-\theta$  is occupied by an obstacle and closed to the flow.

The partial cell treatment method can be regarded as a special case of the treatment of a defined two phase flow. The first phase, in this case the internal obstacles, is fixed in space and time, and with an infinite density. The other phase, in this case the sloshing fluid, is moving with a constant density. The continuity and momentum equations with introduced  $\theta$  become:

$$\nabla \cdot (\theta \vec{u}) = 0 \quad (2.10)$$

and

$$\frac{\partial(\theta \vec{u})}{\partial t} + \nabla \cdot (\theta \vec{u} \vec{u}) = \theta \left[ \vec{g} - \frac{\vec{\nabla} p}{\rho} \right] + \nabla \cdot \left( \frac{\theta \vec{\tau}}{\rho} \right) \quad (2.11)$$

where  $\theta$  is the volume fraction of the moving fluid and its value is defined based on the location of obstacles in the flow field.

## 2.3 Motion Equation of Structure

The motion of a simple idealized structure due to dynamic excitation can be considered as a discrete single degree of freedom SDOF body vibration case, in which it is governed by an ordinary differential equation [10]. The governing equation, or equation of motion, is derived for the two types of dynamic excitation; external force and earthquake ground motion.

### 2.3.1 External Force

Figure 2-2 shows a linear structure of mass  $M_S$ , with stiffness  $K_S$ , and damping  $C_S$  subjected to an externally applied dynamic force  $F_e(t)$ .

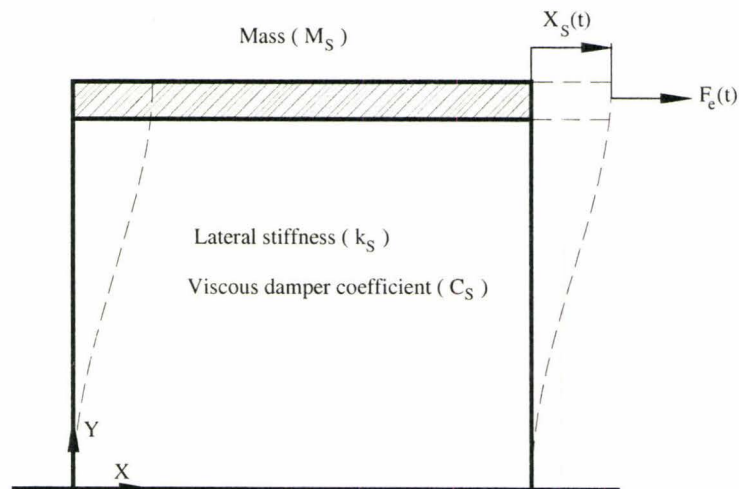


Figure 2-2: Single degree of freedom structure for external force.

This notation indicates that the force  $F_e$  varies with time  $t$ . Under the influence of such a force, the top of the structure moves in the lateral direction by an amount  $X_s(t)$ , which is also the deformation in the structure. The various forces acting on the mass at some instant of time are shown in a free-body diagram of the mass, see figure 2-3.

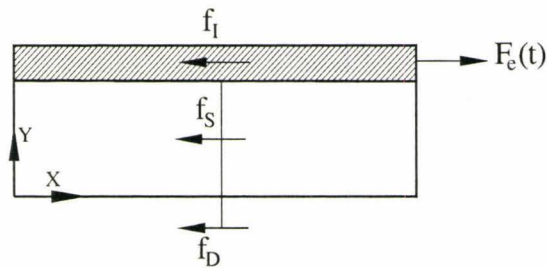


Figure 2-3: Free body diagram for external force.

These include the external force  $F_e(t)$ , the elastic resisting force  $f_s$ , the damping force  $f_D$  and the inertia force  $f_I$ . The elastic and damping forces act to the negative  $x$ -direction because they resist the deformation and velocity, respectively, which are in the positive  $x$ -direction. The inertia force also acts in the negative  $x$ -direction, opposite to the direction of positive acceleration. At each instant of time, the mass is in equilibrium under the action of these forces at that time. From the free body diagram, this condition of dynamic equilibrium is:

$$f_I + f_D + f_s = F_e(t) \quad (2.12)$$

The inertia, damping and elastic forces are next expressed in terms of  $X_s(t)$  and related quantities. For a linear structure, the elastic force is:

$$f_s = K_s X_s \quad (2.13)$$

where  $K_S$  is the lateral stiffness of the structure and  $X_S$  is the displacement. The damping force is:

$$f_D = C_S \dot{X}_S \quad (2.14)$$

where  $C_S$  is the damping coefficient for the structure and  $\dot{X}_S$  is the velocity. The inertia force associated with the mass  $M_S$  undergoing on acceleration  $\ddot{X}_S$  is:

$$f_I = M_S \ddot{X}_S \quad (2.15)$$

Substituting equations (2.13)-(2.15) into equation (2.12) results in:

$$M_S \ddot{X}_S + C_S \dot{X}_S + K_S X_S = F_e(t) \quad (2.16)$$

This is the equation of motion governing the deformation  $X_S(t)$  of the idealized structure of figure 2-2 subjected to an external dynamic force  $F_e(t)$

### 2.3.2 Earthquake Ground Motion

No external dynamic force is applied to the roof in the idealized one-story structure shown in figure 2-4. The excitation in this case is the earthquake included motion of the base of the structure, presumed to be only a horizontal component of ground motion, with displacement  $X_g(t)$ , velocity  $\dot{X}_g(t)$  and acceleration  $\ddot{X}_g(t)$ . Under the influence of such an excitation, the base of the structure is displaced by an amount  $X_g(t)$ . If the ground is rigid and structure undergoes the deformation  $X_S(t)$ , the total displacement of the roof of the structure is:

$$X_I(t) = X_g(t) + X_S(t) \quad (2.17)$$

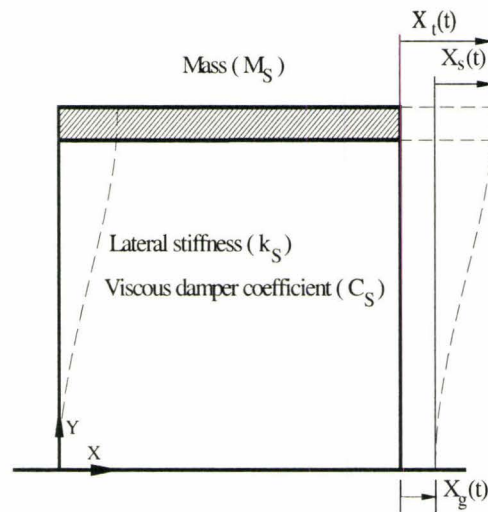


Figure 2-4: Single degree of freedom structure for ground motion.

From the free body diagram of the mass shown in figure 2-5, the equation of dynamic equilibrium is:

$$f_I + f_D + f_S = 0.0 \quad (2.18)$$

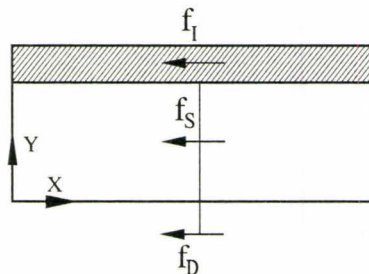


Figure 2-5: Free body diagram for ground motion.

Equations (2.13) and (2.14) still apply because the elastic and damping forces depend only on the relative displacement and velocity, not on the total quantities. However, the mass in this case undergoes acceleration  $\ddot{X}_t$  and the inertia force therefore is:

$$f_I = M_S \ddot{X}_t \quad (2.19)$$

which with the aid of equation (2.17) can be expressed as:

$$f_I = M_S (\ddot{X}_g + \ddot{X}_S) \quad (2.20)$$

Equation (2.18) after substitution of equations (2.13), (2.14), and (2.20) can be expressed as:

$$M_S \ddot{X}_S + C_S \dot{X}_S + K_S X_S = -M_S \ddot{X}_g(t) \quad (2.21)$$

This is the equation of motion governing the deformation  $X_S(t)$  of the idealized structure system of figure 2-4 subjected to earthquake ground acceleration  $\ddot{X}_g(t)$ .

Comparison of equations (2.16) and (2.21) shows that the equation of motion for the structure subjected to the two cases of excitation is the same. The deformation response  $X_S(t)$  of the structure to ground acceleration  $\ddot{X}_g(t)$  will be identical to the response of the structure on fixed base due to an external force equal to mass times the ground acceleration, acting opposite to the direction of acceleration. The ground motion can therefore be replaced by an effective force  $= -M_S \ddot{X}_g$ .

Given the mass ( $M_S$ ), stiffness ( $K_S$ ), damping ( $C_S$ ) and the excitation force ( $F_e$ ) or ground acceleration  $\ddot{X}_g(t)$ , a fundamental problem in structural dynamics is to determine the deformation response  $X_S(t)$  of the idealized structure.

## 2.4 Fluid-Structure Interaction Model

Since TLDs are coupled with a structure, any meaningful assessment of the performance of a TLD must include the effect of such coupling. In this research, a fluid-

structure interaction model has been developed. The TLD has been coupled with a SDOF structure as shown in figure 2-6. A TLD is designed to have natural frequency approximately equal to the natural frequency of the structure so that the sloshing motion of water inside the tank will cause inertia forces approximately anti-phase to the building motion. Therefore, the generated force by the water sloshing motion acts as a resisting or damping force to the external force. The coupled system is treated as a SDOF system subjected to total external force which is sum of the damping force,  $F_{TLD}$  and the external force,  $F_e$ . The equation of motion of the coupled system is expressed as:

$$M_S \ddot{X}_S + C_S \dot{X}_S + K_S X_S = F_e + F_{TLD} \quad (2.22)$$

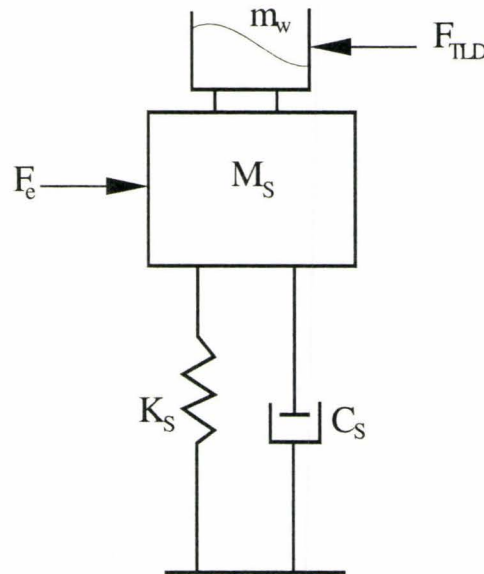


Figure 2-6: Schematic of coupling between TLD and SDOF structure.

where  $M_S$ ,  $C_S$  and  $K_S$  are mass, generalized damping and stiffness respectively and  $X_S$  is structural displacement. The damping force due to water sloshing is calculated by

applying momentum theory. Based on this theory the damping force can be determined by the rate of the change of momentum which is expressed as:

$$F_{TLD} = \frac{\partial P(t)}{\partial t} \quad (2.23)$$

where  $P(t)$  is the total momentum of contained fluid. Figure 2-7 shows typically how  $F_{TLD}$  acts on the structure. Structures in real applications are often subjected to loads which are normally random with no function to predict its behavior. Therefore, the selected method to solve equation (2.21) numerically should be able to accept random as well as harmonic excitation force. Duhamel integral method which has been chosen in this work, has the ability to solve this equation with any random or harmonic excitation force. In this method the excitation force is approximated with a piecewise linear function between each two time steps. Detailed information about this method is presented in the chapter 3.

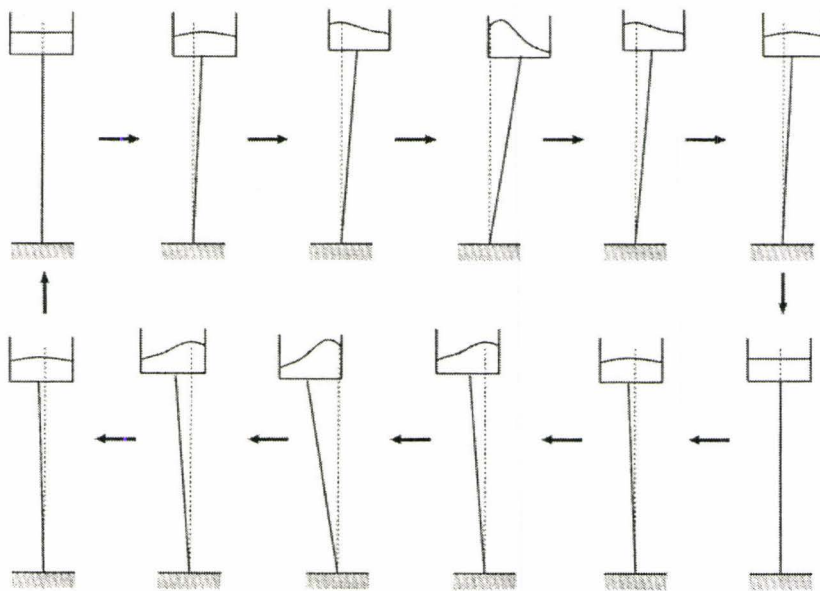


Figure 2-7: Typical free surface during one period of sloshing [22].

## Chapter 3: Numerical Model

### 3.1 Flow Chart of Algorithm

Part of the developed numerical model is based on RIPPLE which was developed at Los Alamos National Laboratory (Kothe et al., 1994). Several modifications and routines have been added for simulation of the TLD-Structure system considered in this study. This chapter provides a detailed description of the numerical algorithm used in this research. The algorithm is based on the Eulerian approach with a fixed grid [26; 28; 30; 63]. The complete Navier-Stokes equations in primitive variables for an incompressible flow are solved by the finite difference method. At the beginning, the whole computational domain is spatially discretized by the  $m \times n$  rectangle cells having variable sizes,  $\Delta x_i$  for  $i^{\text{th}}$  column and  $\Delta y_j$  for the  $j^{\text{th}}$  row, as sketched in figure 3-1.

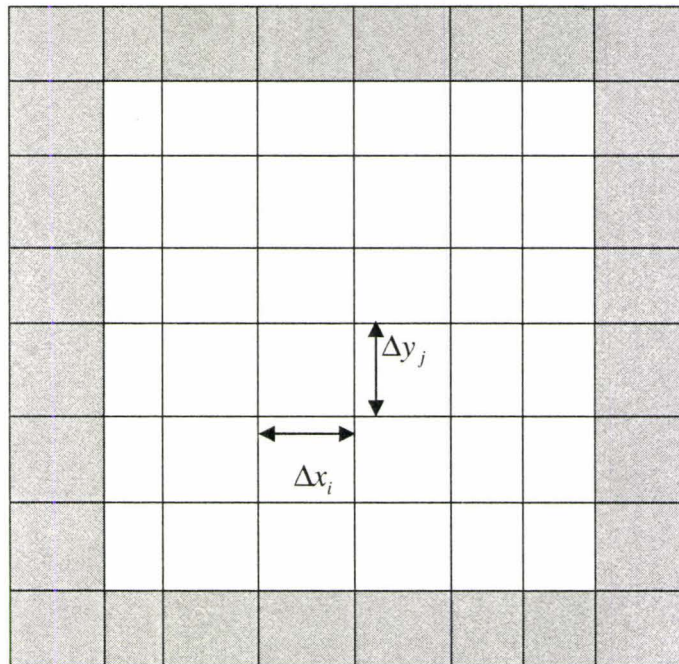
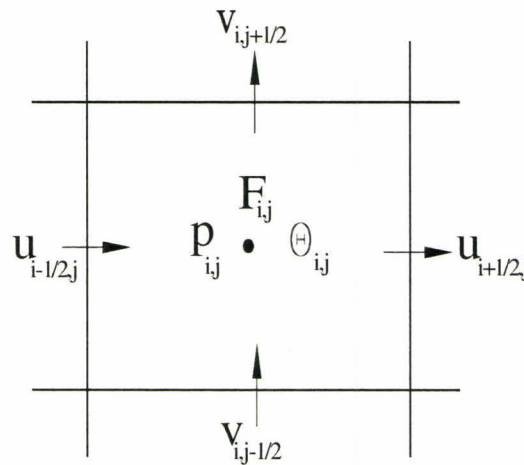


Figure 3-1: Finite difference mesh with variable rectangular mesh.

The computational domain is surrounded by a layer of fictitious cells. These cells are used to set velocity boundary conditions, so that the same discretized equations are used in the whole computational domain. The location of the dependent variables in each mesh cell is represented in figure 3-2.



**Figure 3-2: Location of variables in a typical mesh cell.**

All scalar quantities, i.e., pressure ( $p$ ), the volume of fluid (VOF) function ( $F$ ), and the openness function  $\theta_{i,j}$ , are defined in the center of the cells. The vector and vector related quantities, i.e.,  $u, v$  and the openness functions on the cell faces,  $\theta_{i+1/2,j}$  and  $\theta_{i,j+1/2}$  are defined in the cell faces as shown in figure 3-2.  $\theta_{i,j}$ ,  $\theta_{i+1/2,j}$  and  $\theta_{i,j+1/2}$  are the geometrical quantities arising from the partial cell treatment method to define the obstacles in the flow field, and represent the fractions of the cell volume, right cell face and top cell face open to flow. The model has an automatic mesh generator which has the ability to produce the variable size rectangular grid system.

It is noted that the variable size mesh system always reduces the accuracy of the numerical results, when compared with a constant mesh with size equal to the smallest cell in the variable size mesh system. This is based on the similar argument that use of constant time step produces more accurate results than the use of the variable time steps. Therefore, when a uniform grid system is possible to resolve the problem properly, it is always recommended. It is the reason that uniform grids have been used for cases of a TLD without the screen. In the case of TLD with screens, a uniform grid has been used for the  $y$ - direction only. In the  $x$ -direction of the same case however, a variable size of mesh is necessary to reduce the computational cost, as the resolution near the screen must be rather fine in comparison to what is needed to resolve the flow field away from the screen. The precaution to be taken when using a variable mesh system, is that it must change gradually to avoid excessive numerical errors.

The flow chart of the algorithm is shown in figure 3-3. In this algorithm, the basic computational cycle is the following:

1. Explicit approximations of the momentum equations have been used to calculate the first guess of the new time level ( $n+1$ ) velocities, using the previous (time level  $n$ ) values for the convective, viscous and pressure gradient accelerations.
2. Pressure is iteratively adjusted in each cell in order to satisfy the continuity equation. Velocity changes induced by the pressure corrections are computed.
3. The  $F$  function is updated to determine the fluid configuration at new time level  $n+1$ . All mesh cells are re-flagged as full, surface or empty. Then the free surface orientation is determined by the new updated values of  $F$ .

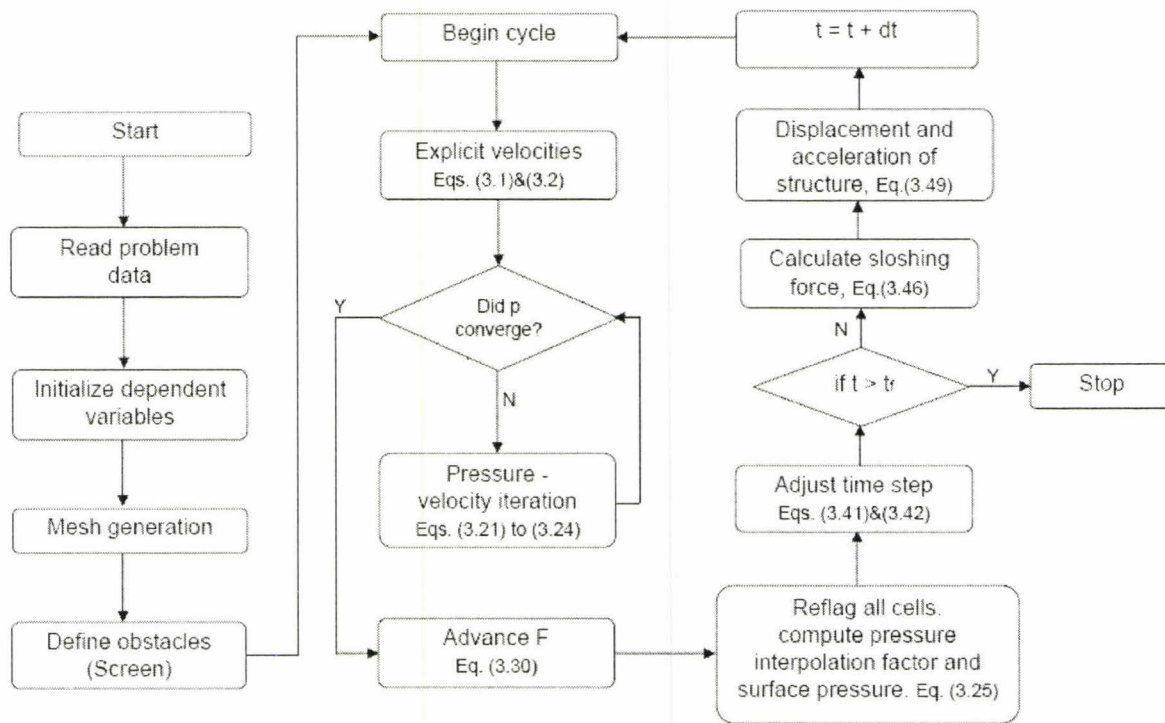


Figure 3-3: The flow chart of the algorithm.

4. All variables are updated and the new time step is adjusted from the stability conditions.
5. The sloshing force is calculated from the updated flow field.
6. The equation of motion for the structure is solved and the acceleration and the displacement of the structure are computed under the external excitation and sloshing forces.
7. The time and cycle counters are incremented and the cycle is restarted.

### 3.2 Discretization of the Governing Equations

The discretization has been performed in the physical space using the finite-

difference method. A forward staggered grid arrangement is used in which the scalar quantities are located at the geometric center of the cell, while the velocity components  $u$  and  $v$  are displaced in the  $x$  and  $y$  coordinate directions, respectively, to lie at the midpoints of the cell faces. The locations of the various dependent variables for this grid configuration are shown in figure 3-2.

The discretization of momentum equations leads to the following expressions in the  $x$ - and  $y$ - directions:

$$u_{i+\frac{1}{2},j}^{n+1} = u_{i+\frac{1}{2},j}^n + \delta t \left[ -\frac{1}{\rho} \frac{p_{i+1,j}^{n+1} - p_{i,j}^{n+1}}{x_{i+1} - x_i} + g_x - FUX - FUY + VISX \right] \quad (3.1)$$

$$v_{i,j+\frac{1}{2}}^{n+1} = v_{i,j+\frac{1}{2}}^n + \delta t \left[ -\frac{1}{\rho} \frac{p_{i,j+1}^{n+1} - p_{i,j}^{n+1}}{y_{j+1} - y_j} + g_y - FVX - FVY + VISY \right] \quad (3.2)$$

where,  $FUX$ ,  $FUY$ ,  $FVX$  and  $FVY$  represent the convection terms of the momentum equations in the  $u$  and  $v$  directions, respectively. Also  $VISX$  and  $VISY$  are associated with the diffusion terms of the momentum equations in the  $x$  and  $y$  directions. Since the upwind scheme usually introduces significant numerical damping and the central difference scheme generates numerical instability, a combination of these two schemes usually yields a more accurate algorithm. Thus, the general finite difference formula for the advection of  $u$  in the  $x$  and  $y$  directions become:

$$FUX = u \frac{\partial u}{\partial x} \Big|_{i+\frac{1}{2},j} = u_{i+\frac{1}{2},j}^n \frac{1}{\Delta x_\alpha} \left[ \Delta x_i \left( \frac{\partial u}{\partial x} \right)_{i+1,j} + \Delta x_{i+1} \left( \frac{\partial u}{\partial x} \right)_{i,j} + \alpha \cdot \text{sign} \left( u_{i+\frac{1}{2},j} \right) \left( \Delta x_{i+1} \left( \frac{\partial u}{\partial x} \right)_{i,j} - \Delta x_i \left( \frac{\partial u}{\partial x} \right)_{i+1,j} \right) \right] \quad (3.3)$$

$$FUY = v \frac{\partial u}{\partial y} \Big|_{i+\frac{1}{2},j} = v_{i+\frac{1}{2},j}^n \frac{1}{\Delta y_\alpha} \left[ \begin{array}{l} \Delta y^- \left( \frac{\partial u}{\partial y} \right)_{i+\frac{1}{2},j+\frac{1}{2}} + \Delta y^+ \left( \frac{\partial u}{\partial y} \right)_{i+\frac{1}{2},j-\frac{1}{2}} + \\ \alpha \cdot \text{sign} \left( v_{i+\frac{1}{2},j} \right) \left( \Delta y^+ \left( \frac{\partial u}{\partial y} \right)_{i+\frac{1}{2},j-\frac{1}{2}} - \Delta y^- \left( \frac{\partial u}{\partial y} \right)_{i+\frac{1}{2},j+\frac{1}{2}} \right) \end{array} \right] \quad (3.4)$$

where,

$$\Delta x_\alpha = \Delta x_i + \Delta x_{i+1} + \alpha \cdot \text{sign} \left( u_{i+\frac{1}{2},j} \right) (\Delta x_{i+1} - \Delta x_i) \quad (3.5)$$

$$\Delta y_\alpha = \Delta y^+ + \Delta y^- + \alpha \cdot \text{sign} \left( v_{i+\frac{1}{2},j} \right) (\Delta y^+ - \Delta y^-) \quad (3.6)$$

$$v_{i+\frac{1}{2},j} = \frac{1}{2(\Delta x_i + \Delta x_{i+1})} \left[ \Delta x_{i+1} v_{i,j+\frac{1}{2}} + \Delta x_{i+1} v_{i,j-\frac{1}{2}} + \Delta x_i v_{i+1,j+\frac{1}{2}} + \Delta x_i v_{i+1,j-\frac{1}{2}} \right] \quad (3.7)$$

where  $\Delta x_i$ ,  $\Delta y^+$  and  $\Delta y^-$  have been shown in the figure 3-4.

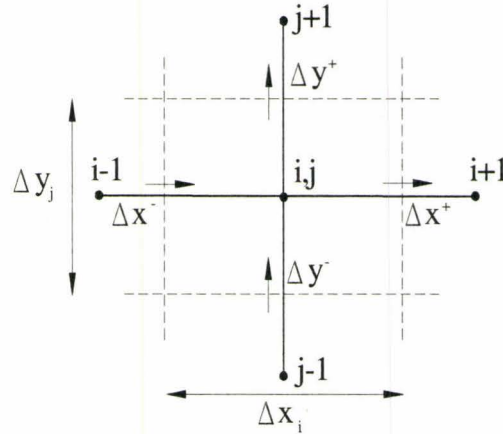


Figure 3-4: A computational Cell.

Here,  $\alpha$ , the donor-cell fraction and the convective differencing, defines the linear

combination of the upwind and the centered differencing. When  $\alpha = 0$ , this formulation reduces to a second order accurate, centered, difference approximation. When  $\alpha = 1$ , the first order upwind form is recovered. In general central differences are more accurate, but also unstable when combined with forward time differences. For each particular problem, there will be an optimum  $\alpha$ . In TLD applications, an unstable solution was found for  $\alpha$  less than 0.5 and no considerable difference was detected for the values between 0.5 and 1.0. The value of  $\alpha$  in this study set to 1.0 to help to reduce the simulation time.

The diffusion term,  $VISX$ , is expressed as:

$$VISX = \nu \left( \frac{\partial^2 u}{\partial x^2} \Big|_{i+\frac{1}{2},j} + \frac{\partial^2 u}{\partial y^2} \Big|_{i+\frac{1}{2},j} \right) \quad (3.8)$$

where:

$$\frac{\partial^2 u}{\partial x^2} \Big|_{i+\frac{1}{2},j} = \left[ \left( \frac{\partial u}{\partial x} \right)_{i+1,j} - \left( \frac{\partial u}{\partial x} \right)_{i,j} \right] / (x_{i+1} - x_i) \quad (3.9)$$

and

$$\frac{\partial^2 u}{\partial y^2} \Big|_{i+\frac{1}{2},j} = \left[ \left( \frac{\partial u}{\partial y} \right)_{i+\frac{1}{2},j+\frac{1}{2}} - \left( \frac{\partial u}{\partial y} \right)_{i+\frac{1}{2},j-\frac{1}{2}} \right] / \left( y_{j+\frac{1}{2}} - y_{j-\frac{1}{2}} \right) \quad (3.10)$$

Also the first derivative can be written as follows:

$$\left( \frac{\partial u}{\partial x} \right)_{i,j} = \frac{u_{i+\frac{1}{2},j} - u_{i-\frac{1}{2},j}}{x_{i+\frac{1}{2}} - x_{i-\frac{1}{2}}} \quad (3.11)$$

and

$$\left( \frac{\partial u}{\partial y} \right)_{i+\frac{1}{2},j+\frac{1}{2}} = \frac{u_{i+\frac{1}{2},j+1} - u_{i+\frac{1}{2},j}}{y_{j+1} - y_j} \quad (3.12)$$

Similar expressions are used for the advection terms  $FVX$ ,  $FVY$  and the diffusion term  $VISY$ .

### 3.3 Partial-Cell Treatment

As introduced in chapter two, partial cell treatment is a special tool to handle the interior obstacle and solid boundary. By using this method flow through the screen is resolved directly. The basic idea behind this technique is that the obstacle can be modeled as a special case of two-phase flow with infinite density. With the use of the partial cell treatment, the variables in the cells or the cell faces are redefined as the multiplication of the openness coefficients with the original variables. Near the obstacle, the openness coefficients are less than unity. The redefined variables therefore take lower values than their original ones. For each partial flow cell three quantities are defined to account for the openness coefficient: a volume fraction  $\theta_{i,j}$  at the cell center, an area fraction  $\theta_{i+\frac{1}{2},j}$  at the right face, and an area fraction  $\theta_{i,j+\frac{1}{2}}$  at the top face. The value of  $\theta$  is assigned manually based on the location of the obstacles in the flow field. Figure 3-5 shows clearly, how the partial flow factors are assigned for the cells that are filled fully or partially by the obstacles. If the cell (i,j) is fully obstacle, the values of  $\theta$  at the cell center and faces of the cell are assigned to zero. If the cell (i,j) is just partially filled by obstacle, the values of  $\theta$  are determined geometrically based on the percentage of the cell and cell faces which are open to flow. For example, in the partially filled obstacle cell

shown in figure 3-5,  $\theta_{i,j}$ ,  $\theta_{i+\frac{1}{2},j}$  and  $\theta_{i,j+\frac{1}{2}}$  is 0.75, 1.0 and 0.75, respectively. The same methodology is accounted for all other cells including the obstacle to determine the values of partial flow factor at each cell.

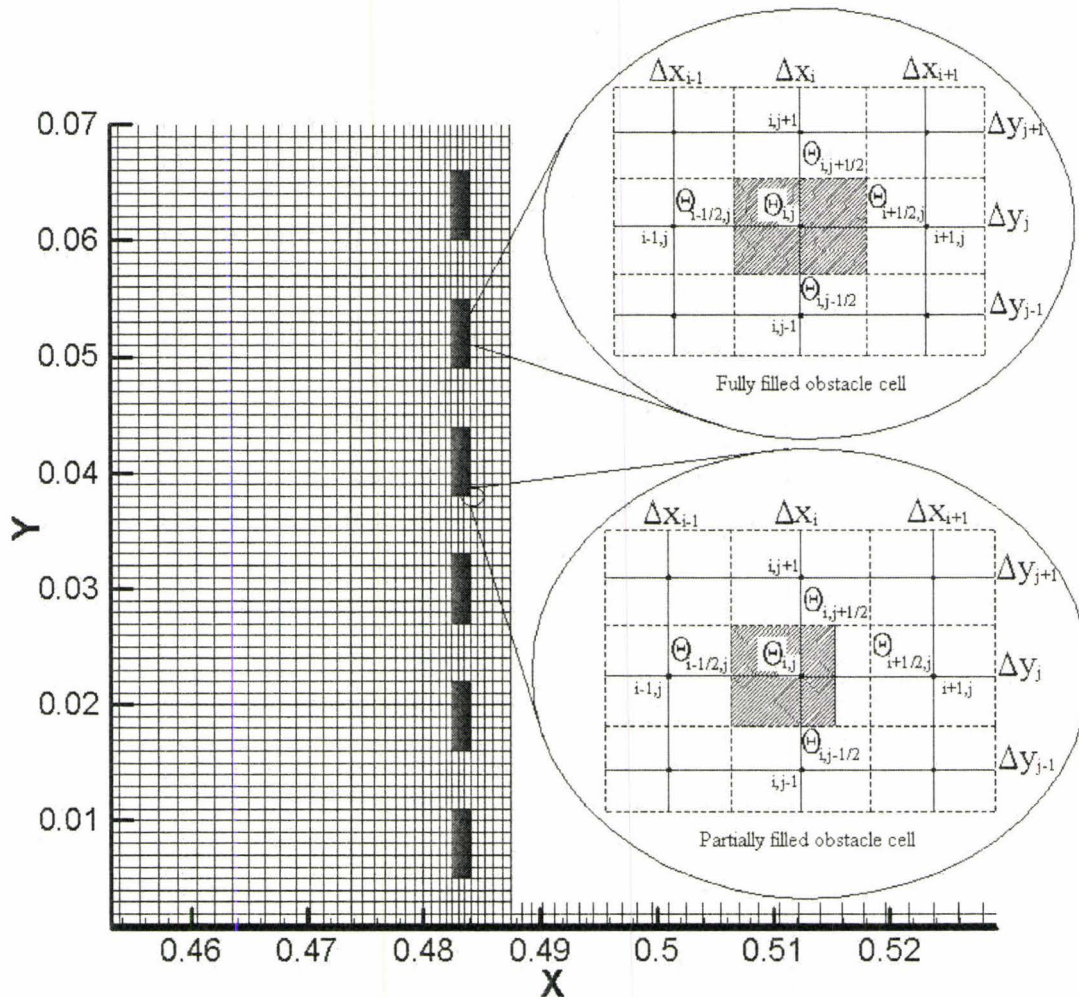


Figure 3-5: Partial flow factor for an obstacle cell

### 3.4 Continuity Equation Approximation

The calculated velocities using equations (3.1) and (3.2) will not satisfy the continuity equation, which, after discretization, takes the form:

$$\left[ \frac{u_{i+\frac{1}{2},j}^{n+1} \theta_{i+\frac{1}{2},j} - u_{i-\frac{1}{2},j}^{n+1} \theta_{i-\frac{1}{2},j}}{\Delta x_i} + \frac{v_{i,j+\frac{1}{2}}^{n+1} \theta_{i,j+\frac{1}{2}} - v_{i,j-\frac{1}{2}}^{n+1} \theta_{i,j-\frac{1}{2}}}{\Delta y_j} \right] / \theta_{i,j} = 0.0 \quad (3.13)$$

To satisfy the continuity equation simultaneously throughout the flow field, pressures and velocities must be corrected in each computational cell which is occupied by the fluid.

The solution is obtained by using the following iterative procedure:

Equations (3.1) and (3.2) are evaluated using quantities at the previous time step, i.e. at  $t=n$ , producing a provisional velocity field used as an estimate of the advanced time velocities. In the fluid cells, a pressure correction is calculated from:

$$\delta p = -\frac{S}{\partial S / \partial p} \quad (3.14)$$

[where S is the value of the left side of equation (3.13) evaluated with the most updated values of u, v and p. Equation (3.14) is derived by substituting the right side of the equations (3.21) to (3.24) into the continuity equation.] NOT clear.

The pressure correction coefficient  $\beta = \frac{1.0}{\partial S / \partial p}$  is obtained from:

$$\beta = \frac{\rho \theta_{i,j}}{2 \delta \left( \lambda_{i+\frac{1}{2}} + \lambda_{i-\frac{1}{2}} + \xi_{j+\frac{1}{2}} + \xi_{j-\frac{1}{2}} \right)} \quad (3.15)$$

where

$$\lambda_{i+\frac{1}{2}} = \frac{\theta_{i+\frac{1}{2},j}}{\Delta x_i (\Delta x_{i+1} + \Delta x_i)} \quad (3.16)$$

$$\lambda_{i-\frac{1}{2}} = \frac{\theta_{i-\frac{1}{2},j}}{\Delta x_i (\Delta x_{i-1} + \Delta x_i)} \quad (3.17)$$

$$\xi_{j+\frac{1}{2}} = \frac{\theta_{i,j+\frac{1}{2}}}{\Delta y_j (\Delta y_{j+1} + \Delta y_j)} \quad (3.18)$$

$$\xi_{j-\frac{1}{2}} = \frac{\theta_{i,j-\frac{1}{2}}}{\Delta y_j (\Delta y_{j-1} + \Delta y_j)} \quad (3.19)$$

The  $k^{th}$  iteration for the pressure would be:

$$p_{i,j}^k = p_{i,j}^{k-1} + \delta p \quad (3.20)$$

and the velocities at all four faces of a cell are updated using:

$$u_{i+\frac{1}{2},j}^k = u_{i+\frac{1}{2},j}^{k-1} + \delta t \frac{\delta p}{\rho(x_{i+1} - x_i)} \quad (3.21)$$

$$u_{i-\frac{1}{2},j}^k = u_{i-\frac{1}{2},j}^{k-1} - \delta t \frac{\delta p}{\rho(x_i - x_{i-1})} \quad (3.22)$$

$$v_{i,j+\frac{1}{2}}^k = v_{i,j+\frac{1}{2}}^{k-1} + \delta t \frac{\delta p}{\rho(y_{j+1} - y_j)} \quad (3.23)$$

$$v_{i,j-\frac{1}{2}}^k = v_{i,j-\frac{1}{2}}^{k-1} - \delta t \frac{\delta p}{\rho(y_j - y_{j-1})} \quad (3.24)$$

For the cells that contain a free surface, this procedure is modified. For these cells, the pressure,  $p_{i,j}$ , is derived using linear interpolation between the surface pressure ( $p_s$ ), calculated from the surface tension, and a neighboring pressure ( $p_n$ ) inside the fluid in a direction perpendicular to the free surface, i.e. :

$$p_{i,j} = (1-\eta)p_n + \eta p_s \quad (3.25)$$

where the distance coefficient factor  $\eta$  is defined by:

$$\eta = \frac{d_c}{d} \quad (3.26)$$

$d$  and  $d_c$  are defined in figure 3-6 where  $d_c$  is the distance between two adjacent grids and  $d$  is calculated from the orientation of free surface at the previous time step. The location of neighboring pressure ( $p_n$ ) has been shown in figure 3-6 as  $(i,j-1)$ .

The new  $p_{i,j}$  is obtained iteratively. The iteration is continued until all residuals ( $S$ ) are sufficiently smaller than a small number,  $\varepsilon$  which is typically of the order of  $10^{-4}$ . The last values of the velocity and pressure fields are used as the new guess in the next time step. In most cases, convergence of the iterations may be accelerated by using successive-over-relaxation by multiplying the  $\delta p$  by an over relaxation parameter  $\omega_r$ . A value of 1.7 has been used in this study.

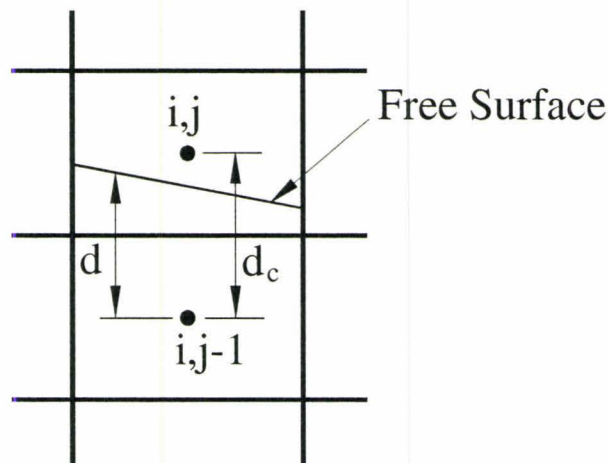


Figure3-6: Geometric parameters of a surface cell.

After the pressure correction is found from equation (3.14), neighboring velocities are updated using equations (3.21) to (3.24); the pressure correction is always computed using the most up-to-date velocities.

In my case I should omit  
the eq.

### 3.5 Volume of Fluid Method

After the velocity and pressure fields are advanced to the time level  $n+1$ , the fluid configuration is updated. Once the time advanced fluid configuration is found, appropriate boundary conditions are imposed and the cycle is restarted.

The VOF function  $F$  is governed by equation (2.4). Because  $F$  is discontinuous, its convective fluxes must be computed in a special way that preserves sharp interface definition, conserves the total fluid volume, and leads to a numerically stable algorithm. Combining equation (2.4) with the continuity equation (2.1) gives:

$$\frac{\partial(\theta F)}{\partial t} + \frac{\partial(\theta F u)}{\partial x} + \frac{\partial(\theta F v)}{\partial y} = 0.0 \quad (3.27)$$

This conservative form of the F-equation allows one to write a difference approximation that conserves the fluid volume. The discretized form of equation (3.20) is written as follows:

$$F_{i,j}^{n+1} = F_{i,j}^n - \frac{\delta t}{\theta_{i,j}} \left[ \frac{1}{\Delta x_i} \left( \theta_{i+\frac{1}{2},j} u_{i+\frac{1}{2},j}^{n+1} F_{i+\frac{1}{2},j}^n - \theta_{i-\frac{1}{2},j} u_{i-\frac{1}{2},j}^{n+1} F_{i-\frac{1}{2},j}^n \right) + \frac{1}{\Delta y_j} \left( \theta_{i,j+\frac{1}{2}} v_{i,j+\frac{1}{2}}^{n+1} F_{i,j+\frac{1}{2}}^n - \theta_{i,j-\frac{1}{2}} v_{i,j-\frac{1}{2}}^{n+1} F_{i,j-\frac{1}{2}}^n \right) \right] \quad (3.28)$$

The convection algorithm must resolve the sharp interface at the free surface, and also guarantee that there is not any flux across any interfacial cell more than the available amount in that cell. A donor-acceptor method has been used in order to satisfy these conditions. At each boundary of each cell, one of the two interface cells is designated as a donor cell and the other is designated as an acceptor cell. Cell quantities are given the subscript D for donor and A for acceptor, respectively. The labeling is accomplished by

means of the algebraic sign of the fluid velocity normal to the boundary. Each computational cell will have four separate assignments of D or A corresponding to each of the cell boundaries as shown in figure 3-7.

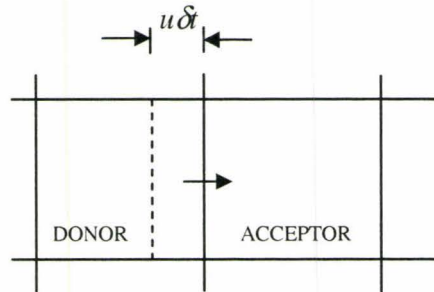


**Figure3-7: Donor-acceptor cell configuration.**

This method is based on the calculation of the amount of  $F$  which is fluxed and advected through the right-hand face of the donor cell during a time step  $\delta t$ . The flux of volume crossing this cell face per unit cross sectional area is:

$$V_x = u_{i+\frac{1}{2},j}^{n+1} \cdot \delta t \quad (3.29)$$

where  $u$  is the normal velocity at the cell face. The sign of  $u$  determines the donor and the acceptor cells. If  $u$  is positive the upstream or left cell is the donor and the downstream or right cell is the acceptor. The amount of  $F$  advected across the cell face in one time step is  $\Delta F$ , where:

$$\Delta F = \Delta y_j \text{MIN}(F_{AD}|V_x| + CF, F_D \Delta x_D) \quad (3.30)$$

where,

$$CF = \text{MAX}\{(1.0 - F_{AD})|V_x| - (1.0 - F_D)\Delta x_D, 0.0\} \quad (3.31)$$

In the same way, the flux of volume crossing the top boundary of cell  $ij$  is  $V_y = v_{i,j+\frac{1}{2}}^{n+1} \cdot \delta t$ ,

and the amount of  $F$  actually fluxed through the top cell face is:

$$\Delta F = \Delta x_i \text{MIN}(F_{AD}|V_y| + CF, F_D \Delta y_D) \quad \leftarrow \text{not clear} \quad (3.32)$$

where,

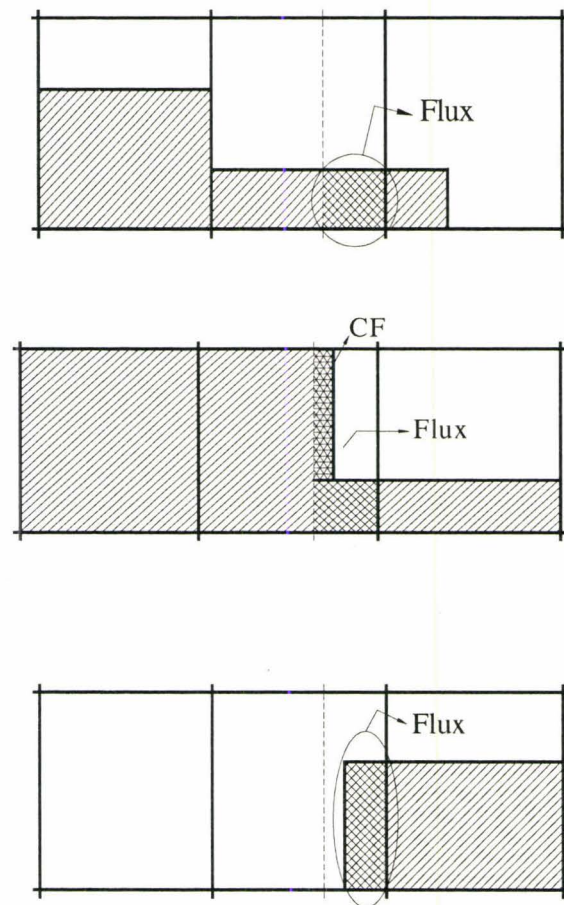
$$CF = \text{MAX}\{(1.0 - F_{AD})|V_y| - (1.0 - F_D)\Delta y_D, 0.0\} \quad (3.33)$$

In these expressions, the subscript A denotes the acceptor cell, the subscript D the donor cell, and the double subscript AD is either A or D [depending on the orientation of the free surface relative to the direction of the flow]. The MIN feature in these equations prevents the fluxing of more  $F$  from the donor cell than it has to give, while the MAX feature accounts for an additional  $F$  flux ( $CF$ ) if the amount of void ( $1-F$ ) to be fluxed exceeds the amount of void available in the donor cell. The rules of choosing  $AD=A$  or  $AD=D$  are as follow. [If the free surface is convected mostly normal to itself, the acceptor cell  $F$ -value is used, otherwise the donor cell  $F$ -value is used. If the acceptor cell is empty, or if the cell upstream of the donor cell is empty; the acceptor cell is used to determine the flux, regardless of the orientation of the free surface.]

The value of  $\Delta F$  computed by the above method is subtracted from the donor cell and added to the acceptor cell. This process is repeated for all cell boundaries in the mesh, and the resulting  $F$  values define the new fluid configuration. It is possible the time-advanced  $F$  values may have values slightly less than zero, or slightly greater than 1.

Hence, after the  $F$ -convection calculation has been completed, the mesh is swept to reset values of  $F$  less than zero back to zero, and values of  $F$  greater than one back to

one. Accumulated changes in  $F$  are recorded during a computation; they may be printed at any time. These tiny volume falsifications are due to small errors in mass conservation and numerical diffusion in F-convection algorithm. They can be reduced by either specifying a smaller tolerance for the residual divergence in the pressure-velocity iteration, or by increasing the mesh resolution and lowering the Courant number.



A) If the fluid surface is parallel to the flow, then the  $F$  value of the donor cell is used to define the fractional area of the cell face that is to be fluxed, i.e.  $AD = D$

*not clear*

B) If the fluid surface is mostly normal to the flow, then an extra amount of fluid  $CF$  is fluxed between the dashed line and the flux boundary and the  $F$  value of acceptor cell is used to define the fractional area of the cell face that is to be fluxed, i.e.  $AD = A$

C) If the upstream cell is empty, then all of the fluid lying between the dashed line and the flux boundary moves into the acceptor cell and then the  $F$  value of the acceptor cell is used to define the fractional area of the cell face that is to be fluxed, i.e.  $AD = A$

Figure 3-8: Examples of free surface shapes during the advection of  $F$ .

A free-surface cell  $i, j$  is defined as a cell with  $0 < f < 1$  and having at least one neighboring cell  $(i \pm 1, j)$  or  $(i, j \pm 1)$  that is empty (i.e. contains a zero value  $F$ ). It should be noted that  $F$  values cannot be tested against exact numbers because of round off errors. Instead, a cell is defined to be empty when  $F$  is less than  $\varepsilon_f$  and full when  $F$  is greater than  $1 - \varepsilon_f$ , where  $\varepsilon_f$  is typically  $10^{-6}$ . Accumulated volume errors after hundreds of cycles are typically a fraction of a per cent of the total  $F$  volume. This indicated that the  $F$ -convection algorithm preserves free surface sharpness and has good conservation properties.

Determination of whether the interface is mostly horizontal or vertical is based on estimating the local slope of the fluid-void interface. To determine the boundary slope, it must be recognized that the boundary can be represented either as a single-valued function of  $(x)$  i.e.,  $Y(x)$  or as a single valued function of  $(y)$ , i.e.,  $X(y)$ , depending on its orientation which is determined based on the value of  $F$  in the surface cell and its eight neighbors. A good approximation of  $Y(x_i)$  is:

$$Y(x_i) = F_{i,j-1} \Delta y_{j-1} + F_{i,j} \Delta y_j + F_{i,j+1} \Delta y_{j+1} \quad (3.34)$$

then

$$\left( \frac{dY}{dx} \right)_i = \left[ \frac{(Y_{i+1} - Y_i) \Delta x_{i-\frac{1}{2}}}{\Delta x_{i+\frac{1}{2}}} + \frac{(Y_i - Y_{i-1}) \Delta x_{i+\frac{1}{2}}}{\Delta x_{i-\frac{1}{2}}} \right] \cdot \frac{1}{\Delta x_{i-\frac{1}{2}} + \Delta x_{i+\frac{1}{2}}} \quad (3.35)$$

How??

where,

$$\Delta x_{i+\frac{1}{2}} = \frac{\Delta x_i + \Delta x_{i+1}}{2} \quad (3.36)$$

A similar calculation of  $\left(\frac{dX}{dy}\right)_j$  can be made from,

$$X(y_j) = F_{i-1,j}\Delta x_{i-1} + F_{i,j}\Delta x_i + F_{i+1,j}\Delta x_{i+1} \quad (3.37)$$

then 
$$\left(\frac{dX}{dy}\right)_j = \left[ \frac{(X_{j+1} - X_j)\Delta y_{j-\frac{1}{2}}}{\Delta y_{j+\frac{1}{2}}} + \frac{(X_j - X_{j-1})\Delta y_{j+\frac{1}{2}}}{\Delta y_{j-\frac{1}{2}}} \right] \cdot \frac{1}{\Delta y_{j+\frac{1}{2}} + \Delta y_{j-\frac{1}{2}}} \quad (3.38)$$

where

$$\Delta y_{j+\frac{1}{2}} = \frac{\Delta y_j + \Delta y_{j+1}}{2} \quad (3.39)$$

The general rule to determine the orientation of free surface is as follows:

If  $\left|\frac{dY}{dx}\right| > \left|\frac{dX}{dy}\right|$  and  $\frac{dY}{dx} > 0$ , then free surface is vertical with the fluid on the right side.

If  $\left|\frac{dY}{dx}\right| > \left|\frac{dX}{dy}\right|$  and  $\frac{dY}{dx} < 0$ , then free surface is vertical with the fluid on the left side.

If  $\left|\frac{dX}{dy}\right| > \left|\frac{dY}{dx}\right|$  and  $\frac{dX}{dy} > 0$ , then free surface is horizontal with the fluid on the top side.

If  $\left|\frac{dX}{dy}\right| > \left|\frac{dY}{dx}\right|$  and  $\frac{dX}{dy} < 0$ , then free surface is horizontal with the fluid on the bottom side.

Once the boundary slope and the side occupied by fluid have been determined, a line can be constructed in the cell with correct amount of F placed on the fluid side. This line is used as an approximation of the actual boundary and provides the information necessary to calculate  $d$  and  $d_c$ . Hence, the distance coefficient factor,  $\eta$ , can also be calculated for the application of the free surface pressure condition, equation (3.25)

## 3.6 Velocity Boundary Conditions

### 3.6.1 Mesh Boundaries

At the mesh boundaries, a no-slip boundary condition is imposed using the layer of fictitious cells. For example, if the left wall is a rigid no slip wall, both normal and tangential velocity components are set to zero, and the appropriate boundary conditions are:

$$u_{1,j}^{n+1} = 0.0, \quad v_{1,j}^{n+1} = -\frac{\Delta x_1}{\Delta x_2} v_{2,j}^{n+1}, \quad p_{1,j}^{n+1} = p_{2,j}^{n+1}, \quad F_{1,j}^{n+1} = F_{2,j}^{n+1} \quad (3.40)$$

The boundary conditions are imposed after applying the momentum equations and after each pass through the pressure iteration.

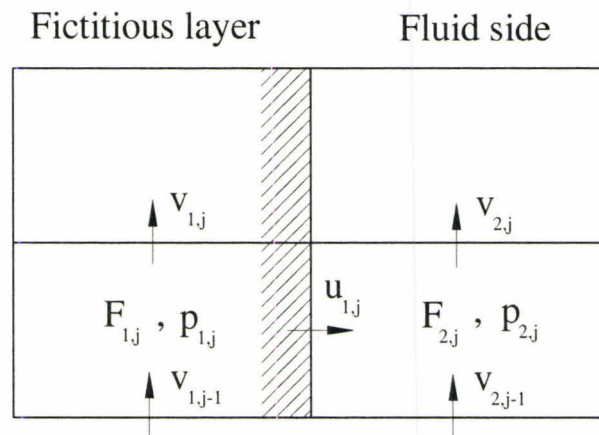


Figure 3-9: Boundary condition near the left wall.

Boundary conditions similar to the ones for the left mesh boundary are used at the right, top and bottom boundaries, reversing the roles of  $u$  and  $v$  as normal and tangential velocities when appropriate.

### 3.6.2 Free Surface Boundaries

The free surface boundary conditions are imposed in several ways in the solution algorithm. The kinematic boundary condition is automatically satisfied in the F-advection step. The normal stress dynamic boundary condition is imposed as a boundary condition for pressure. The tangential stress boundary condition is the only remaining condition to be satisfied.

The tangential stress condition is approximated by specifying velocities immediately outside the free surface, where these values are needed in the finite difference equations for points at the surface cells [28]. The velocities at all boundaries between surface and empty cells must be set as shown in figure 3-10.

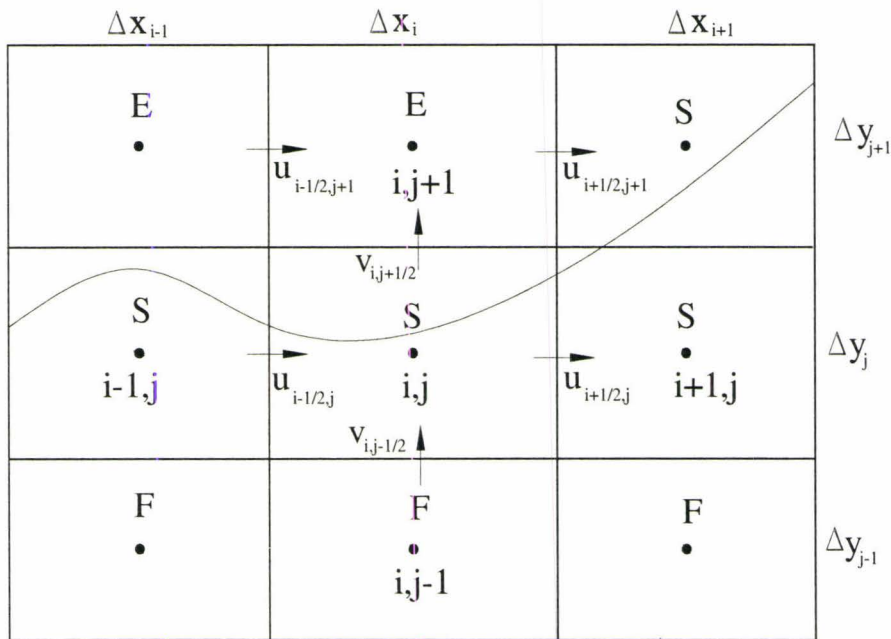


Figure 3-10: Boundary condition on free surface.

If the surface cell has only one neighboring empty cell, the boundary velocity is set to insure the satisfaction of the continuity equation. When there are two or more empty cell neighbors, the individual contributions to the divergence  $\partial u/\partial x$  and  $\partial v/\partial y$  are separately set to zero. Zero values for  $\partial u/\partial y$  and  $\partial v/\partial x$  are additionally used to set exterior tangent velocities between the empty cells adjacent to the surface cell on a free surface boundary.

### 3.6.3 Internal-Obstacle Boundaries

The internal obstacles are defined by flagging the cells of a mesh that are to be blocked out. This is done by assigning zero values for the openness volume and face functions ( $\theta_{i,j}$ ,  $\theta_{i+\frac{1}{2},j}$  and  $\theta_{i,j+\frac{1}{2}}$ ) for each obstacle cell.

Velocities and pressures are not calculated in obstacle cells. All velocity components on the faces of the obstacle cells are automatically set to zero. The values for volume fractions and pressures are set in all obstacle cells bordering fluid cells. These values are computed to be equal to the averages of these quantities in the adjacent fluid cells. All other obstacle cells have zero values for  $F$  and  $p$ . No-slip boundary conditions are provided in cells adjacent to obstacle cells. This is specified by setting all velocities equal to zero inside obstacle cells.

## 3.7 Conditions for Numerical Stability

The explicit finite difference form for the momentum equations are subject to numerical instability unless certain stability criteria are satisfied. Once a mesh size has

been selected, the choice of the time step necessary for stability is governed by several restrictions. In this work, two conditions have been applied. First, the fluid cannot move through more than one cell in one time step. This criterion arises from the stability requirement for the advection term. From the Von Newman stability analysis, the time step must satisfy the following condition:

$$\Delta t \leq \min \left\{ \frac{\Delta x}{|u_{i,j}|}, \frac{\Delta y}{|v_{i,j}|} \right\} \quad (3.41)$$

The minimum of  $\Delta t$  is calculated with respect to every cell in the mesh. Second, when a nonzero value of the kinematic viscosity ( $\nu$ ) is used, momentum must not diffuse more than, approximately, one cell in one time step. This criterion arises from the stability requirement for the diffusion term. A linear stability analysis shows that this limitation implies that:

$$\Delta t \leq \frac{1}{2\nu} \frac{\Delta x^2 \Delta y^2}{\Delta x^2 + \Delta y^2} \quad (3.42)$$

### 3.8 Sloshing Force and Structure Response

As was mentioned in chapter two, when a TLD is coupled with a SDOF structure, the generated force by the water sloshing motion acts as a resisting or damping force to the external force. The coupled system is treated as a SDOF system subject to a total external force which is the sum of the damping force,  $F_{TLD}$  and the external force,  $F_e$ . The equation of motion of the coupled system is expressed as:

$$M_S \ddot{X}_S + C_S \dot{X}_S + K_S X_S = F_e + F_{TLD} \quad (3.43)$$

where  $M_s$  ,  $C_s$  and  $K_s$  are mass, generalized damping and stiffness respectively and  $X_s$  is structural displacement. The damping force due to water sloshing is calculated by applying momentum theory. The mass of each element is given by the following equation:

$$m_{ij} = \rho \cdot \Delta x_i \Delta y_j \quad (3.44)$$

The total momentum of the contained fluid can be described as:

$$P = \sum_{i=1}^{n_i} \sum_{j=1}^{n_j} m_{ij} u_{ij} \quad (3.45)$$

The damping force  $F_{TLD}$  can then be determined from the rate of change of the fluid momentum using the following equation:

$$F_{TLD} = \frac{1}{\Delta t} (P(t) - P(t + \Delta t)) \quad (3.46)$$

The Duhamel integral method [39] has been used to solve the equation of motion of the structure. This integral method can be used to determine the response of the SDOF system under any type of external excitations (harmonic and random). The total displacement of a damped SDOF system subjected to an external force  $F_t$  , can be expressed as:

$$X_s(t) = \frac{1}{M_s \omega_D} \int_0^t F_t(\tau) e^{-\xi \omega_n (t-\tau)} \sin \omega_D (t-\tau) d\tau \quad (3.47)$$

where  $F_t$  is the summation of the external excitation force and the TLD sloshing force and  $\omega_D$  is the damped frequency of the structure which is expresses as:

$$\omega_D = \omega_n \sqrt{1 - \xi^2} \quad (3.48)$$

$X_S(t)$  in equation (3.47) is the response for a damped system in terms of Duhamel's integral. The displacement is calculated by using a numerical integration of equation (3.47). For this purpose we use the trigonometric identity  $\sin \omega(t - \tau) = \sin \omega t \cos \omega \tau - \cos \omega t \sin \omega \tau$ , in Duhamel's integral. Then we obtain Duhamel's integral in the form:

$$X_S(t) = \frac{e^{-\xi \omega_n t}}{M_S \omega_D} \{A_D(t) \sin \omega_D t - B_D(t) \cos \omega_D t\} \quad (3.49)$$

where  $A_D$  and  $B_D$  can be evaluated from :

$$A_D(t_i) = A_D(t_{i-1}) + \int_{t_{i-1}}^{t_i} F_t(\tau) e^{\xi \omega_n \tau} \cos(\omega_D \tau) d\tau \quad (3.50)$$

$$B_D(t_i) = B_D(t_{i-1}) + \int_{t_{i-1}}^{t_i} F_t(\tau) e^{\xi \omega_n \tau} \sin(\omega_D \tau) d\tau \quad (3.51)$$

For a linear piecewise loading function, the forcing function  $F_t(\tau)$  is approximated by:

$$F_t(\tau) = F_t(t_{i-1}) + \frac{\Delta F_i}{\Delta t_i} (\tau - t_{i-1}), \quad t_{i-1} \leq \tau \leq t_i \quad (3.52)$$

where,

$$\Delta F_i = F_t(t_i) - F_t(t_{i-1}) \quad (3.53)$$

$$F_t(t_i) = F_e(t_i) + F_{TLD}(t_i) \quad (3.54)$$

$$\Delta t_i = t_i - t_{i-1} \quad (3.55)$$

This requires the evaluation of the following integrals:

$$I_1 = \int_{t_{i-1}}^{t_i} e^{\xi \omega_n \tau} \cos \omega_D \tau \, d\tau = \frac{e^{\xi \omega_n \tau}}{(\xi \omega_n)^2 + \omega_D^2} (\xi \omega_n \cos \omega_D \tau + \omega_D \sin \omega_D \tau) \Big|_{t_{i-1}}^{t_i} \quad (3.56)$$

$$I_2 = \int_{t_{i-1}}^{t_i} e^{\xi\omega_n\tau} \sin \omega_D \tau \, d\tau = \frac{e^{\xi\omega_n\tau}}{(\xi\omega_n)^2 + \omega_D^2} (\xi\omega_n \sin \omega_D \tau + \omega_D \cos \omega_D \tau) \Big|_{t_{i-1}}^{t_i} \quad (3.57)$$

$$I_3 = \int_{t_{i-1}}^{t_i} \tau e^{\xi\omega_n\tau} \sin \omega_D \tau \, d\tau = \tau - \frac{\xi\omega_n}{(\xi\omega_n)^2 + \omega_D^2} I_2 + \frac{\omega_D}{(\xi\omega_n)^2 + \omega_D^2} I_1 \Big|_{t_{i-1}}^{t_i} \quad (3.58)$$

$$I_4 = \int_{t_{i-1}}^{t_i} \tau e^{\xi\omega_n\tau} \cos \omega_D \tau \, d\tau = \left( \tau - \frac{\xi\omega_n}{(\xi\omega_n)^2 + \omega_D^2} \right) I_1 - \frac{\omega_D}{(\xi\omega_n)^2 + \omega_D^2} I_2 \Big|_{t_{i-1}}^{t_i} \quad (3.59)$$

In terms of these integrals,  $A_D(t_i)$  and  $B_D(t_i)$  may be evaluated from:

$$A_D(t_i) = A_D(t_{i-1}) + \left( F_t(t_{i-1}) - t_{i-1} \frac{\Delta F_i}{\Delta t_i} \right) I_1 + \frac{\Delta F_i}{\Delta t_i} I_4 \quad (3.60)$$

$$B_D(t_i) = B_D(t_{i-1}) + \left( F_t(t_{i-1}) - t_{i-1} \frac{\Delta F_i}{\Delta t_i} \right) I_2 + \frac{\Delta F_i}{\Delta t_i} I_3 \quad (3.61)$$

The substitution of equations (3.60) and (3.61) into equation (3.49) gives the displacement at time  $t_i$  as:

$$X_S(t_i) = \frac{e^{-\xi\omega_n t_i}}{M_S \omega_D} \{ A_D(t_i) \sin \omega_D t_i - B_D(t_i) \cos \omega_D t_i \} \quad (3.59)$$

## Chapter 4: Validation of the Numerical Model

This chapter presents 5 principal test cases for the algorithm, to validate its accuracy and dependability. Past literature and recent experimental results were used as references to test the algorithm for the water sloshing problem. This includes cases of TLDs without screens, with screens, and TLDs coupled to a vibrating structure.

### 4.1 The Broken Dam Problem

The first benchmark problem is the broken dam problem in which a rectangular column of water, originally under hydrostatic equilibrium, is confined between two vertical walls. The appearance of both vertical and horizontal free surfaces in this problem, provides a rigorous test of the capability of the algorithm to deal with free surfaces that are not single valued with respect to  $x$  or  $y$ . The water column is 1.0 unit wide and 2.0 units high, as shown in figure 4-1.

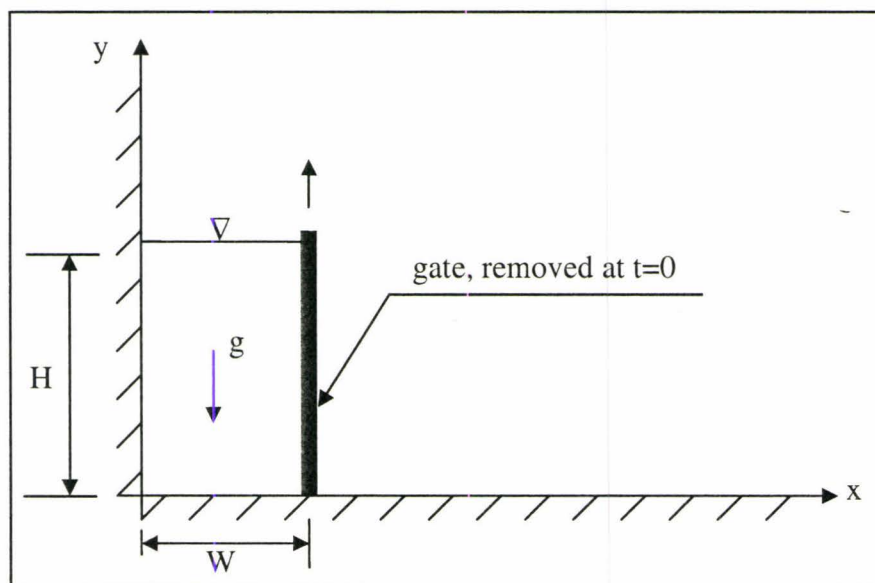


Figure 4-1: The layout of the broken dam problem.

Gravity is acting downwards with unit magnitude. At the beginning of the calculation, the right wall of the dam is removed suddenly and water is allowed to flow out along a dry horizontal floor. Experimental data of this problem have been reported [65] giving the position of the leading edge of the water surface as function of time as it flows to the right. The numerical results of the 2-D case are presented and compared with the experimental data in figures 4-2 and 4-3.

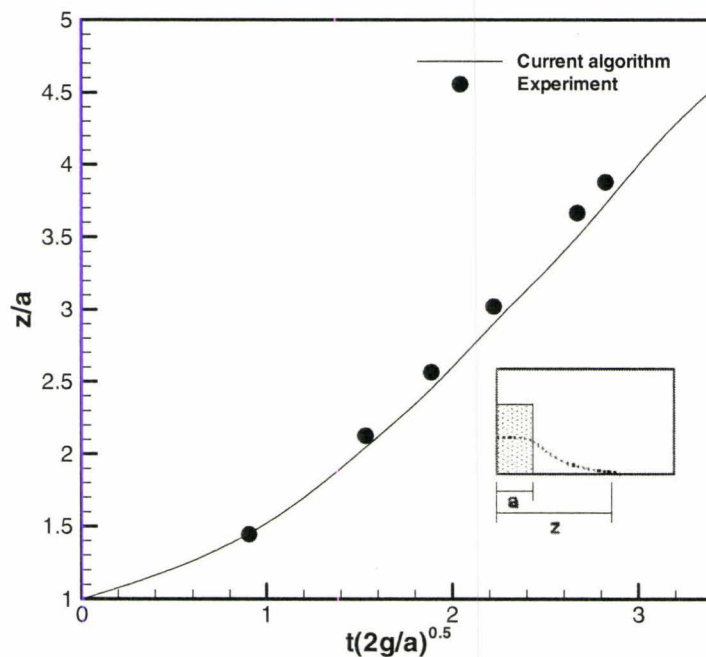


Figure 4-2: Horizontal position of free surface as function of time versus experimental data [65].

Figure 4-2, and 4-3 show the horizontal and vertical position of the free surface, respectively, as a function of time compared with the experimental data. Figure 4-4 shows the numerically predicted shape of the free surface using the present algorithm. The results presented in figures 4-2 and 4-3 show good agreement between the numerical

results and the experimental data. The uncertainty of experimental results has not been reported in the reference [65].

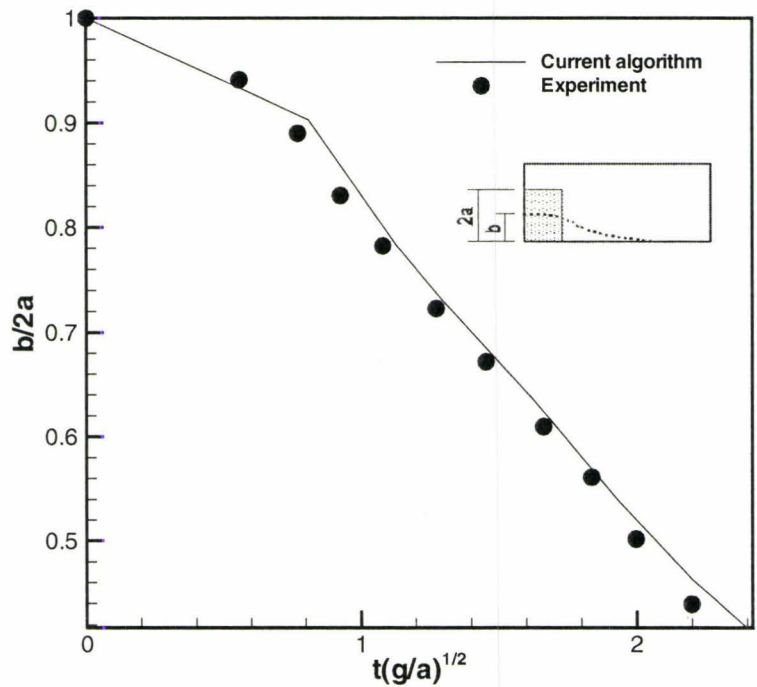


Figure 4-3: Vertical position of free surface as function of time versus experimental data [65].

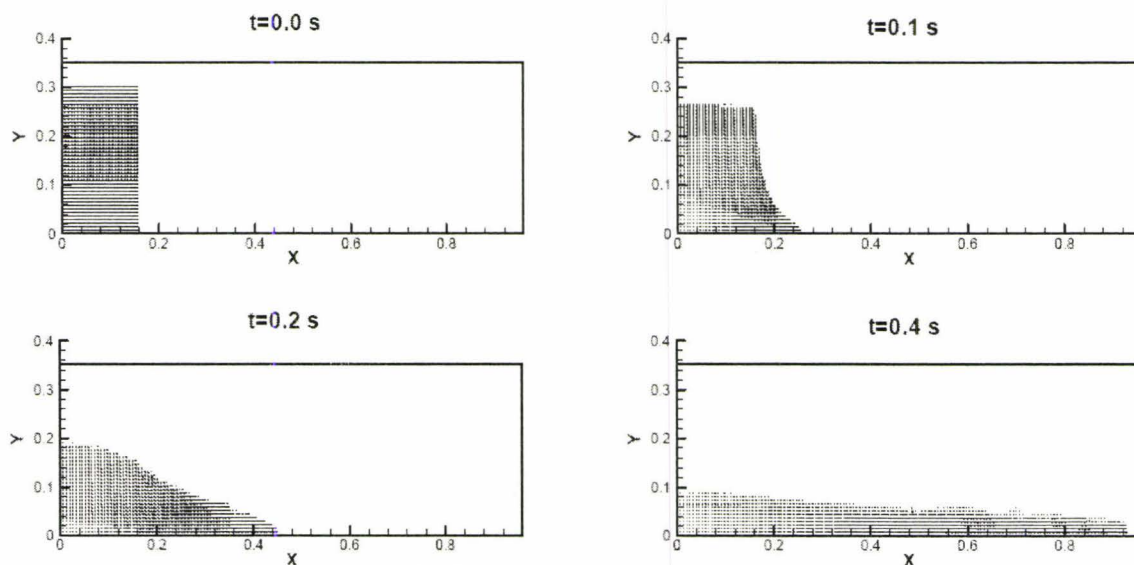


Figure 4-4: Free surface profile at various times.

## 4.2 Sloshing Motion of a Wave under the Effect of Gravity

The second test case is the problem reported in Raad et al [41], which is related to the sloshing motion of a low amplitude liquid wave under the influence of gravity. This problem is shown in figure 4-5. Initially the quiescent fluid has an average depth of 0.05 m, and its surface is initially defined by:  $y(x) = 0.05 + 0.005 \cos(\pi x/L)$ .

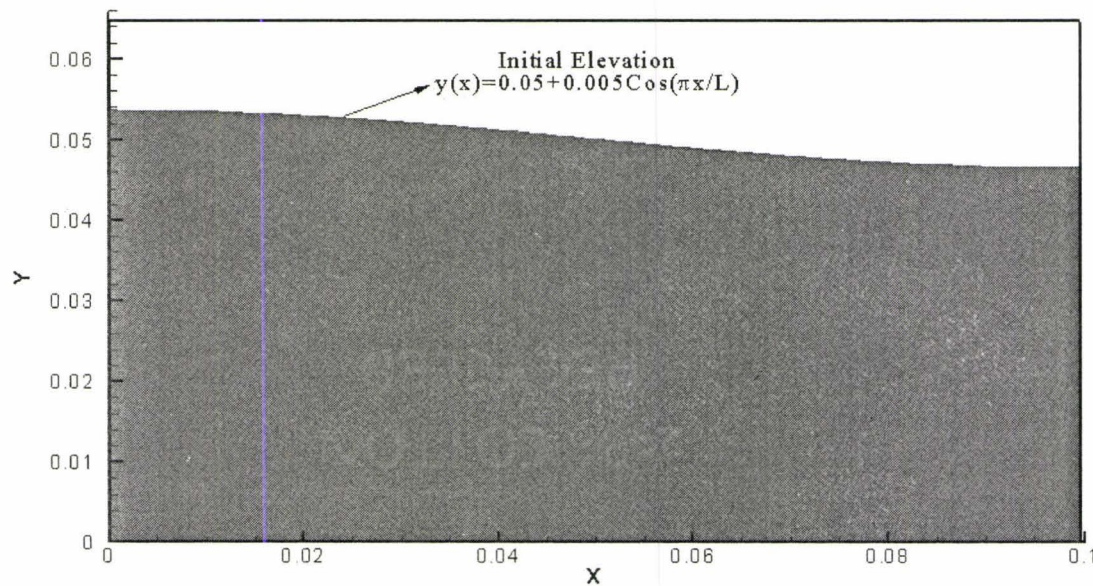


Figure 4-5: Initial geometry of the sloshing problem

The computational domain is a rectangle with width of 0.1 m and height of 0.065 m. The fluid begins to slosh solely under the influence of the gravitational field. The theoretical period of sloshing for the first mode is:

$$T = 2\pi \sqrt{gk \tanh(kh)} = 0.3739 \text{ s} \quad (4.1)$$

where  $k$  is the wave number and  $h$  is the average fluid depth.

Figure 4-6 shows the comparison between the theoretical results obtained in the literature, and the numerical results from the present algorithm. In both cases the height of the liquid free surface at the left boundary was captured, and again good agreement was found. The maximum discrepancy happened at about  $t=0.4$  s, which is 1.8% and insignificant.

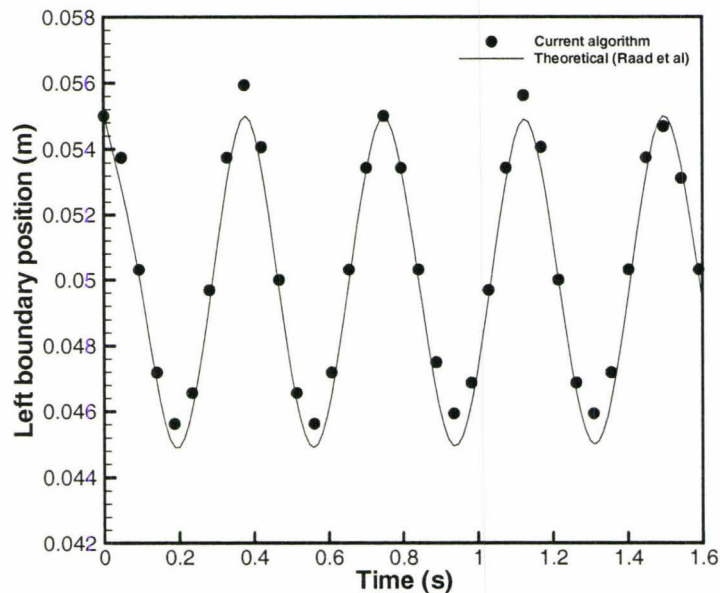


Figure 4-6: Position of the interface at the left boundary as a function of time

Figure 4-7 shows time captions of the developing free surface profile across one time period, using the present algorithm. As mentioned before, the system is initially at rest. After quarter of a period, the potential energy of the system has been transferred to kinetic energy and the fluid velocity reaches its maximum. After half a period, all the kinetic energy has been transferred back into potential energy and the fluid velocity goes back to zero.

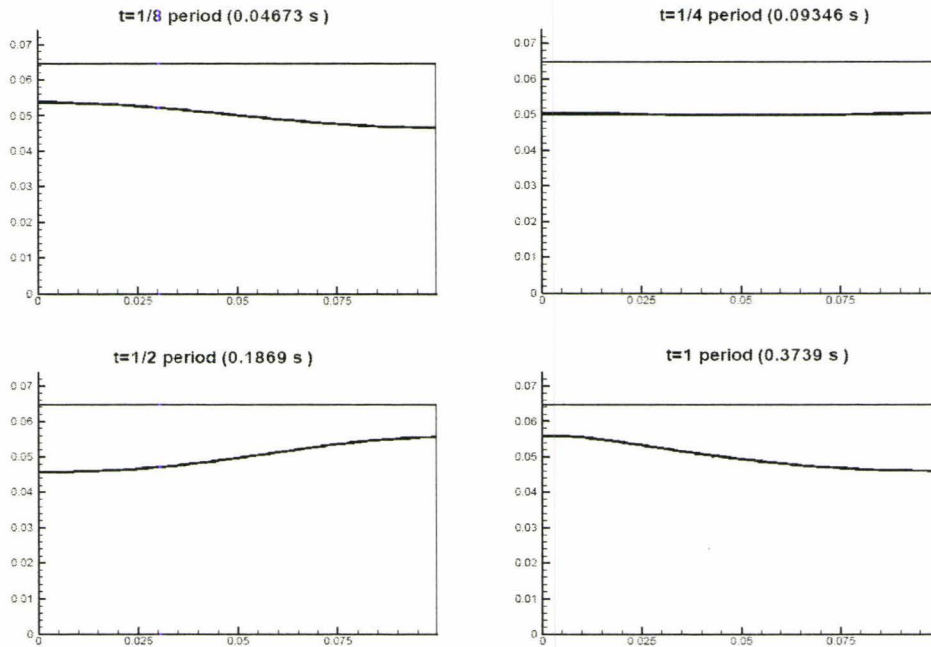


Figure 4-7: Development of the free surface during the first period of the sloshing motion.

### 4.3 Sloshing of a Shallow Layer in a TLD

The third problem is related to the sloshing motion of a shallow water layer in the TLD shown in figure 4-8. In this problem, the TLD is subjected to a sudden sinusoidal external excitation in the horizontal direction. As seen in figure 4-8, the tank is partially filled with water and is initially at rest.

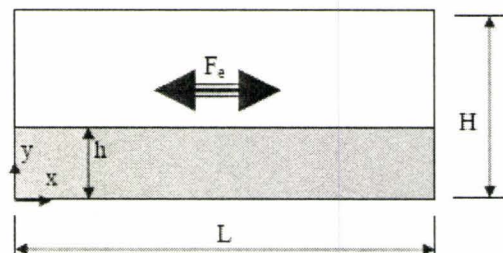


Figure 4-8: Model Problem - sloshing motion in a rectangle tank subjected to an external excitation.

$h$  is the fluid height,  $H$  is the tank height,  $L$  is the tank length,  $F_e$  is the excitation force.

The external excitation imposes a horizontal displacement given by  $X_e = A.Sin(\omega t + \varphi)$ , where  $A$ ,  $\omega$ , and  $\varphi$  are the amplitude, the frequency, and the phase angle of the forced oscillation, respectively.

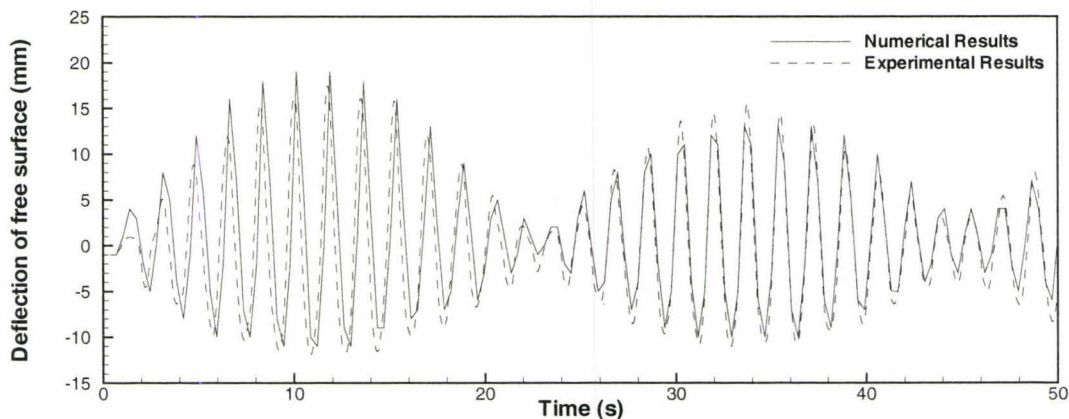
In the case presented here, the amplitude,  $A$ , the period of oscillation,  $T$ , and the phase angle,  $\varphi$ , were chosen as 0.259 cm, 1.681s, and 4.0 degrees, respectively. The initial depth of the liquid layer,  $h$ , is 0.119 m, and the tank width,  $w$ , is 0.966 m. In order to make it possible to compare with the experimental data, all these parameters have been selected similar to those used in [57].

All numerical simulations have been carried out for this case using a uniform grid of 200  $\times$  100 grid points. The dependence of the numerical results on the grid size has been checked and the 200 $\times$ 100 grid gave acceptable results. Table 4-1 shows the maximum difference for the free surface deflection at the three different mesh sizes relative to the selected mesh in this analysis.

**Table 4-1: Grid dependency analysis for TLD with no screen**

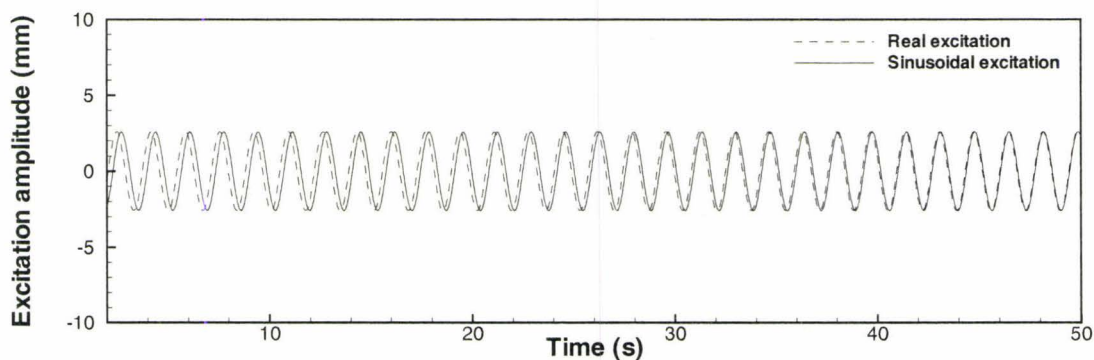
Mesh size	Maximum deviation
200x100	Selected mesh
160x80	1.8%
120x60	11%

Figure 4-9 shows the variation of the height of the free surface as a function of time at  $x = 0.05 \times L$ . The numerical results were in good agreement with the experimental data. The interfacial deformations depicted in figure 4-9 are about 20% of the original height of the liquid layer.



**Figure 4-9: Surface deformations at a location 5% of tank length from the left wall (i.e.,  $x=0.0483$  m) compare with experimental data reported in [57].**

A slight phase shift appeared between the experimental data and the numerical results presented in figure 4-9, and then disappeared after about 30 seconds. The reason for this has been investigated and found to be caused by a slight phase shift between the actual excitation used in the experiment and the one used in the numerical computations, see figure 4-10. In agreement with the results presented in figure 4-9, this phase shift disappeared after about 30 sec.



**Figure 4-10: The forced sinusoidal excitation used for code validation compared with the real excitation used in the experiment reported in [57].**

#### 4.4 Sloshing of a Shallow Layer in a TLD with a Slat Screen

The same configuration of the TLD used in the previous case has been considered in this test case to assess the effect of screens. Figure 4-11 shows the dimensions and location proposed for the slat screen. The height of each slat is 5 mm with 5 mm spacing between slats, and the first slat is placed at 3 mm from the bottom of the tank. Since the depth of the fluid in the tank is 119 mm, the screen has 12 slats. The thickness of each slat is 2.6 mm and the screen is located at the middle of tank.

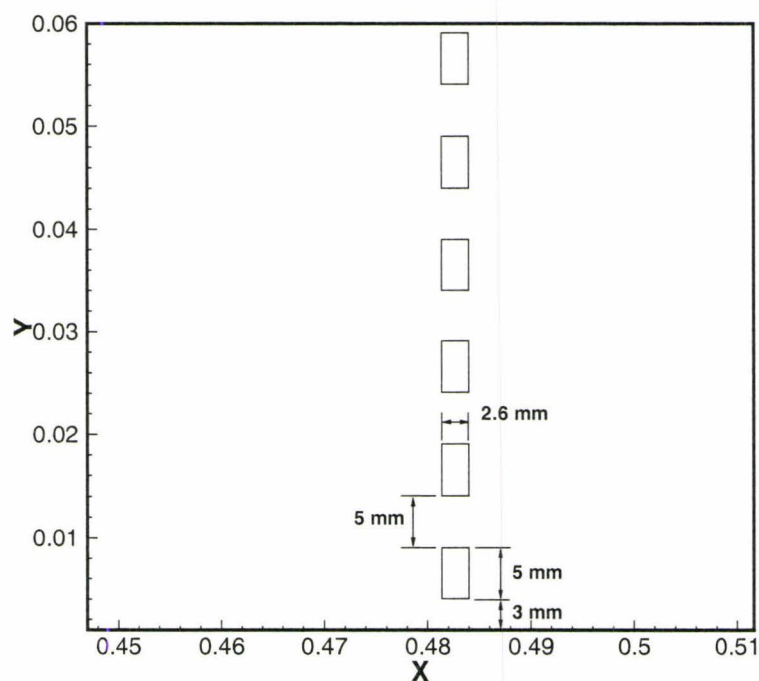


Figure 4-11: Slat screen layout.

The amplitude,  $A$ , the period of oscillation,  $T$ , and the phase angle,  $\phi$ , were chosen as 0.259 cm, 1.681s, and 0.0 degrees, respectively. All parameters have been selected according to the experiments carried out by Tait [57]. Numerical simulations of

this case have been carried using a non-uniform grid in the x- direction and a uniform grid in y- direction. The non-uniform mesh has been designed such that more grids are located around the screen.

A grid dependence test has been carried out. A  $260 \times 200$  mesh gave acceptable results. Table 4-2 shows maximum difference in the free surface deflection obtained using three mesh sizes.

**Table 4-2: Grid dependency analysis for TLD with screen**

Mesh size	Maximum deviation
260x200	Selected mesh
200x200	0.5%
150x200	2.0%

Figure 4-12 shows the variation of the height of the free surface at  $x = 0.05 \times L$  for both cases of TLD with and without the screen. As expected, using the screen increased the damping effect, thus eliminated the beating phenomena of the free surface and resulted in a more linear and controllable sloshing motion. Figure 4-13 clearly indicated that the numerical results are in good agreement with the experimental data. The unsymmetrical results around the time axis in figure 4-13 could be attributed to the ideal flow assumption at the free surface location. After about 18 seconds, both the experimental and the numerical results showed a linear behavior of the sloshing motion and a constant deformation of the free surface. A slight phase shift appeared between the experimental and the numerical results. This shift, similar to the previous test case, was caused by a slight phase shift between the actual excitation used in the experiment and the one used in the numerical computations, see Figure 4-10.

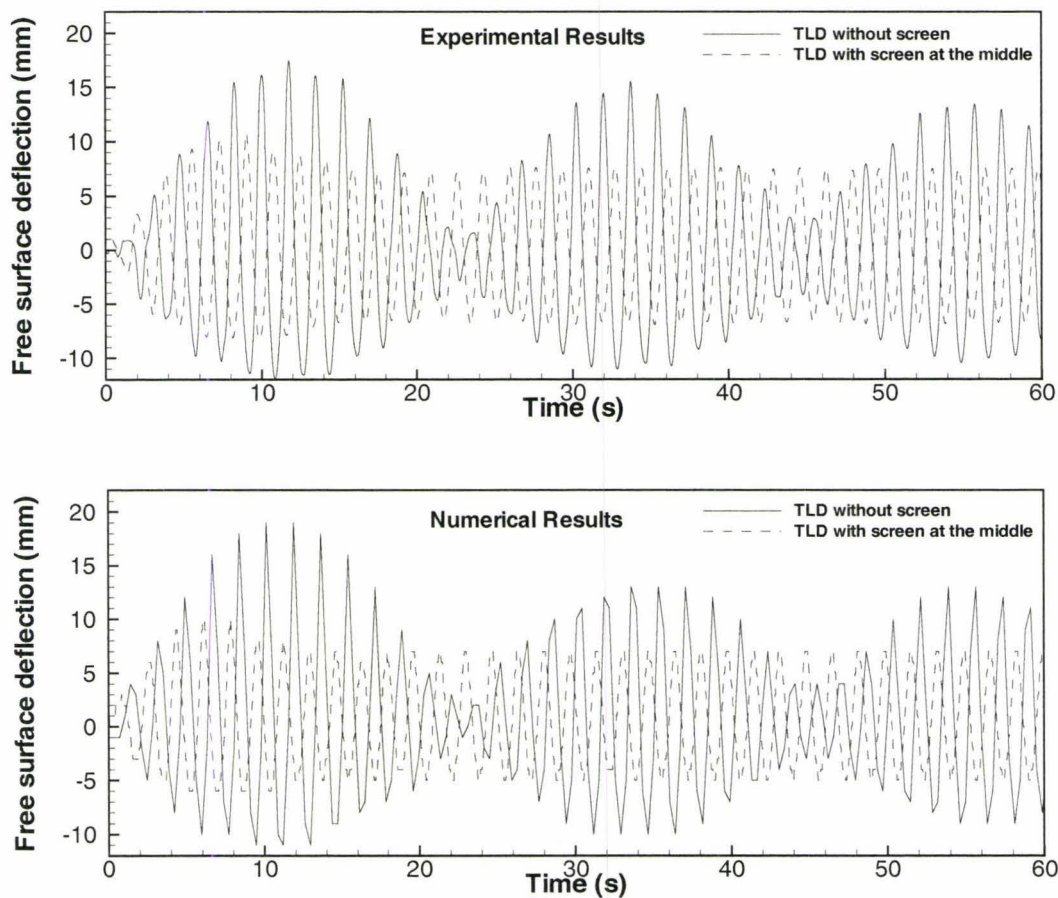


Figure 4-12: Comparison between measured [57] and predicted surface deformations at  $x = 0.0483$  m for the cases of the TLD without and with a screen.

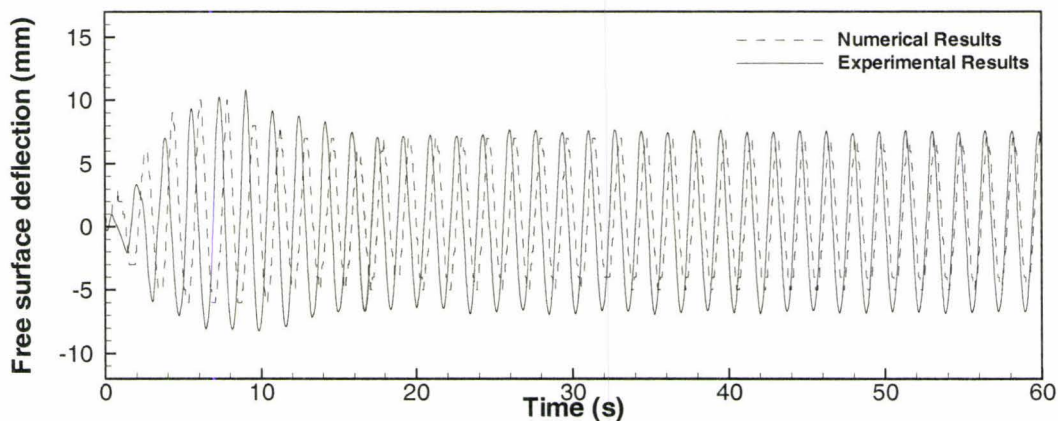


Figure 4-13: Comparison between measured [57] and predicted surface deformations at  $x = 0.0483$  m for the case of the TLD with a screen.

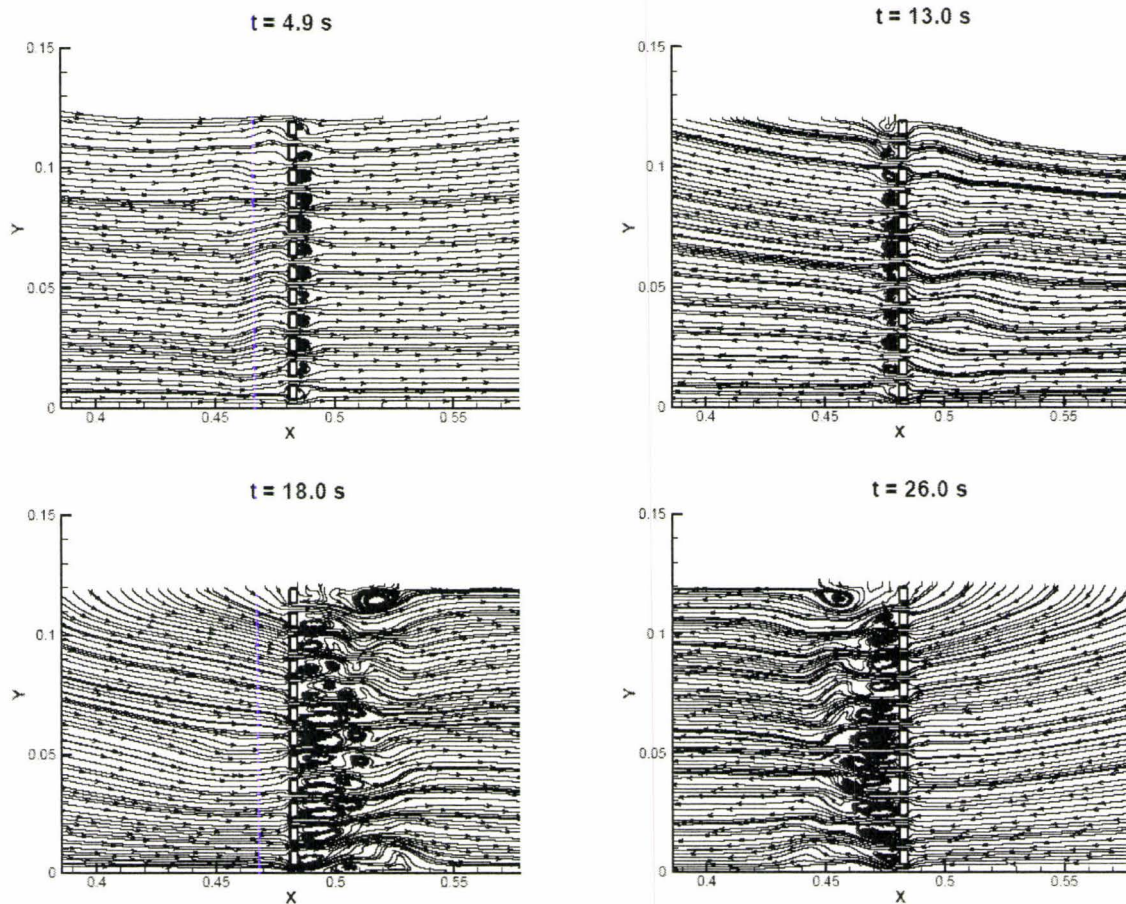


Figure 4-14: Details of the flow through the screen at various times.

One should note that in the case of no screen, figure 4-12, the level of surface deformations encountered ranged between + 15% and – 10% of the original liquid layer depth, indicating the capability of the present algorithm of capturing large interfacial deformations.

The details of the flow through the screen at four instances in time are shown in figure 4-14. At  $t = 4.9$  seconds, the liquid was moving from left to right and a set of vortices formed to the right of the screen. At  $t = 13.0$  seconds, the flow reversed direction and the vortices formed on the left side of the screen. As time progresses, the same

alternating pattern of the locations of the vortices can be seen at  $t = 18.0$  and  $26.0$  seconds. However, the size of the vortices and the complexity of the flow structure increased significantly. These results of the flow details indicate quite clearly that the screen pattern would have a significant effect on the sloshing motion and on the damping efficiency of the TLD, which is in agreement with the results reported recently by Hamelin [18]. A thorough investigation of the effect of screen pattern using the present algorithm has been studied in chapter 5.

#### 4.5 TLD-Structure Interaction

This case study validates the developed TLD-structure model. Figure 4-15 shows the schematic of the proposed system.

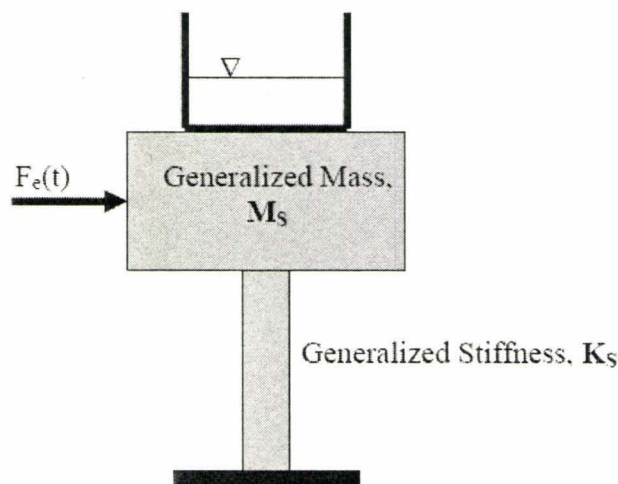


Figure 4-15: Schematic of TLD-Structure Model.

Again, all parameters have been selected according to the experiments carried out by Tait [57]. In this study, the structure was assumed to be a single degree of freedom (SDOF) system with properties listed in table 4-3.

**Table 4-3: Structure properties**

$M_s$ (Kg)	$K_s$ (N/m)	$\xi$ (%)	$\mu$ (%)
4480	55100	0.1	2.5

The TLD that was coupled to this structure had the properties listed in table 4-4 with the dimensions shown in figure 4-16.

**Table 4-4: TLD properties**

L (m)	H (m)	h (m)	$f_w$ (Hz)
0.966	0.3	0.119	0.545

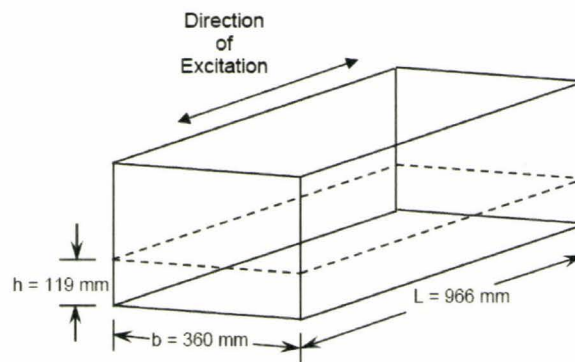
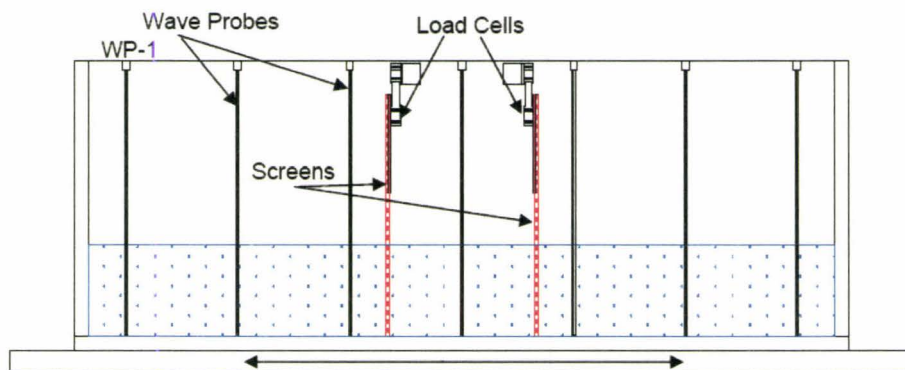
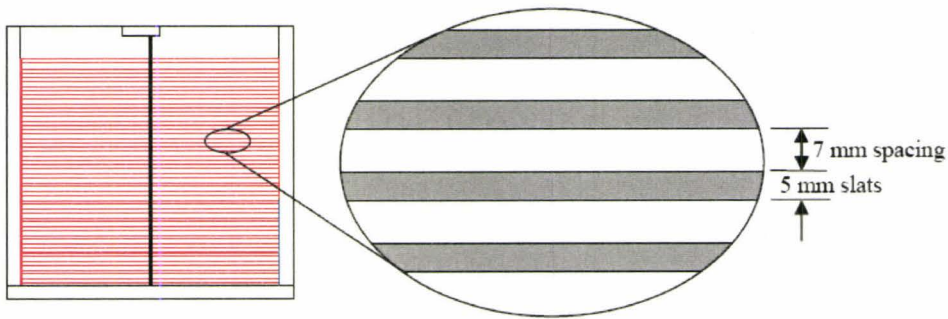
**Figure 4-16: Schematic of TLD used in the experiment [57].**

Figure 4-17 shows the tank set up side view of tank for this experiment.

**Figure 4-17: Tank set-up side view [57].**

Two identical screens with solidity ratio of 0.42 have been installed in the TLD at 40% and 60% of tank length ( $L$ ), as shown in figure 4-17. The solidity ratio ( $S$ ) is defined as the ratio of the solid projected area of the screen to the total screen projected area. The slat height is 5 mm with 7 mm spacing between them, and the thickness of each slat is 1 mm. Figure 4-18 shows a closer look at the slat configuration.



**Figure 4-18: Damping screen [57].**

A  $280 \times 200$  mesh has been employed for this numerical analysis. The mesh is non-uniform (with finer grid size around the screens) in the  $x$ - direction and uniform in the  $y$ - direction. The minimum  $\Delta x$  of 1mm has been selected for this analysis. The TLD-structure system is subjected to random external force, as shown in figure 4-19.

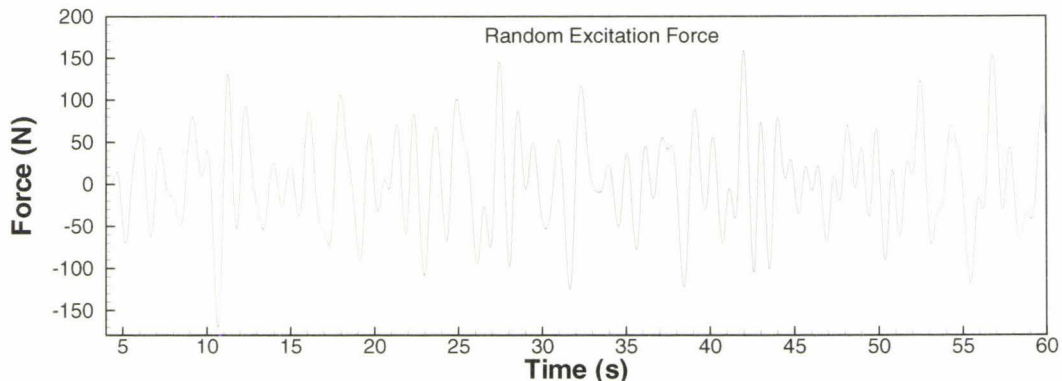


**Figure 4-19: External excitation function [57].**

Figure 4-20 shows both experimental and numerical normalized free surface deflections ( $\lambda = \frac{dh}{h}$ ) at  $x=0.0483\text{m}$ . Results indicate excellent agreement between the numerical and the experimental results.

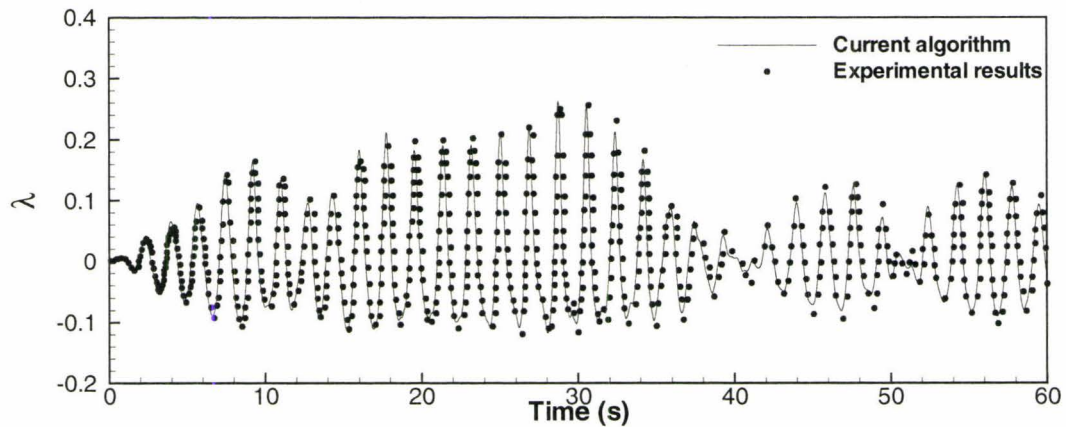


Figure 4-20: Comparison of experimental [57] and numerical time histories of free surface response at  $x=0.0483\text{ m}$ .

Figures 4-21 and 4-22 show the time history of normalized sloshing force and structural acceleration, respectively. In both cases, excellent agreement between the numerical and the experimental results has been found.

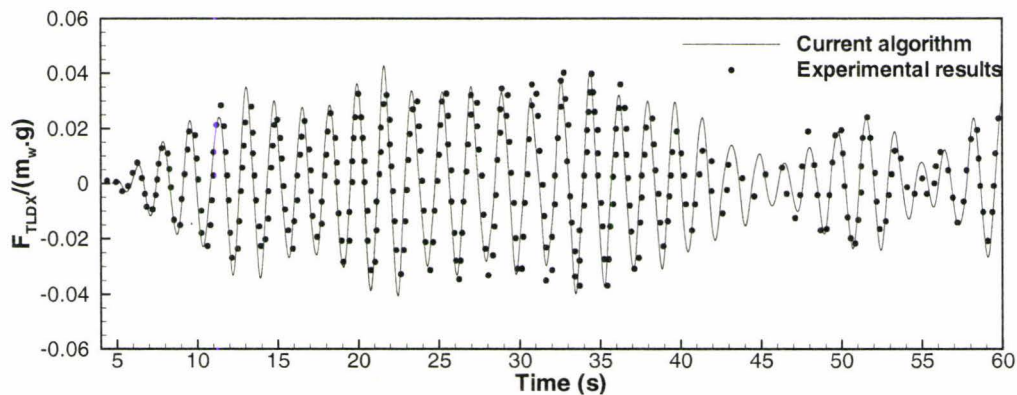


Figure 4-21: Comparison of experimental [57] and numerical normalized TLD force.

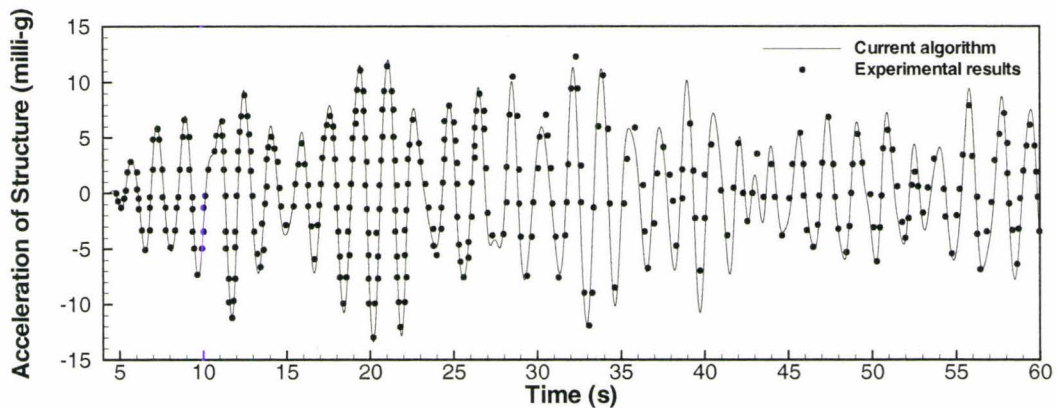


Figure 4-22: Comparison of experimental [57] and numerical structural acceleration time histories.

The performance of a TLD is often treated by analogy with a TMD. The TMD parameters are usually determined by matching the energy dissipation or the shear force produced by the TLD with that produced by an equivalent single degree of freedom TMD. The energy dissipation or the shear force produced by the TLD is usually determined experimentally. Numerical results of the present algorithm have been compared with results of an equivalent amplitude dependent TMD model [57] and the one obtained experimentally [57]. Parameters of the equivalent TMD model were obtained experimentally [57]. The TMD parameters were determined by matching the energy dissipated by the TLD and by an equivalent single degree of freedom TMD. The current TLD was exposed to a sinusoidal excitation with amplitudes equal to 2.5 mm and 12.5 mm without interaction with the structure. Figures 4-23 and 4-24 show the normalized sloshing force ( $F'$ ) as a function of the excitation frequency for the two amplitudes. The sloshing force has been normalized by the inertia force of the liquid

treated as a solid mass,  $m\omega^2 A$ . The excitation frequency ratio,  $\beta_w$ , is the ratio of the frequency of excitation to the natural frequency of the TLD calculated from the linear wave theory according to the following equation:

$$f_w = \frac{1}{2\pi} \sqrt{\frac{\pi g}{L} \tanh\left(\frac{\pi h}{L}\right)} \quad (4.2)$$

Substituting L and h into the above equation, leads to value of  $f_w \approx 0.545$  Hz.

Figure 4-23 and 4-24 show a comparison of the normalized sloshing force calculated by the present numerical model, the measured sloshing force reported in [57], and the estimated base shear force obtained using the equivalent TMD model [57]. In both small and large amplitude cases, the agreement between the present model and the experiment is excellent. However, results of the equivalent TMD model, especially in the case of large amplitude of excitation, did not produce satisfactory results. Figures 4-23 and 4-24 clearly indicate that the present numerical model can be used to carry out an extensive investigation of the performance of any TLD using the TMD analogy. The uncertainty of the experimental data has not been reported in [57].

The good agreement between the numerical and experimental results has justified the laminar flow assumption. However, the  $K - \varepsilon$  turbulence model added to RIPPLE by Lin (1997) was used for this TLD-Structure system. Results for free surface deflection, pressure drop at screen, sloshing force and acceleration of structure were almost identical. Therefore the flow has been assumed to be laminar in this study.

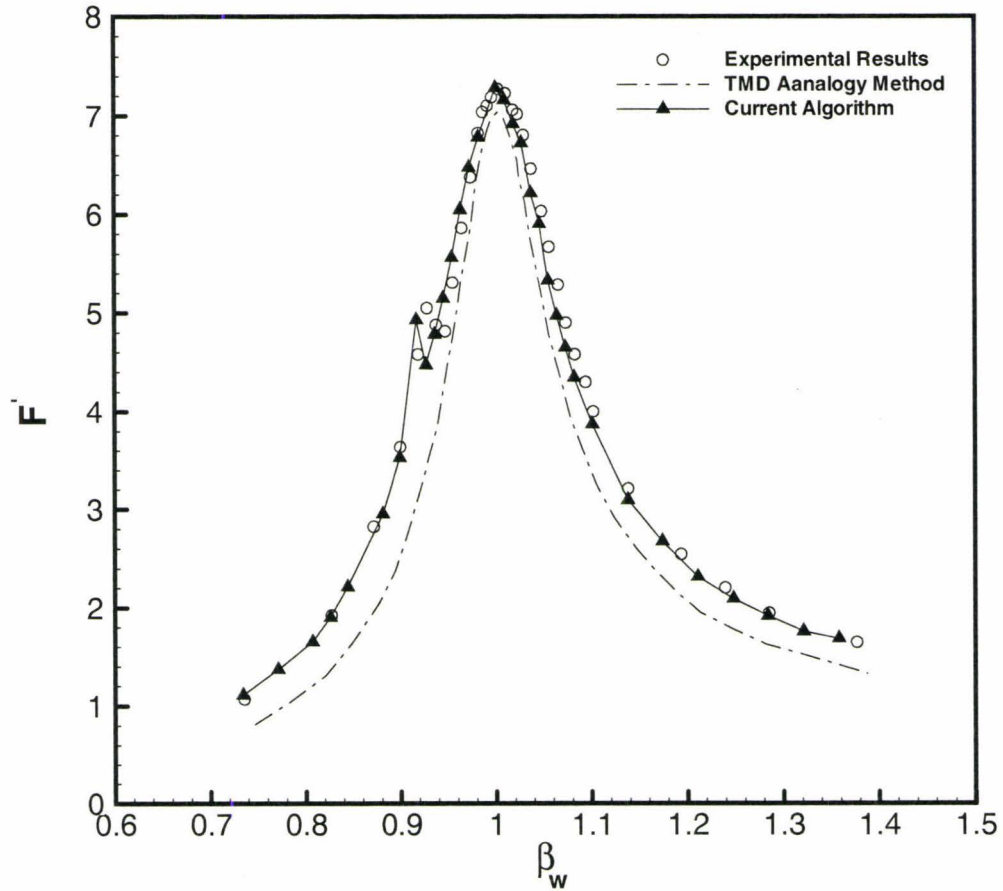


Figure 4-23: Variation of the normalized sloshing force  $F$ , as function of excitation frequency ratio  $\beta_w$ . Comparison between results of experiments [57], equivalent TMD analogy [57], and present numerical model at amplitude of excitation of 2.5 mm.

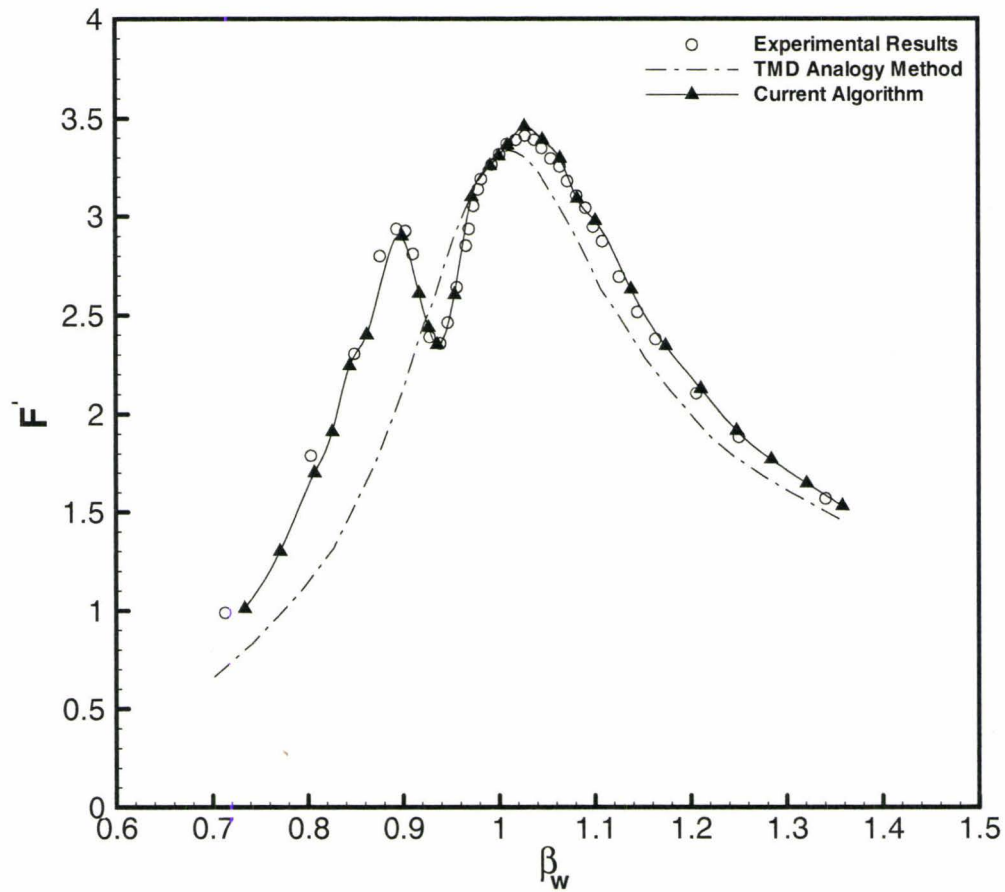


Figure 4-24: Variation of the normalized sloshing force  $F$ , as function of excitation frequency ratio  $\beta_w$ . Comparison between results of experiments [57], equivalent TMD analogy [57], and present numerical model at amplitude of excitation of 12.5 mm.

## Chapter 5: Numerical Results

### 5.1 Introduction

The objective of this chapter is to present numerical results obtained using the algorithm developed and validated in chapters 3 and 4 to investigate the effect of the following:

1. Effect of the TLD on structural response.
2. Effect of slat screens on TLD performance and on structural response.
3. Effect of screen pattern on TLD performance and on structural response.
4. Effect of screen pattern on the pressure drop of slat screen in the TLD.
5. Effect of screen pattern on natural frequency of the TLD.

In this chapter results obtain for various cases of TLD configuration are presented to understand the nature of the sloshing motion inside the TLD, whether a screen is present or not. The present algorithm has made it possible to fully resolve flow through screens, and hence allowed for a better assessment of pressure drop due to screens. A new parameter, the screen slat ratio (SR), has been proposed and introduced in the present study to account for the effect of slat screen pattern, which has never been accounted for before. The slat ratio (SR) has been used to examine the validity of the Baines and Peterson model [2] for the calculation of pressure ( $\Delta p$ ) drop through the screen. A correction factor has been proposed and developed to extend the applicability of Baines and Peterson model taking into account the effect of the screen pattern on the calculation of pressure drop through the screen.

## 5.2 TLD Performance without Screens

### 5.2.1 TLD Subjected to Harmonic Excitation

In this section, the effect of TLD on structure response without any screens is discussed. All cases presented in this chapter are for the same TLD and structure properties mentioned in tables 4-3 and 4-4. Figure 5-1 shows a TLD with  $h=0.119\text{m}$ ,  $L=0.966\text{m}$ . The TLD is subjected to a harmonic excitation,  $X_e = A \sin(2\pi f t)$ , where  $A$ , the amplitude of excitation is 10 mm and  $f$ , frequency of excitation, is 0.545 Hz which is the natural frequency of this TLD according to equation 4.2. Since the purpose of this analysis is not to study the effect of the amplitude of excitation, 10 mm has been selected as a value between small (2.5 mm) and large amplitude (more than 20 mm).

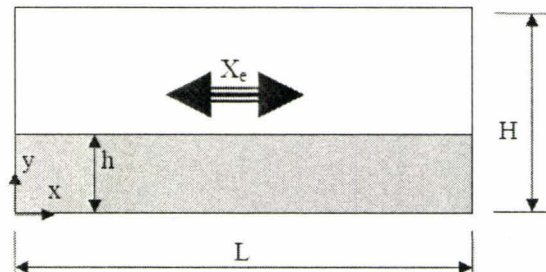


Figure 5-1: The TLD configuration

First, the structure response was calculated for the case without a TLD and then the response of the structure coupled with the TLD was calculated. Figure 5-2 shows the structure responses in term of its top displacement with and without the TLD. The results show that the TLD has decreased the structure response by up to 67%.

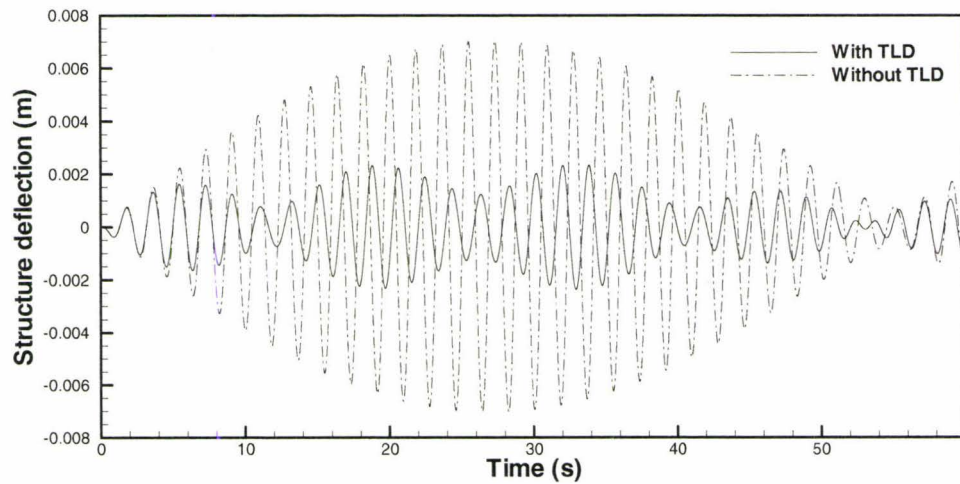


Figure 5-2: The response of the structure with and without the TLD

This reduction is because of the damping effect of the TLD. The damping effect of the TLD is due to the generated sloshing force which acts anti-phase to the external excitation force as shown in figure 5-3.

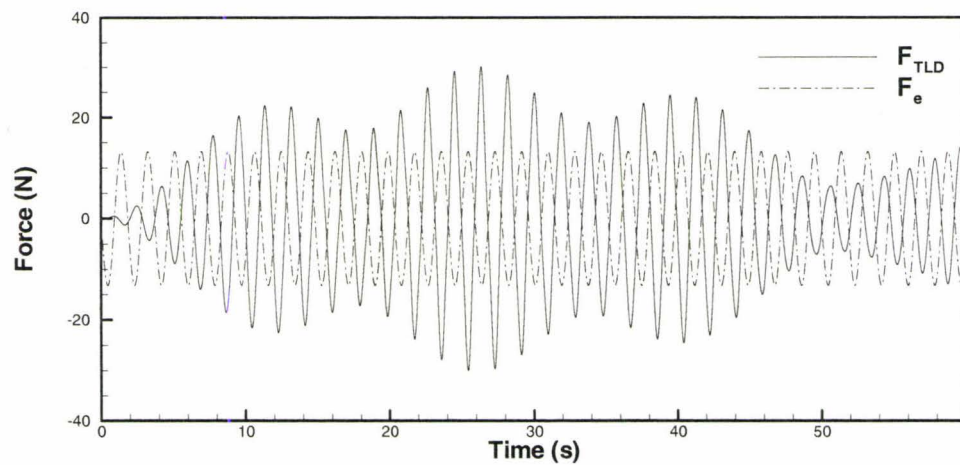
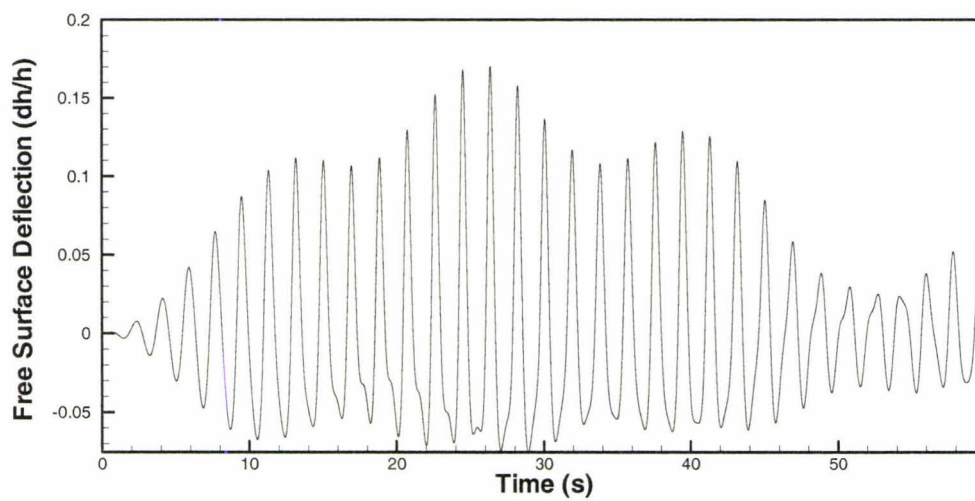


Figure 5-3: Time history of the sloshing force ( $F_{TLD}$ ) and the excitation force ( $F_e$ )

Following the trend of sloshing force with time and comparing it with the trend of the structure deflection during the same time interval, it is clear that the sloshing force, which is acting anti-phase to the excitation force, reduced deflection of the structure. The mechanism of generating the sloshing force in the TLD is the rate of momentum change of the fluid. The change of momentum is imposed on the flow field by the side walls. Therefore, it is expected that the maximum deflection of the free surface would occur at the side walls of the tank when the maximum sloshing force is gained. The sloshing force has been calculated according to equation (3.46) and the external excitation force would have a harmonic with the amplitude of  $A(2\pi f)^2 m$  where  $A$  and  $f$  are the amplitude and frequency of excitation. This fact is shown in figure 5-4 which illustrates the time history of free surface deflection at  $x = 0.05 \times L$ . It was observed in this figure that during the whole TLD operation, the maximum deflection of the free surface corresponded to the maximum generated sloshing force shown in figure 5.3.



**Figure 5-4:** Time history of the free surface deflection at  $x = 0.05 \times L$ .

Figure 5-5 shows clearly when the maximum deflection of free surface is happened at  $x=0.05 \times L$ , the fluid height at the rest of the TLD would be less than it.

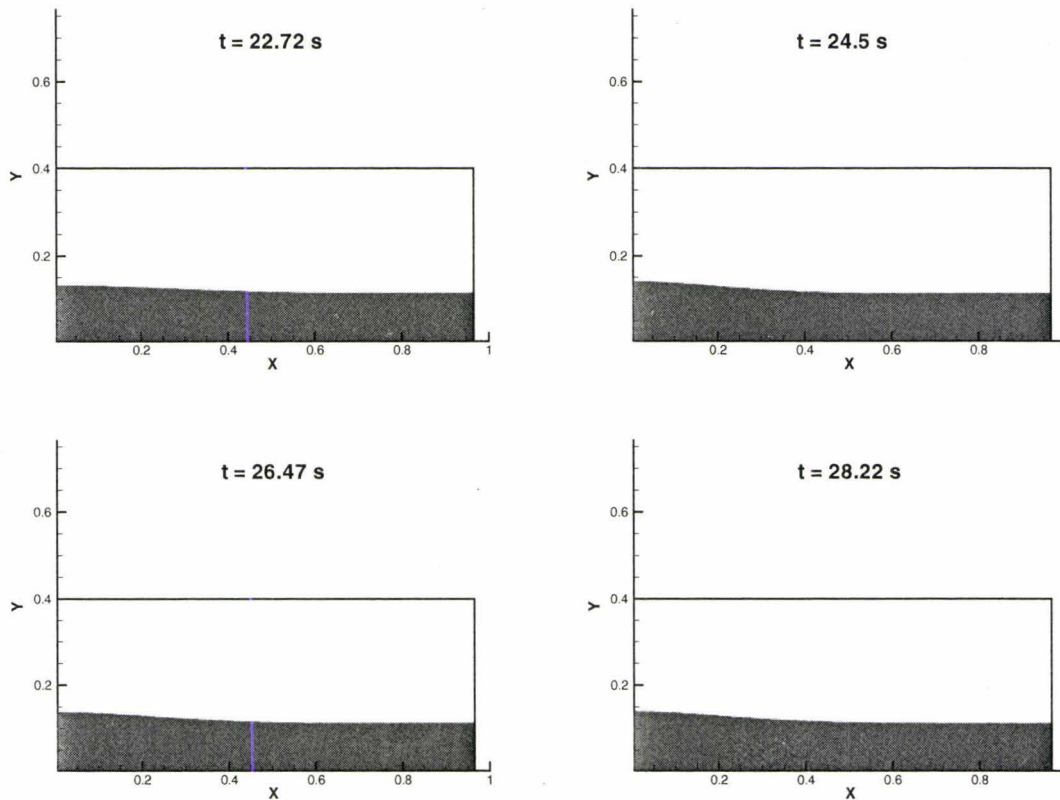


**Figure 5-5: Free surface profile in TLD at selected times which fluid height at the left side is maximum**

Figure 5-4 also shows that the maximum deflection of the free surface could reach to more than 15% of the initial fluid depth. Due to the low damping of the TLD, the deflection of free surface will experience a beating phenomenon in which case the maximum deflection of the free surface is not constant with time. This phenomenon is not desirable because it makes the behavior of the TLD unpredictable. Figure 5-4 shows clearly this beating phenomenon. To eliminate this phenomenon, the inherent damping of

the TLD should be increased. The introduction of screens into a TLD has been considered as a method to increase the inherent damping of the TLD. It can reduce or even diminish this beating phenomenon and cause the sloshing motion inside the TLD to be more linear and predictable. It also reduces the structure response. Figure 5-6 shows the streamlines showing the flow pattern inside the TLD at different times.

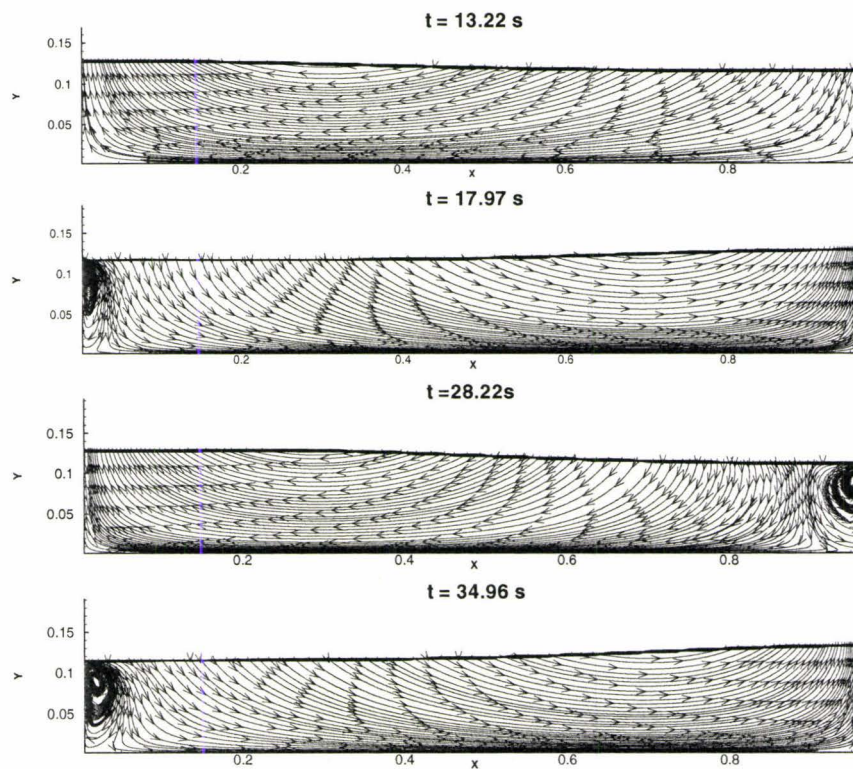


**Figure 5-6: Free surface profile and streamlines showing the flow pattern at different times**

The times shown in figure 5-6 are the times at which the free surface elevation became maximum at the side walls. The flow patterns show that when the free surface deflection reached its maximum value at one side of the tank, a recirculation zone was observed at the other side of the tank. This observation suggests that using different

shapes for the corners of the tank, might increase the amount of fluid mass inside the TLD which might increase the TLD damping effect.

## 5.2.2 TLD Subjected to Random Excitation

Typically, the case of wind loading on a structure corresponds to a harmonic external excitation. In the case of an earthquake, the excitation function is not harmonic and would be random. In order to investigate how a TLD can affect the structure response under earthquake conditions, the TLD-structure system has been subjected to the random excitation function shown in figure 4-19. This random excitation function has been considered for all random excitation cases presented in this chapter.

The response of the structure without and with a TLD is compared in figure 5-7. Again a reduction in the structure response by up to 88% was obtained using a TLD. However the beating phenomenon which was discussed earlier still exists.

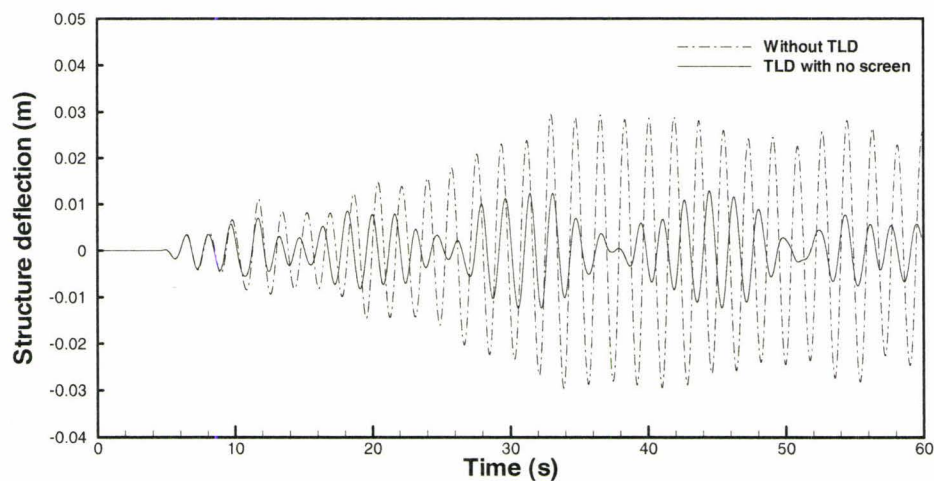
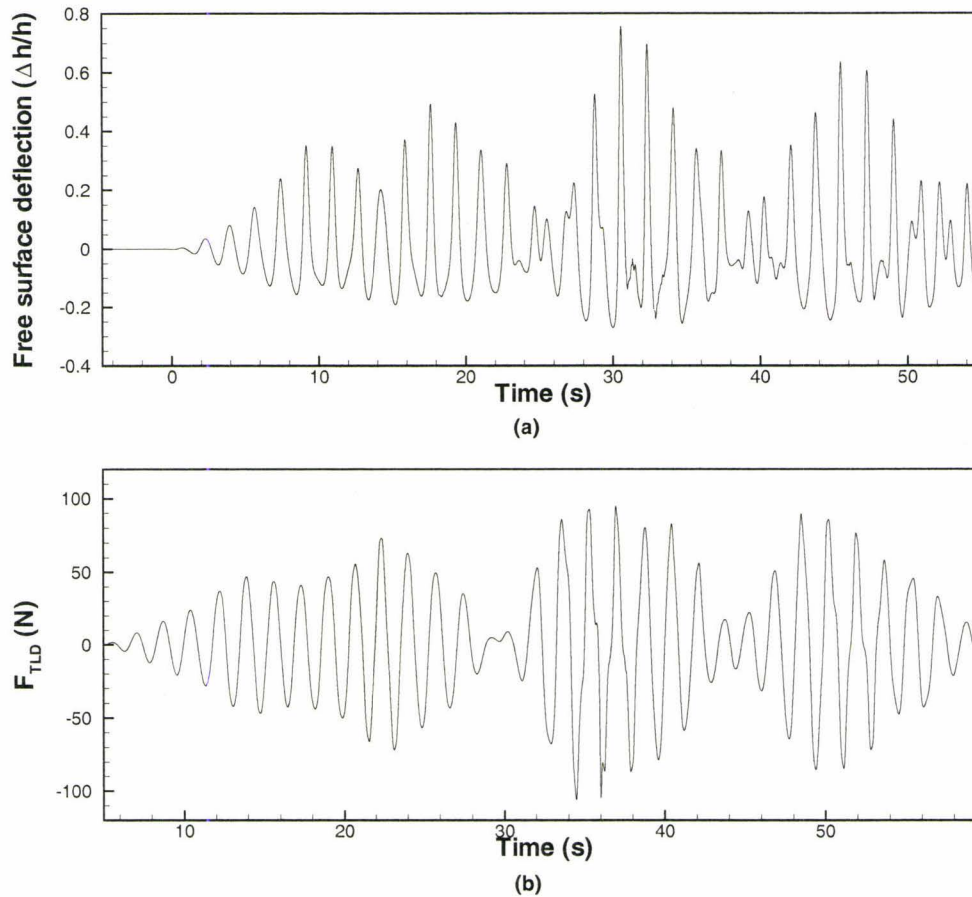


Figure 5-7: The response of the structure with and without TLD for random excitation

The time history of the sloshing force and the free surface deflection at  $x = 0.05 \times L$  are shown in figure 5-8. The non-uniformity in the amplitude of the free surface deflection can be observed clearly in this figure.



**Figure 5-8: Time history of (a) the free surface deflection at  $x=0.05 \times L$  and (b) the sloshing force**

The maximum deflection of the free surface in this case reaches up to 75% of the initial depth of water, which is extremely high. The minimum deflection of the structure corresponds to the maximum deflection of the free surface at the side wall and so it corresponds to the maximum sloshing force.

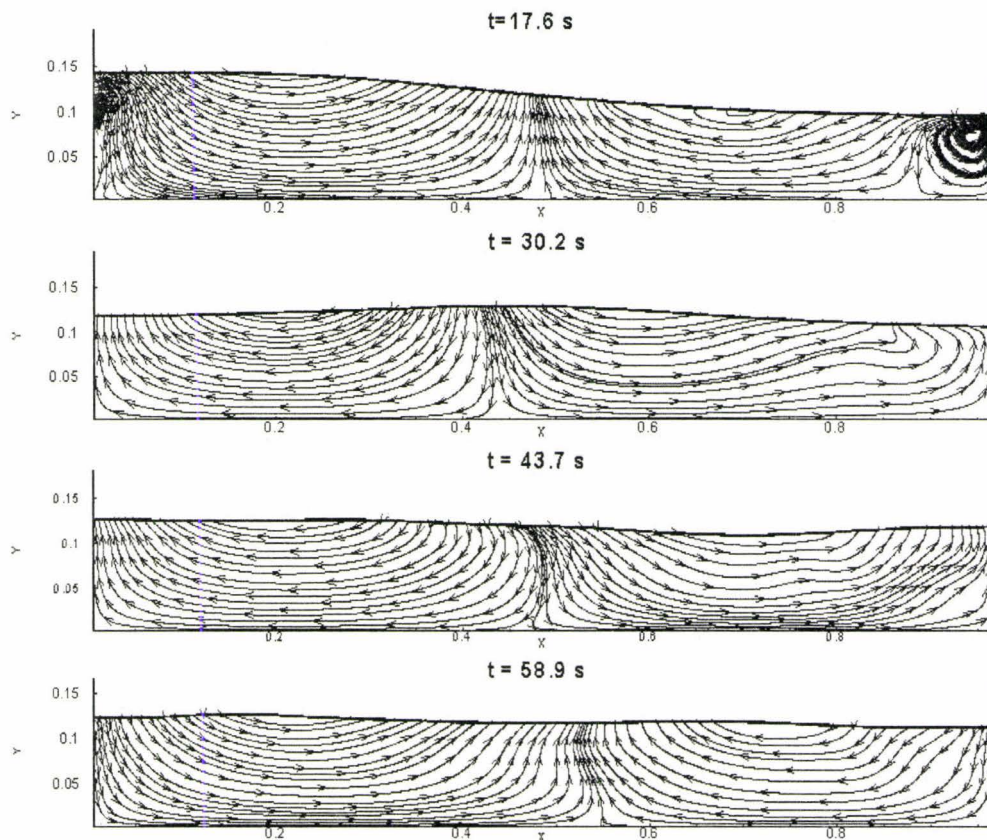


**Figure 5-9: Free surface profile and streamlines showing the flow pattern at different times**

The times shown in figure 5-9 are those at which the maximum sloshing force is minimized. The flow patterns show that in addition to a recirculation zone formed at the side of the tank, two masses of fluid move opposite to each other. The overall effect of this phenomenon is less flow contributed in the sloshing motion and hence the sloshing force decreased.

The beating phenomenon which was observed in the time history of the free surface deflection and sloshing force in both random and harmonic excitations is an undesirable phenomenon. The lack of sufficient inherent damping of the TLD is the main

source of this phenomenon. The major solution of this problem is to increase the inherent damping by using additional damping devices in the TLD. In this research, the slat screens have been chosen to achieve that. In the next section the effect of slat screens on the performance of the TLD is presented and discussed.

### 5.3 Effect of Slat Screen on TLD Performance and Structure Response

#### 5.3.1 TLD-Structure System Subjected to Harmonic Excitation

Results presented here are for a TLD equipped with one slat screen placed in the middle, as shown in figure 5-10. A screen is usually characterized by its solidity ratio ( $S$ ). The solidity ratio ( $S$ ) is defined as the ratio of the solid area of the screen to the total screen area, that is:

$$S = \frac{A_s}{A_t} \quad (5-1)$$

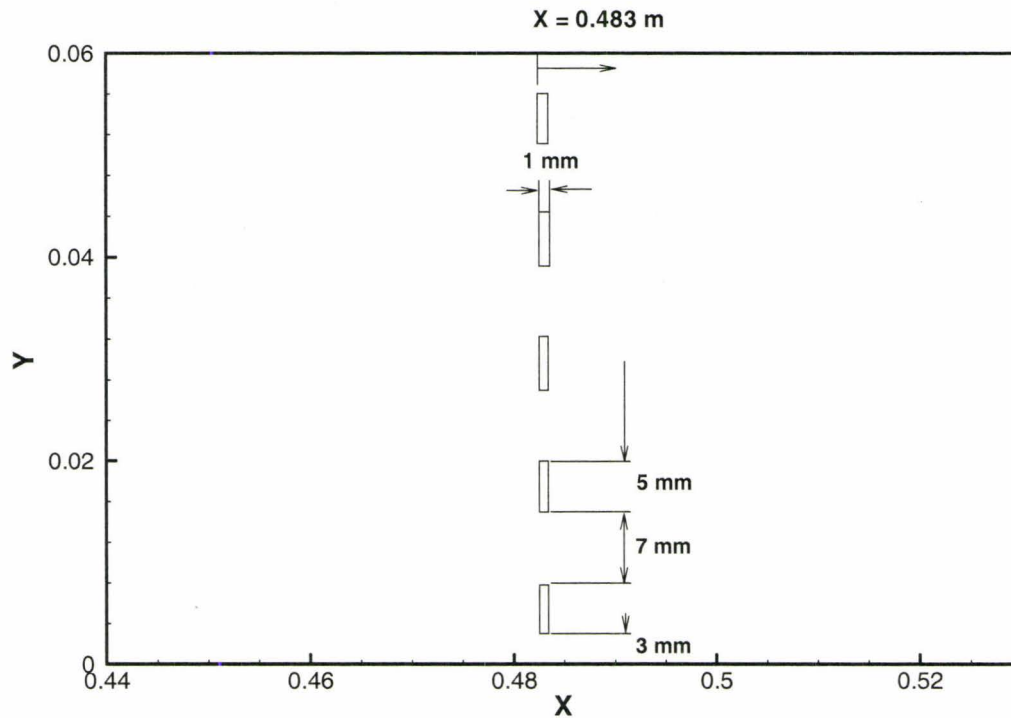
In the case of a slat screen,  $S$  could also be defined as:

$$S = \frac{n.D}{h} \quad (5-2)$$

where  $n$  is the number of slats,  $D$  is the slat height and  $h$  is the fluid height in the TLD tank.

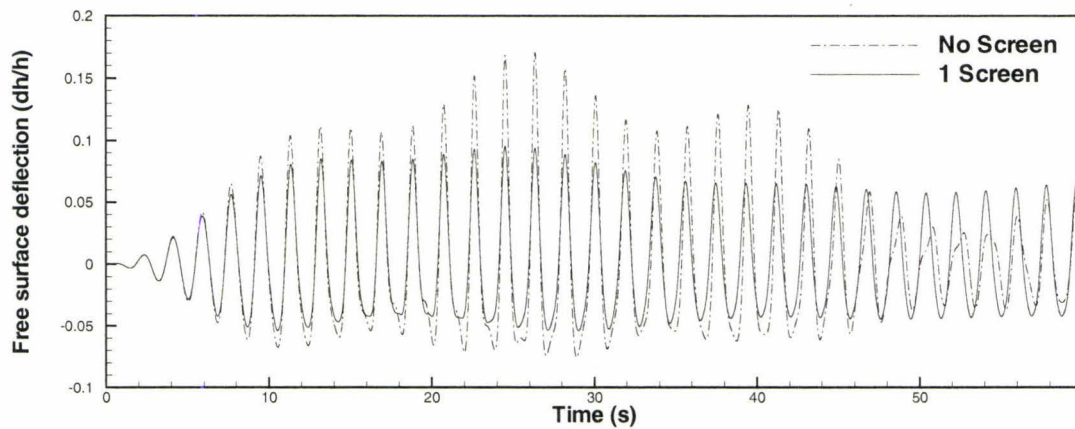
Results presented in this section are for a slat screen with a solidity ratio of 0.42, which corresponds to slat height of 5 mm and 7 mm spacing between slats. The screen is located at the middle of the tank, i.e. at  $x = 0.483$  m. The thickness of each slat and the

distance of the first slat from the bottom of tank, for all cases presented here, are 1 mm and 3 mm, respectively. The configuration of the slat screen is shown in figure 5-10.



**Figure 5-10: The screen configuration and its location**

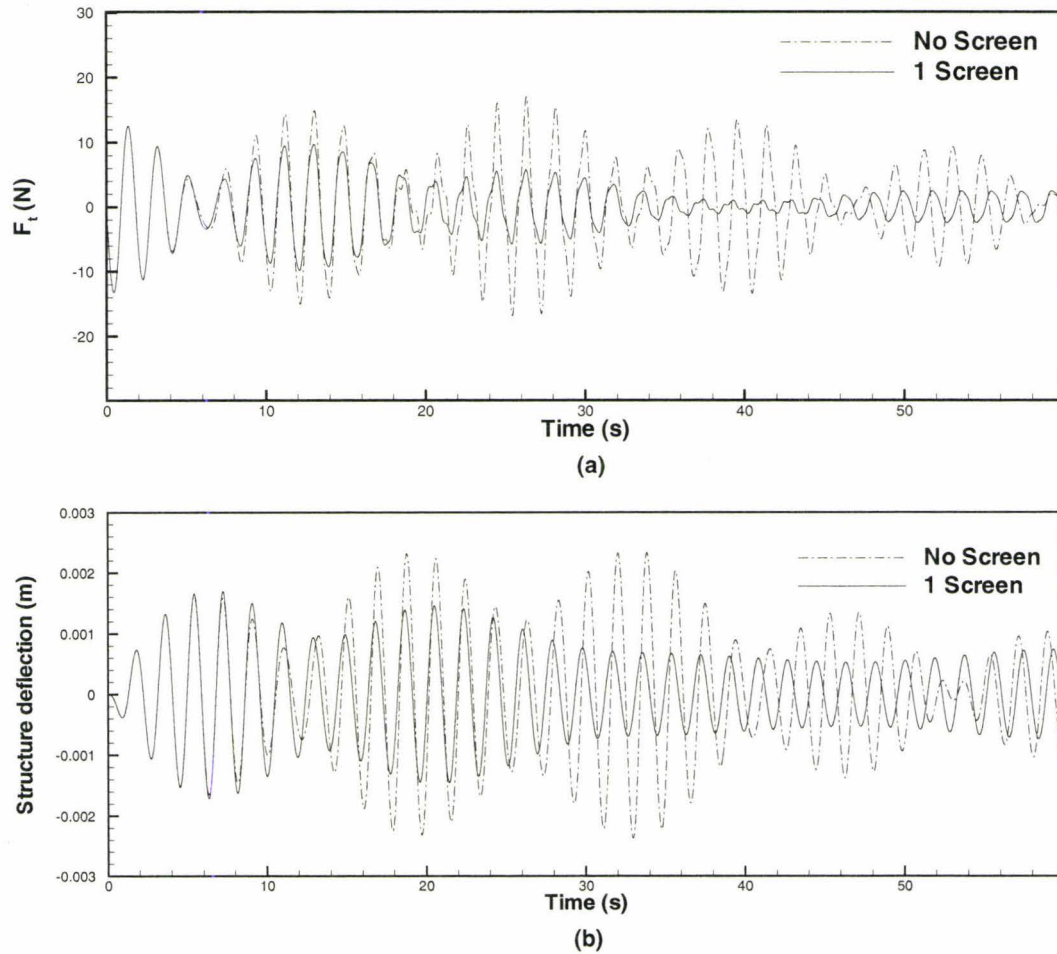
The TLD-structure system with the slat screen inside TLD is subjected to the same harmonic excitation function mentioned in section 5.2. Figure 5-11 shows the time history of the free surface deflection at  $x = 0.05 \times L$ , i.e.  $x=0.0483\text{m}$  for the cases of with and without screen in the TLD.



**Figure 5-11: Comparison of time history of the free surface deflection at  $x=0.05 \times L$  in the TLD with and without screen.**

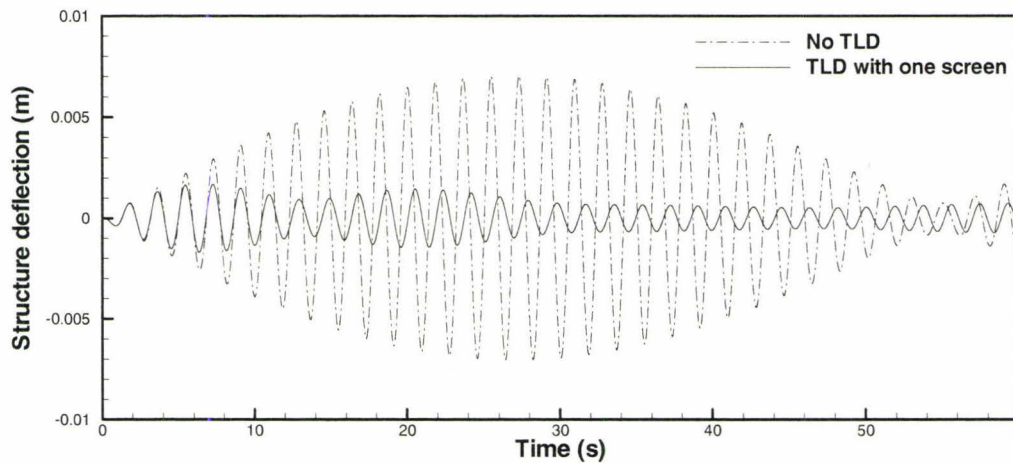
It was mentioned before that the beating phenomenon in a TLD having low damping is an undesirable phenomenon. Results shown in figure 5-11 indicate that using the screen has reduced the nonlinearity of the sloshing motion and reduced the beating phenomenon. The maximum deflection of the free surface after 30s is almost constant and uniform, which clearly indicates that using the screen made the sloshing motion more linear and more predictable.

Figure 5-12 shows the time history of the resultant force ( $F_t$ ) and the deflection of the structure coupled with a TLD with and without a slat screen. Results show that by using the slat screen, the resultant force, which is the sum of the excitation force and the sloshing force imposed on the structure, would be smaller and more uniform than the case with no screen. The reduction in the resultant force leads to decrease in the structure response, as shown in figure 5-12. Results indicate that after 30s, while the sloshing motion becomes uniform, the structure response become uniform as well.



**Figure 5-12: Comparison of the time history of (a) the resultant force and (b) the structure deflection for the cases of with and without screen.**

Figure 5-13 shows a comparison of the structure response for the cases of a structure with and without the TLD. Results show that using the TLD with one screen, not only made the behavior of TLD more linear and predictable, but also increased the damping effect of the TLD and so decreased the response of the structure.



**Figure 5-13: Comparison of the time history of the structure deflection with TLD outfitted by one screen at the middle and without a TLD**

Figure 5-14 shows the pattern of flow field inside the TLD at times at which the resultant force ( $F_r$ ) imposed to the structure, in the TLD with one screen, is less than the one with no screen. Flow patterns shown in figure 5-14 (a) are for the case of no screen. In this case, it is observed that two masses of fluid move opposite to each other. This phenomenon reduces the amount of generated sloshing force due to the sloshing motion and so it causes higher resultant force imposed to the structure.

Figure 5-14 (b) shows the flow pattern in the TLD with one screen at the middle. It is observed that in case of using the screen, the whole mass of the fluid moves in the same direction and contributes in generating the sloshing force and therefore causes smaller amount of resultant force.

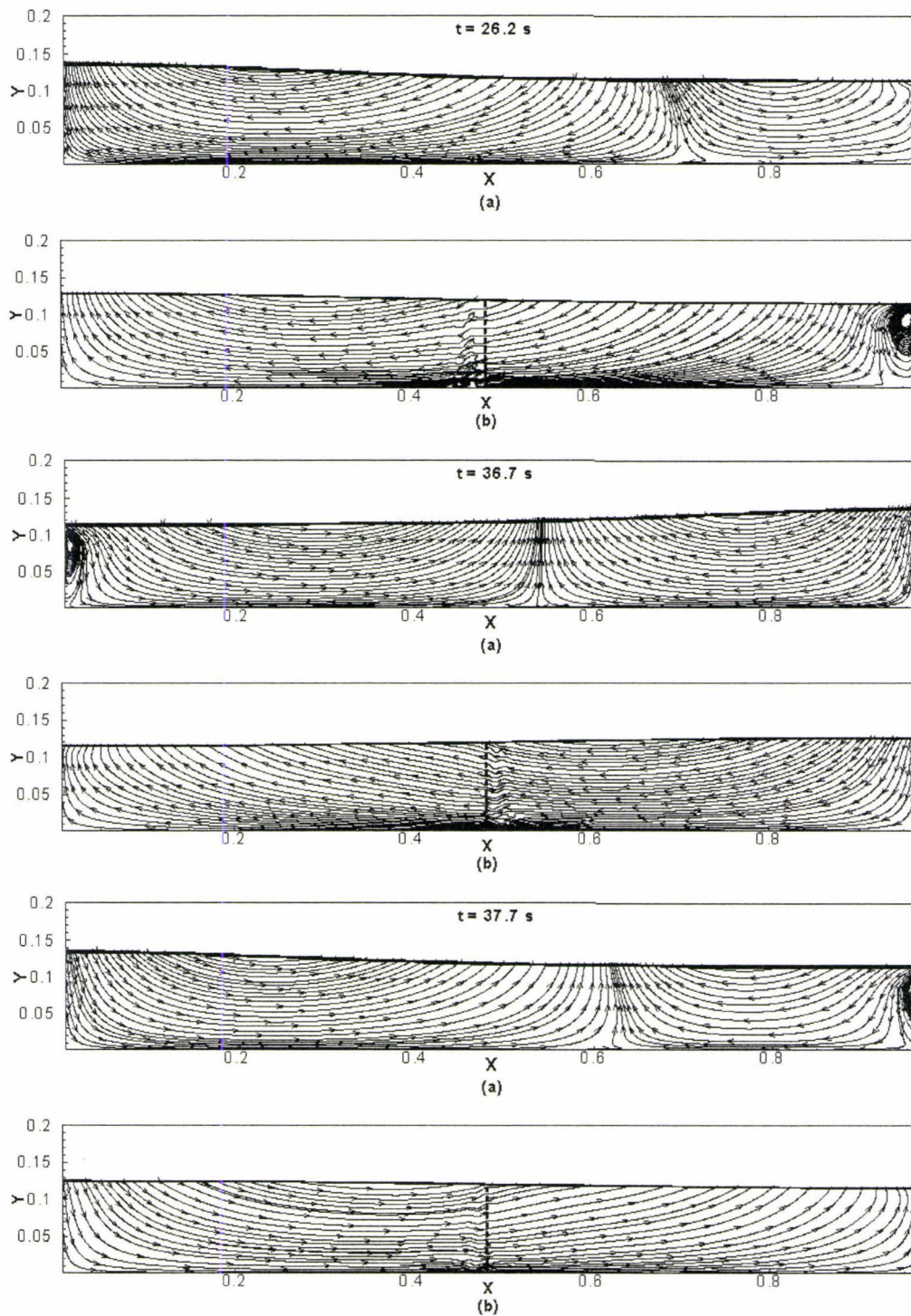


**Figure 5-14: The flow field inside the TLD for the cases of (a) without and (b) with a slat screen at  $t=26.2$  s,  $36.7$  s &  $37.7$  s. The TLD-Structure is subjected to harmonic excitation.**

### 5.3.2 TLD-Structure System Subjected to Random Excitation

The same TLD-Structure system has been subjected to the random excitation shown in figure 4-19. Figure 5-15 shows the deflection of the free surface, at  $x = 0.05 \times L$ , i.e.  $x=0.0483$  m, for both cases of TLD with and without a slat screen. Similar to the case of harmonic excitation, using the slat screen reduced the amplitude of maximum deflection of the free surface and the sloshing motion in TLD became more uniform and linear in the presence of the slat screen. The amplitude of the free surface deflection dropped from 75% of the initial depth of water in the TLD to less than 30% at  $t = 30$  second, as shown in figure 5-15.

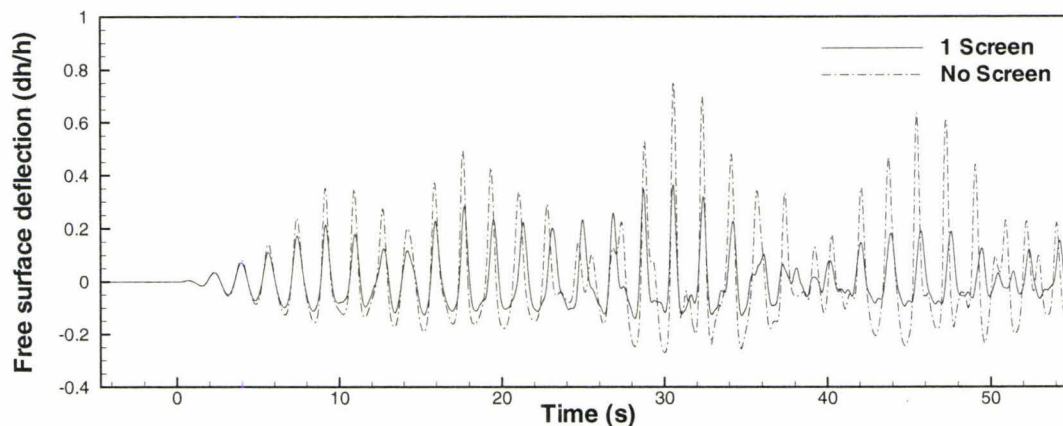
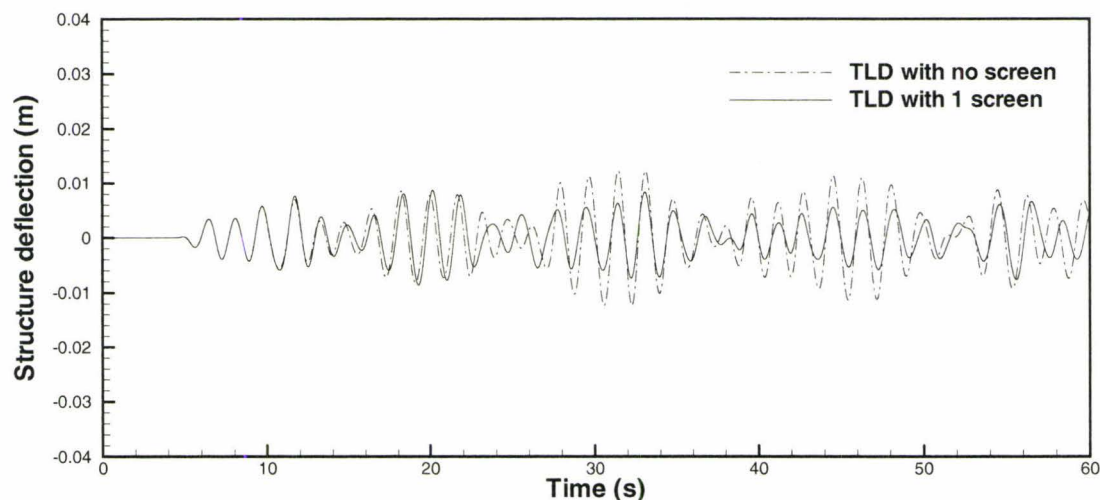


Figure 5-15: Comparison of time history of the free surface deflection in the TLD with and without screen.

Figure 5-16 shows the time history of the structure response for the cases of using a TLD with and without a slat screen. The slat screen reduced the structure response by 56% compared with no screen case. These results indicate that independent of the nature of the

external excitation, slat screens reduce the nonlinearity of the free surface motion and increase the damping effect of the TLD leading to smaller structure responses.



**Figure 5-16: The time history of structure response under random excitation for the case of using a TLD with and without screen**

In order to have a better understanding of how the screen decreases the non-uniformity of the sloshing motion and increases the damping effect of a TLD, the flow pattern inside the TLD at two selected times are compared in figure 5-17.

The snap shots in figure 5-17 are shown at times at which the deflection of the structure showed greater reduction because of the screen. Flow patterns shown in figure 5-17 (a) for the case of no screen show two masses of fluid moving opposite to each other and meeting in about the middle of the tank.

In this case, the two masses of fluid cancel out the effect of each other, which results in a low sloshing force generated by the sloshing motion. Such a phenomenon does not exist when the slat screen is used at the middle of the TLD, as shown in figure 5-

17 (b). In this case all fluid particles are moving in the same direction, which results into a larger sloshing force, and hence in higher effective damping.

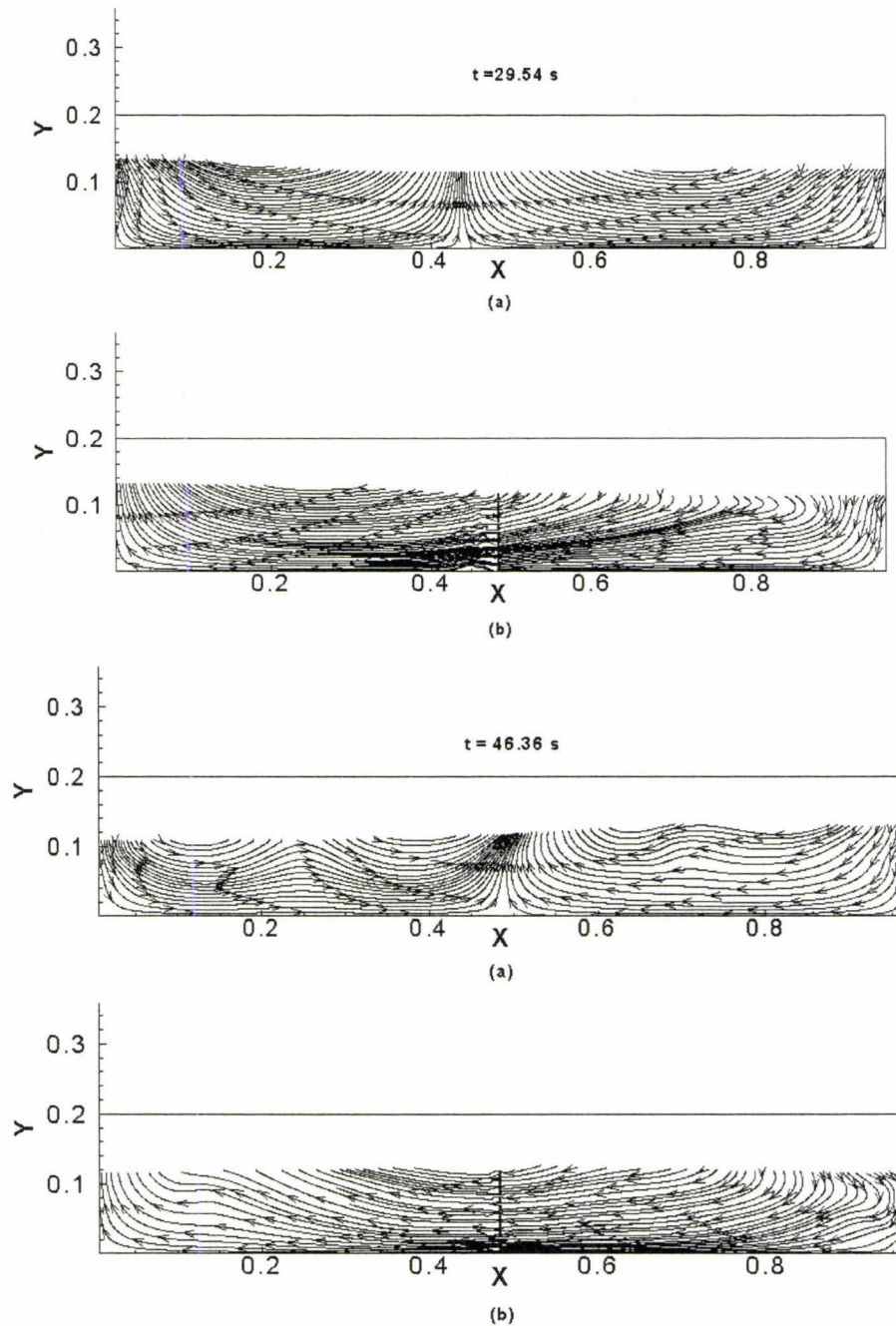


Figure 5-17: The flow field inside the TLD for the cases of (a) without and (b) with a slat screen at  $t=29.54$  s &  $46.36$  s. The TLD-Structure is subjected to random excitation.

The additional resistance introduced by the screen in the middle of the TLD increased the amount of energy dissipation and eliminated the recirculation zone in the middle of the tank and so the entire fluid mass moved in one direction. The elimination of the recirculation zone in the middle of the cavity reduced the nonlinearity of the fluid motion inside the TLD and unpredictability.

Results presented in this section clearly indicate the significant effect a slat screen has on the flow field and hence on the TLD performance. Results presented here are only use one screen placed at the middle of the TLD. The effect of using more than one screen is presented in the next section.

## **5.4 Effect of Number of Screens on TLD Performance and Structure Response**

In order to investigate the effect of number of screens, the TLD-structure system discussed in section 5.3 has been subjected to both harmonic and random excitations using two screens placed inside the TLD. These two screens were located at  $x = 0.386$  m and  $0.58$  m, which correspond to 40% and 60% of the tank length, as shown in figure 5-18. The two slat screens have the same dimensions shown in figure 5-10, that is, the solidity ratio of each screen is 0.42 with the slat height of 5 mm, spacing of 7 mm and thickness of 1 mm. The distance of the first slat from the bottom of the tank is 3mm.

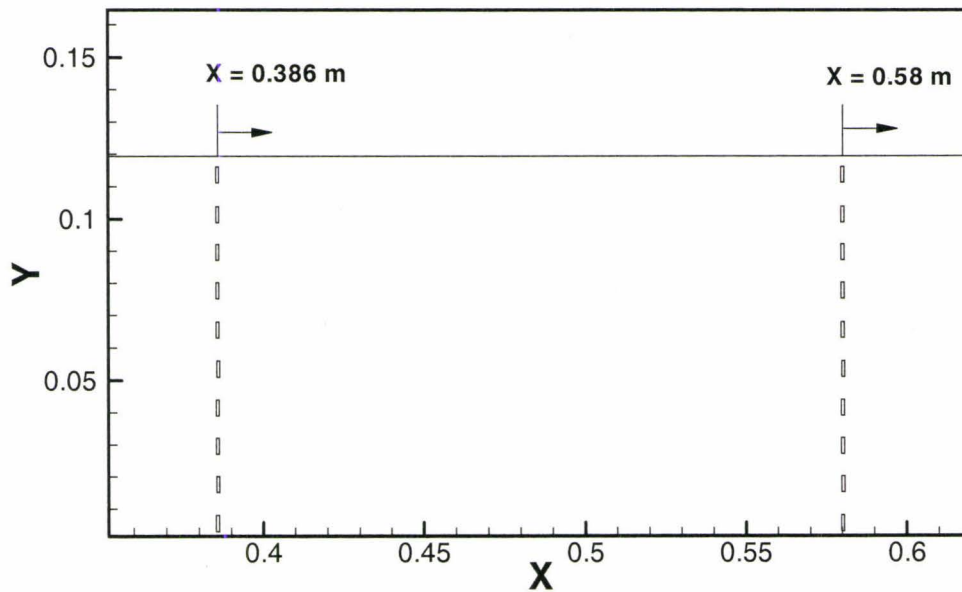
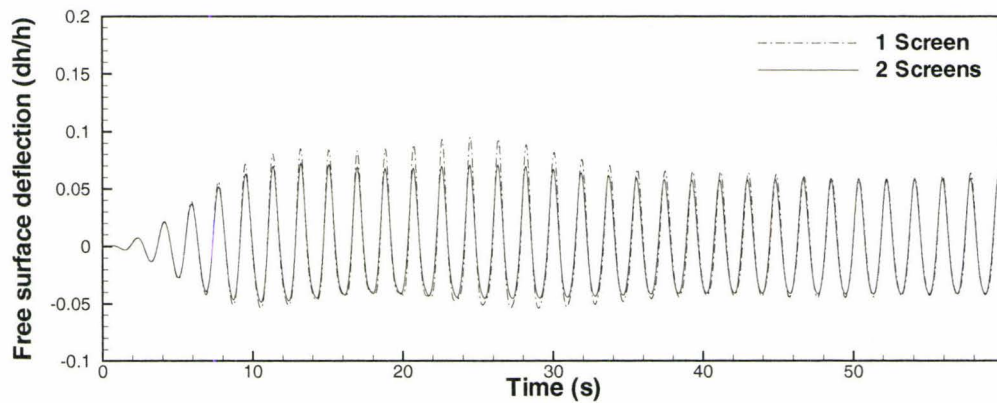


Figure 5-18: Locations of two screens placed in the TLD

### 5.4.1 Case of Harmonic External Excitation

The TLD-structure system subjected to the same harmonic excitation discussed in section 5.3. The amplitude is 10 mm and the excitation frequency is 0.54 Hz. Figure 5-19 shows the deflection of the free surface for the cases of TLD with one screen and with two screens.

As was expected, adding another screen has made the sloshing motion more uniform and reduced the amplitude of the free surface deflection, especially at early time cycles. The maximum deflection of the free surface becomes almost constant at  $t=10$  sec and remain constant in the whole period of TLD operation. This uniformity is reached after about 35 s in the case of one screen.



**Figure 5-19: Comparison of time history of the free surface deflection at  $x=0.0483\text{m}$  in a TLD with one and two screens.**

Figure 5-20 shows the deflection of the structure for the cases of one and two screens. Structure deflection in both cases is almost the same during the first 10s. In the time interval between 10s and 30s, TLD with two screens has more effective damping on the structure and so leads to less structure deflection. This means that the resultant force applied to the structure which is the sum of the sloshing and external excitation forces is less for the case of TLD with two screens in this time interval.

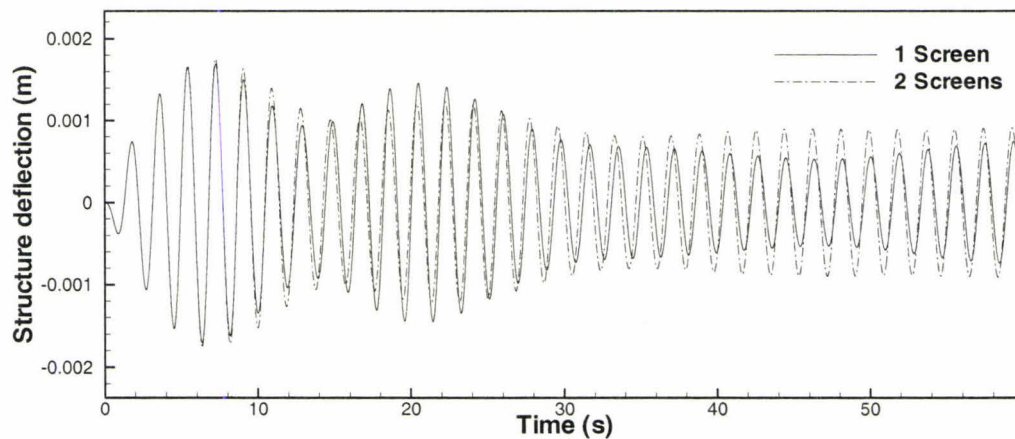


**Figure 5-20: Comparison of time history of structure deflection in the cases of TLD with one and two screens.**

The time history of the sloshing force imposed on the structure for both cases of TLD with one and two screens against the external excitation is shown in figure 5-21.

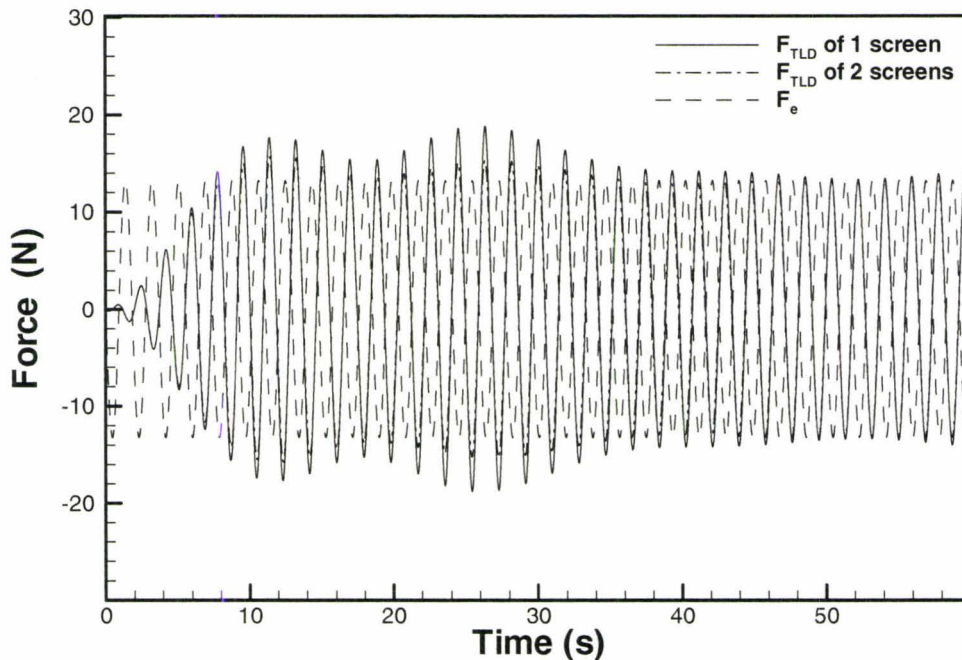


Figure 5-21: Comparison of time history of sloshing force for the cases of TLD with one and two screens.

It is observed that generated sloshing force at the first 10 sec for both cases is almost the same. After that, the sloshing force in case of TLD with one screen becomes higher than the case of two screens especially in time interval between 10 sec and 30 sec. During this time interval, although the sloshing force of TLD with one screen is higher, the resultant force imposed to the structure for the TLD with two screens is smaller. It is because the magnitude of the sloshing force of the TLD with two screens is close to the magnitude of excitation force while in case of the TLD with one screen this magnitude is higher than

the external excitation force. Therefore, the resultant force, which is the sum of these two forces would be smaller in the case of a TLD with two screens, as shown in figure 5-22. Figure 5-22 shows the time history of the resultant force for both cases of a TLD with one and two screens. The resultant force for the case of TLD with two screens in this time interval is smaller than the case of a TLD with one screen and this is the reason that the structure deflection in this time interval for the case of TLD with two screens is smaller. After approximately 30s, the magnitude of sloshing force of TLD with one screen which becomes closer to the external excitation force and the resultant force of the case of TLD with one screen becomes smaller than the case of TLD with two screens and therefore the corresponded deflection of structure would be smaller. After about  $t= 45s$ , the sloshing force in the case of one screen starts to become larger and so the corresponding resultant force becomes larger as shown in figure 5-22.

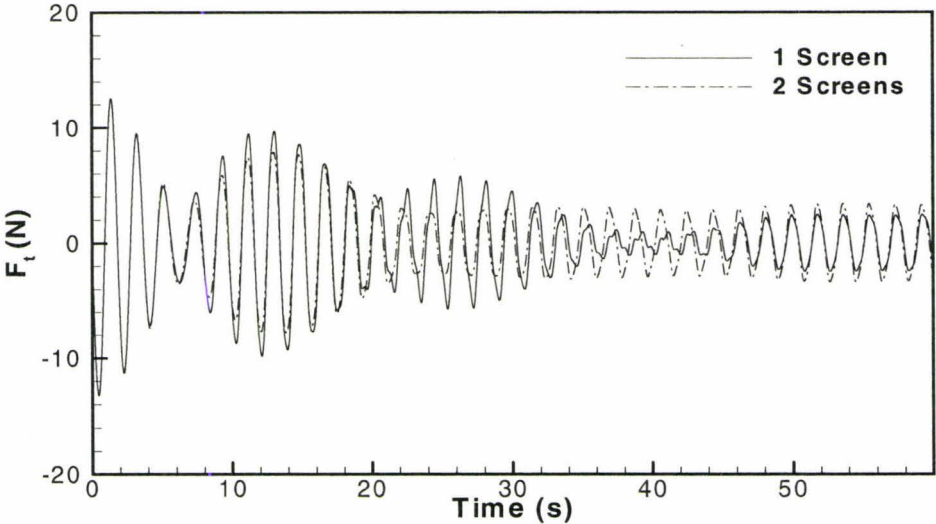
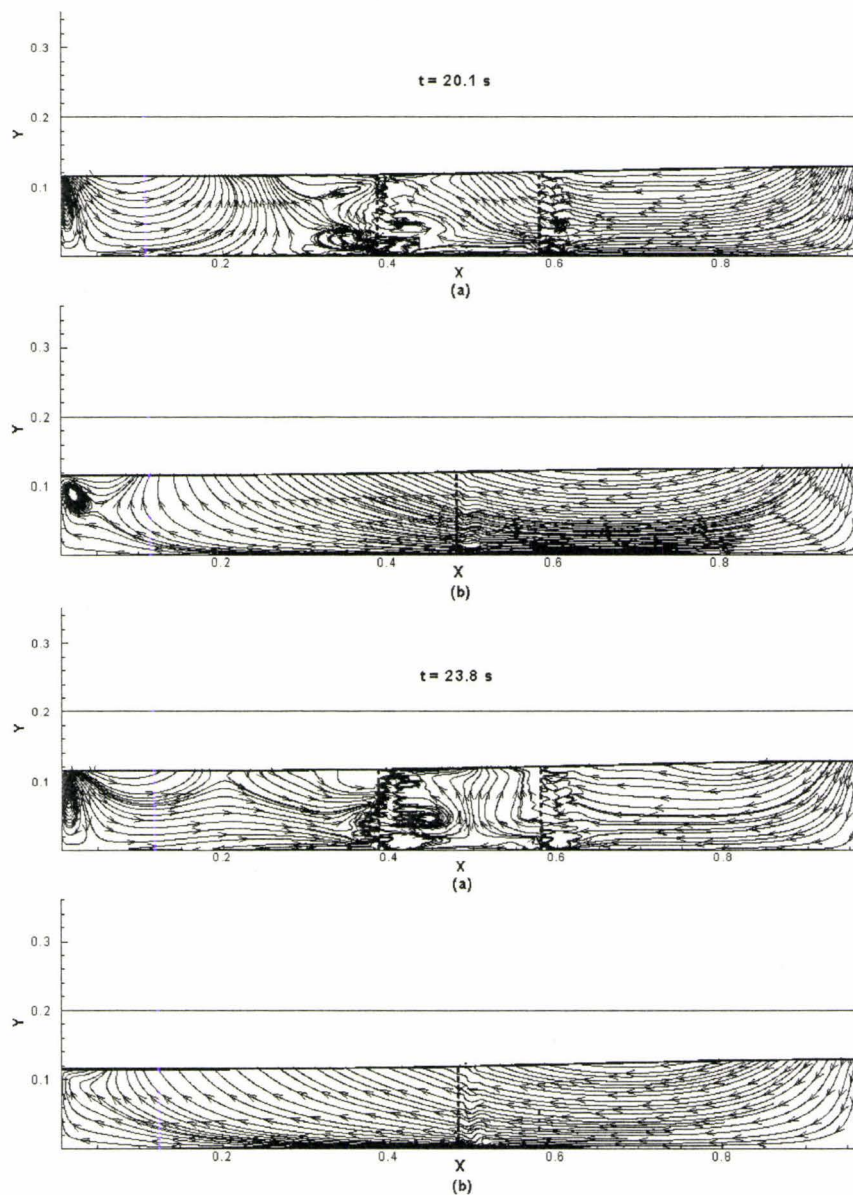


Figure 5-22: Comparison of time history of resultant force for the cases of TLD with one and two screens.

Figure 5-23 shows the pattern of the flow field in the TLD for the cases of one and two screens. The created recirculation zones and masses of fluid moving opposite to each other in case of two screens results in lower sloshing force generated by the sloshing motion.



**Figure 5-23: The flow field inside the TLD for the cases of with (a) two screen and (b) one screen at  $t=20.1$  s & 23.8 s**

## 5.4.2 Case of Random External Excitation

The same TLD-structure system has been subjected to the random excitation force shown in figure 4-19. The time history of the free surface deflection at  $x=0.0483\text{m}$  has been compared for both cases of TLD with one and two screens in figure 5-24. Again, it was observed that adding one more screen, has made the sloshing motion of water inside the TLD more uniform and reduced the amplitude of maximum deflection of free surface.

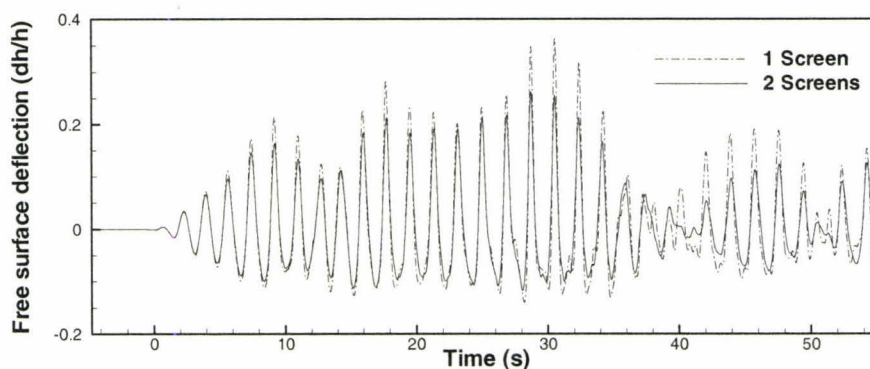


Figure 5-24: Comparison of time history of the free surface deflection at  $x=0.0483\text{m}$  in the case of TLD with one and two screens.

Figure 5-25 shows the sloshing force for the cases of TLD with one and two screens.

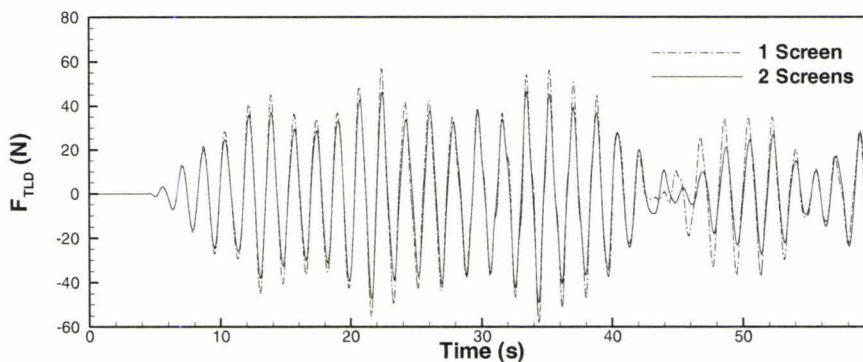
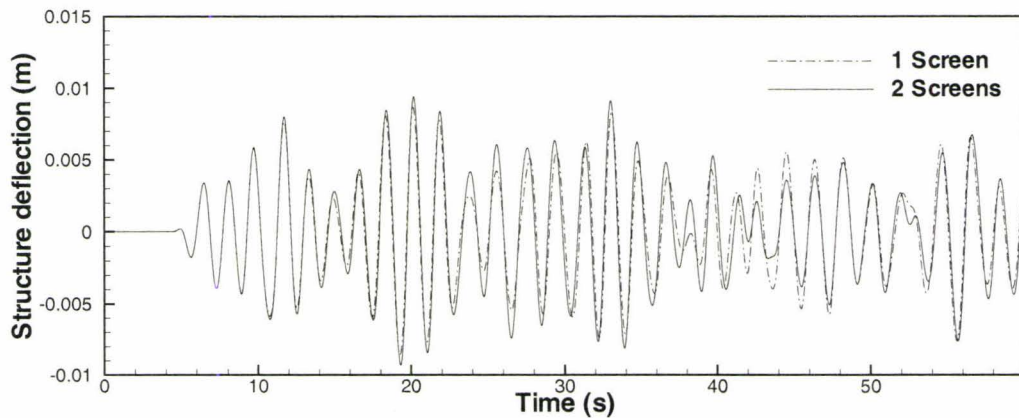


Figure 5-25: Comparison of time history of the sloshing force in the case of TLD with one and two screens.

It was observed that a TLD with one screen generated a higher sloshing force during the TLD operation which resulted in smaller structure response for the case of one screen except for the time interval between about 42 sec and 46 sec, as shown in figure 5-26. During this time interval, the generated sloshing force in case of a TLD with one screen became smaller for the case of two screens and caused an increase in the structure response compared to the case of TLD with two screens.



**Figure 5-26: Comparison of time history of the structure deflection in the case of TLD with one and two screens.**

Figure 5-27 shows the pattern of the flow field in a TLD for the cases of one and two screens at different times. Similar to harmonic excitation, the created recirculation zones and masses of fluid moving opposite to each other in case of two screens results in lower sloshing force generated by the sloshing motion except for the time interval between 42 sec and 46 sec which this phenomenon was observed for the case of one screen. Physically, by growing the sloshing motion during the TLD operation, the rate of change of momentum of fluid in the TLD with one screen is higher which leads to a higher sloshing force.

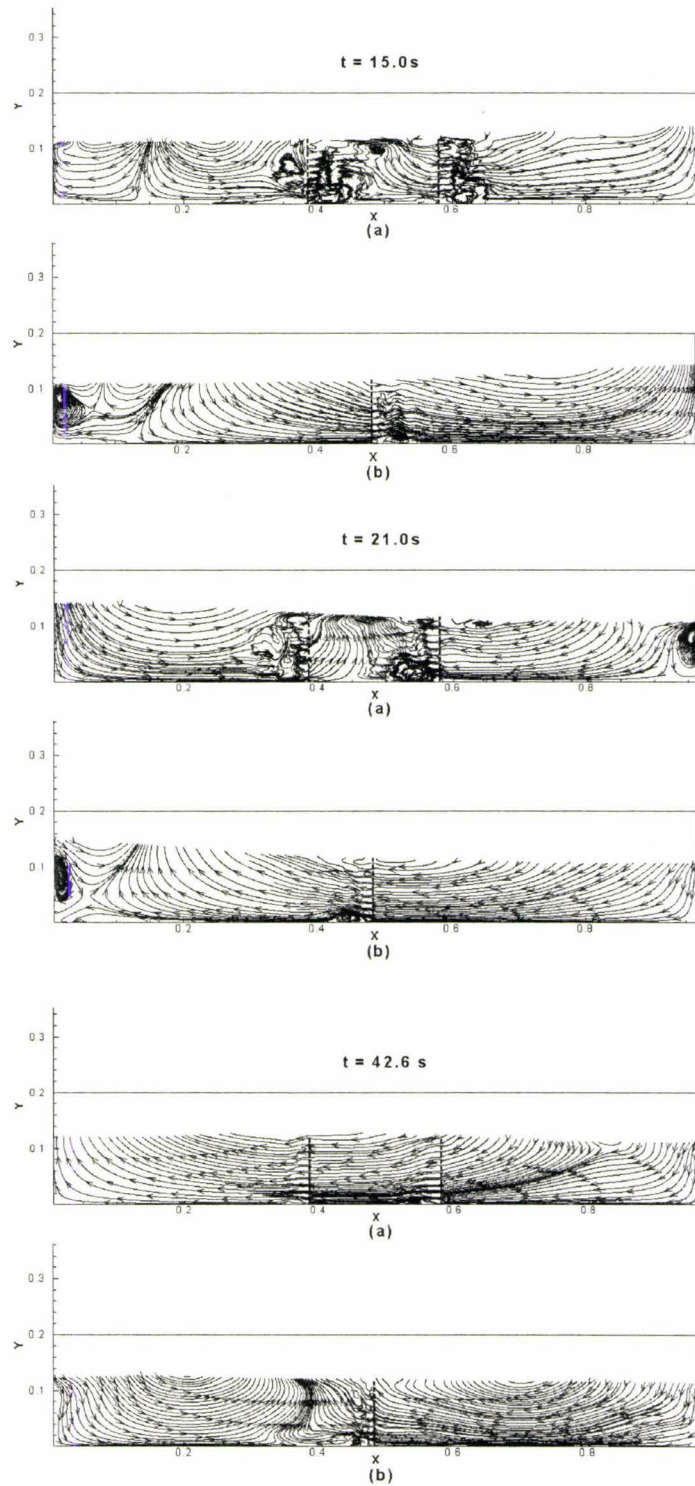


Figure 5-27: The flow field inside the TLD for the cases of with (a) two screen and (b) one screen at  $t=15$  s & 21 s & 42.6 s

The study of numerical results in this section helped to reach the major conclusion that the introduction of screens into a TLD increases its inherent damping, thus decreases structure response and provides more uniform and predictable sloshing motion inside the TLD. It was found that increasing the number of screens could reduce the amplitude of free surface deflection and makes the sloshing motion more linear.

## 5.5 Effect of Screen Pattern

### 5.5.1 Characteristic Dimension of Slat Screen

To the best of the author's knowledge, no numerical work has been published on the effect of screen pattern on the performance of a TLD and the response of the structure. This is because no past research had fully resolved the details of the flow through slat screens. In all previous work, screens have been dealt with as a hydraulic resistance without taking the effect of their pattern into consideration. Only the solidity ratio was considered. The solidity ratio of the screen is insufficient to characterize the slat screens based on their pattern. Different slat screens could have the same solidity ratio with different patterns. In order to address the effect of screen pattern, in this study a new parameter has been introduced termed as the "Slat Ratio" (SR) defined based on the total solid height of the screen. The solid height of screen ( $S_s$ ) is equal to the slat height multiplied by the number of slats, as shown in figure 5-28.

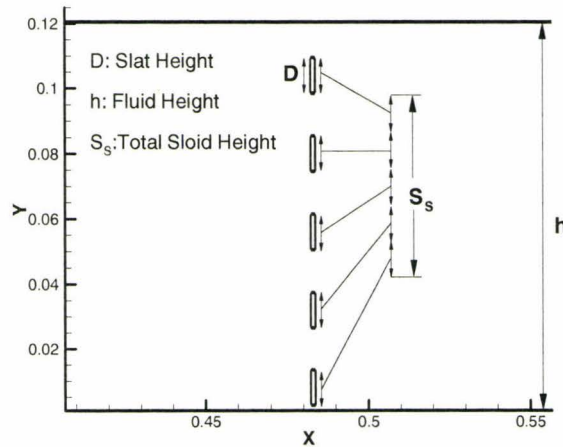


Figure 5-28: Characteristic dimensions of the slat screen

The total solid height of the screen ( $S_s$ ) can also be defined as the product of the solidity ratio multiplied the fluid height. The slat ratio (SR) is then defined as the ratio of the slat height ( $D$ ) to the total solid height of the screen ( $S_s$ ), i.e.,

$$SR = \frac{D}{S_s} = \frac{D}{S \cdot h} \quad (5-3)$$

## 5.5.2 Effect of Screen Pattern on Flow inside the TLD and on the Structure Response

### 5.5.2.1 Harmonic External Excitation

To study the effect of the screen pattern on the response of the structure, two slat screens with solidity ratios of 0.42 and slat ratios of 0.2 and 0.5 were considered. The two slat ratios correspond to slat heights of 10 mm and 25 mm, respectively. The corresponding slat spacing is 13mm and 34mm, respectively. The thickness of each slat

and the distance of the first slat from the bottom of tank are 1 mm and 3mm, respectively. The TLD and the structure properties are the same as in tables 4-3 and 4-4. For each case, screens were located at 40% and 60% of tank length, from left. According to this configuration, the screens were completely submerged under water. Figure 5-29 shows the location and configuration of the two screens used in this case study.

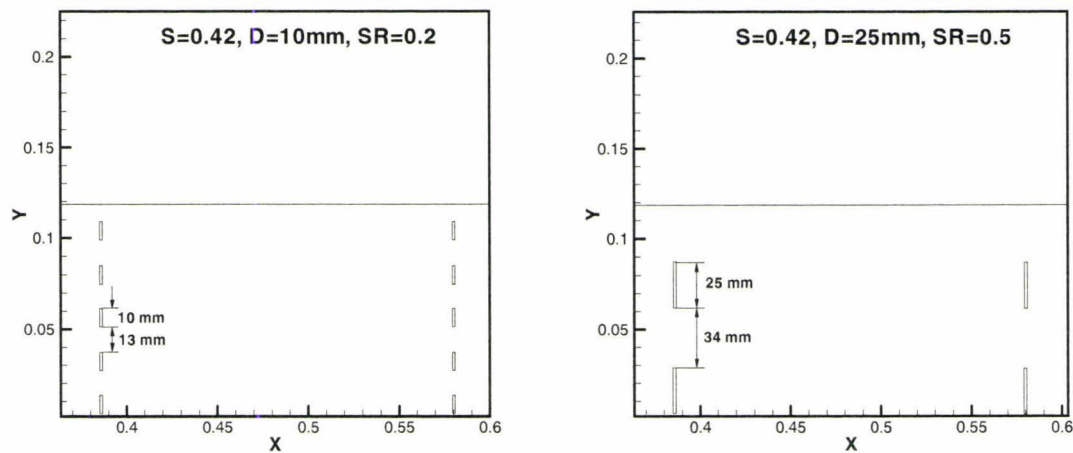


**Figure 5-29: Location of the two slat screens having the same solidity ratio and different slat ratio**

The TLD-structure system subjected to a harmonic excitation function with an amplitude of 10 mm and a frequency of 0.54 Hz. Figure 5-30 illustrates the flow pattern of water inside the TLD for both cases of SR=0.2 and 0.5.

Flow patterns show that the large scale vortices are produced for the higher slat ratio. Figure 5-30 (a) and (b) show the flow patterns at  $t=15.0$  s. It was observed that for the slat ratio of 0.5, some vortices were created before the screen in the direction of flow. These vortices changed direction of flow and didn't allow fluid particles to have a smooth horizontal path. Fluid particles rather have a wavy path at the middle of the tank between the two screens compared to the case of SR=0.2 in which case fluid particles are moving

through an almost perfect horizontal path. Figure 5-30 (c) and (d) show the same behavior at  $t = 24.7$ s.

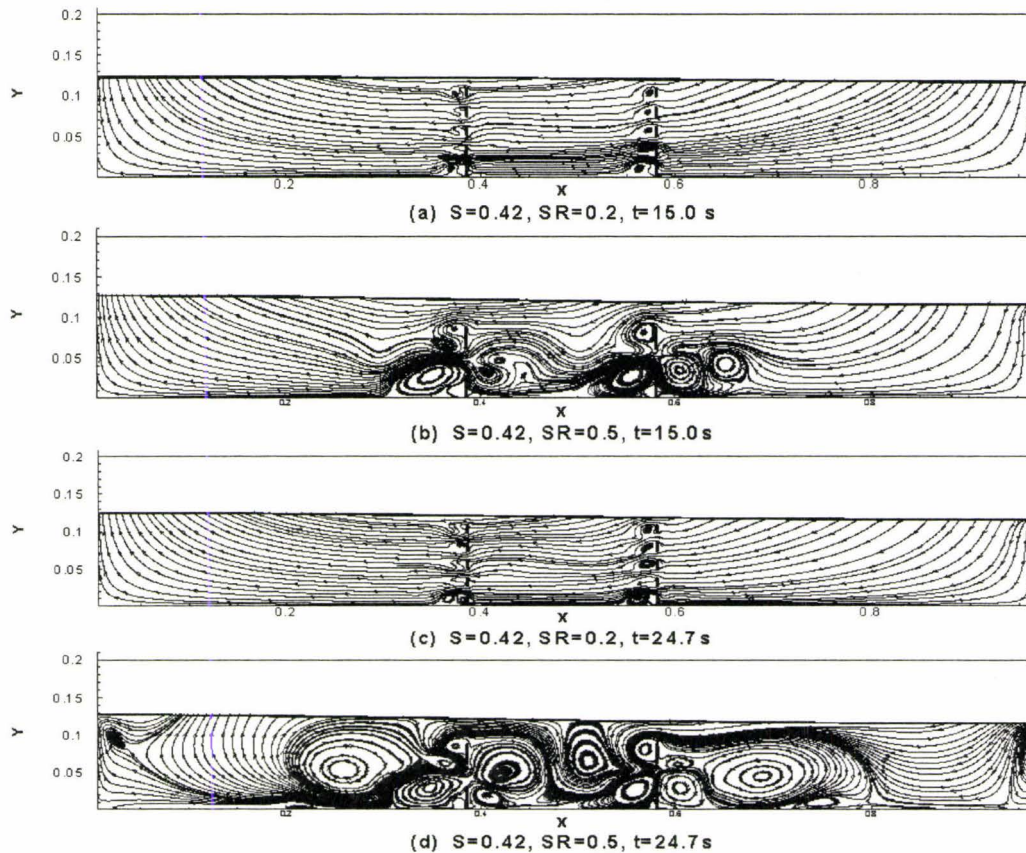


**Figure 5-30: Effect of SR on flow pattern inside a TLD subjected to a harmonic excitation.**

The main effect of these large scale vortices is to reduce the overall momentum of fluid particles in the  $x$ - direction and so to reduce the amplitude of maximum deflection of the free surface and the sloshing force created inside the TLD.

The effect of SR on the free surface deformation for these two cases of  $SR=0.2$  and  $0.5$  are shown in figure 5-31.  $SR=0.5$  resulted in lower maximum free surface deformation by about 22%.

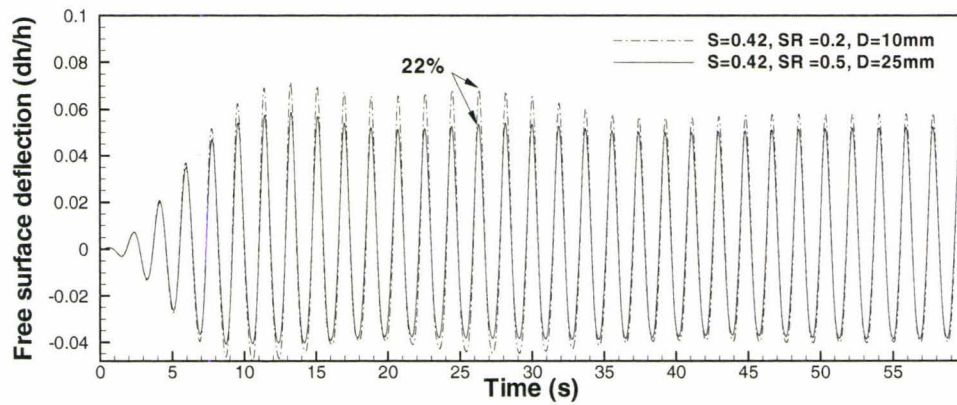


Figure 5-31: Effect of SR on deformation of free surface at  $x=0.0483\text{m}$ .

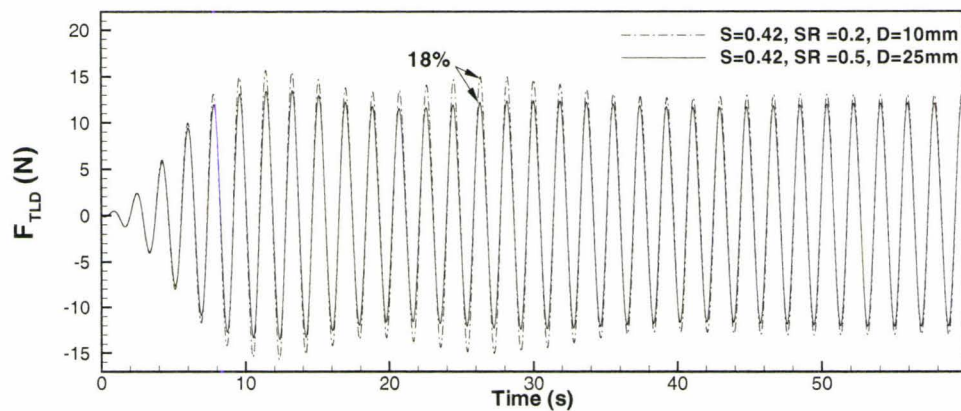


Figure 5-32: Effect of SR on the sloshing force inside the TLD.

The effect of SR on the sloshing force produced inside the TLD is shown in figure 5.32. Increasing SR from 0.2 to 0.5 resulted in decreasing the sloshing force by up to 18%. Figure 5-33 shows the effect of SR on structure response. Results show that the larger sloshing force generated by a TLD outfitted with screens with a slat ratio of 0.2 lead to a structure response reduced by 33%.

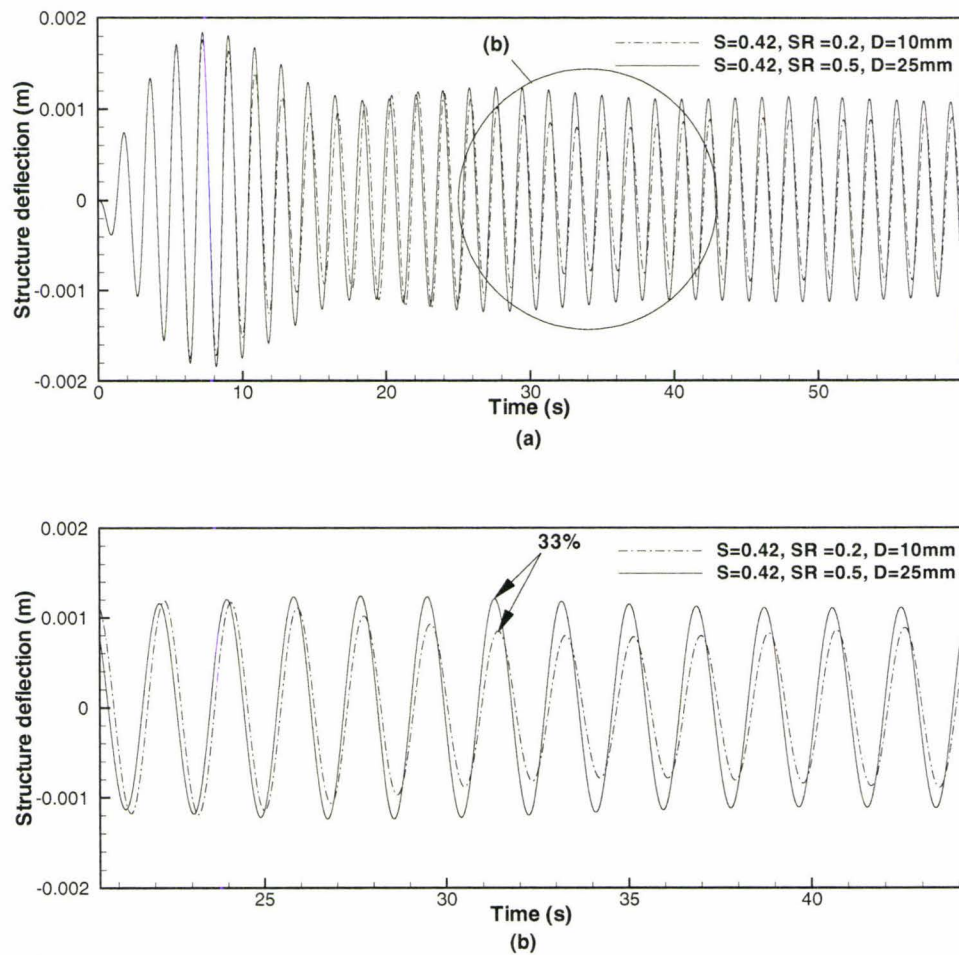


Figure 5-33: Effect of SR on structure response.

Figure 5-34 shows the effect of SR on the acceleration of the structure. Up to a 33% reduction in structure acceleration was achievable just by changing the slat ratio from 0.5 to 0.2 (the slat height from 25mm to 10mm).

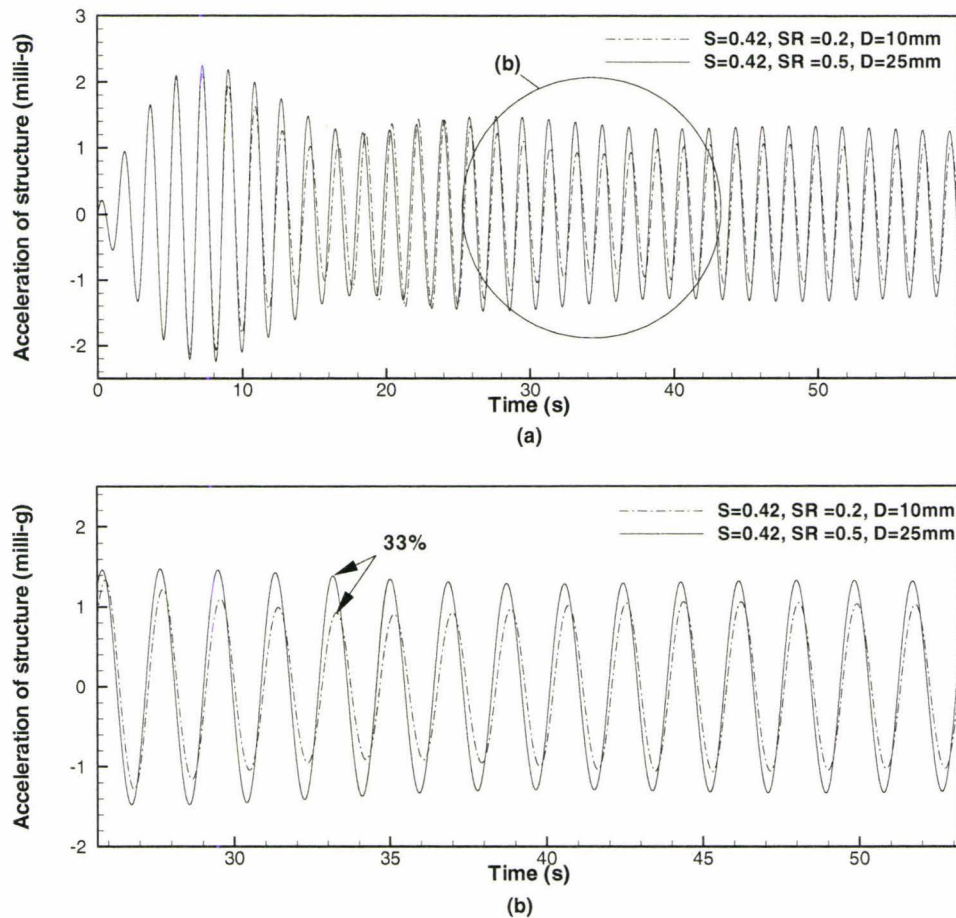


Figure 5-34: Effect of SR on structure acceleration.

### 5.5.2.2 Random External Excitation

The same analysis has been carried out on the same structure subjected to the random excitation shown in figure 4-19. The effect of SR on the free surface deformation at  $x=0.0483\text{m}$ , in the TLD outfitted with two screens shown in figure 5-29 is presented in figure 5-35. Results indicate that increasing the slat ratio reduced the maximum amplitude of the free surface deformation by up to 18%. This reduction in the case of the higher slat ratio ( $SR=0.50$ ) is because of the formation of larger recirculation zones for

this case. Figure 5-36 show the flow patterns for these two slat screens at two different times.

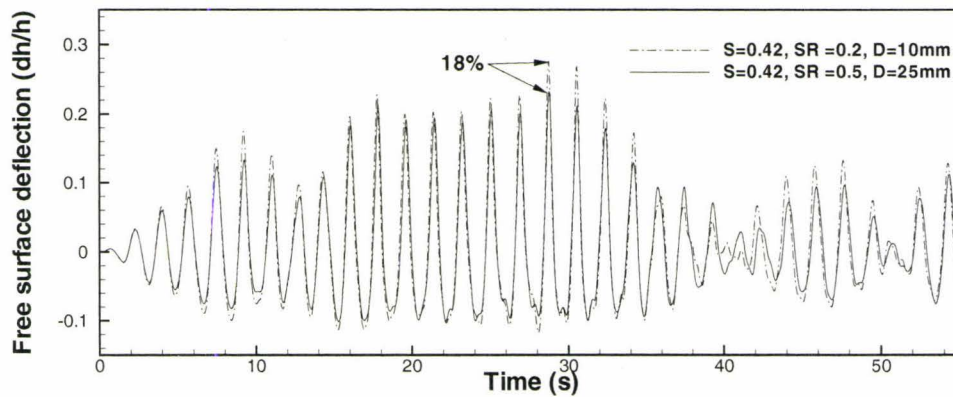


Figure 5-35: Effect of SR on free surface deformation at  $x=0.0483m$ .

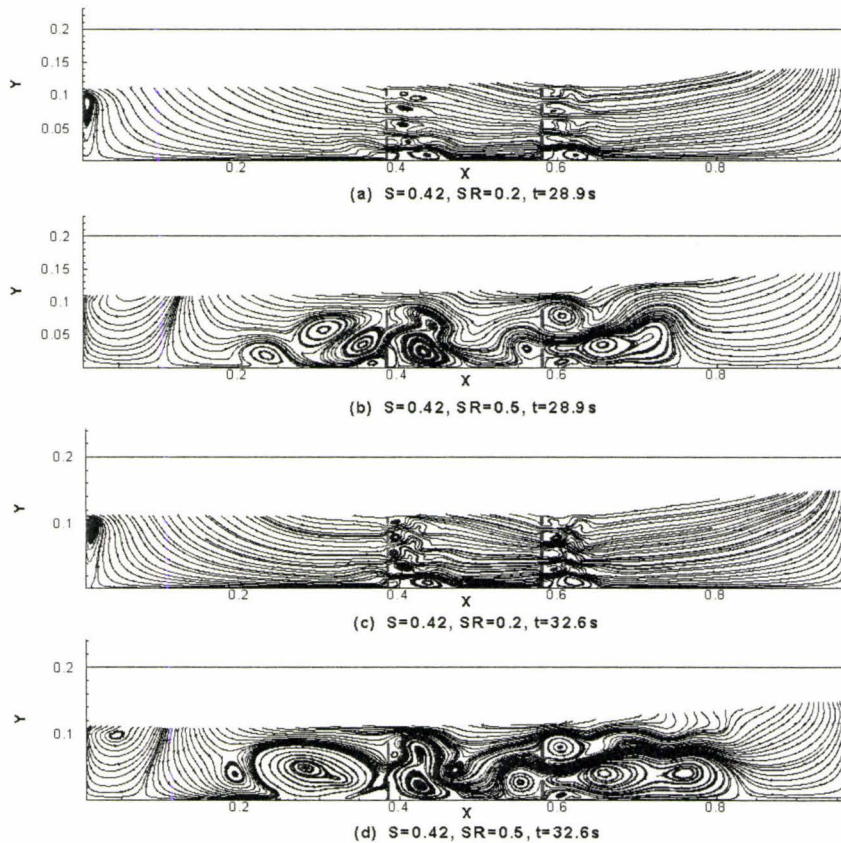
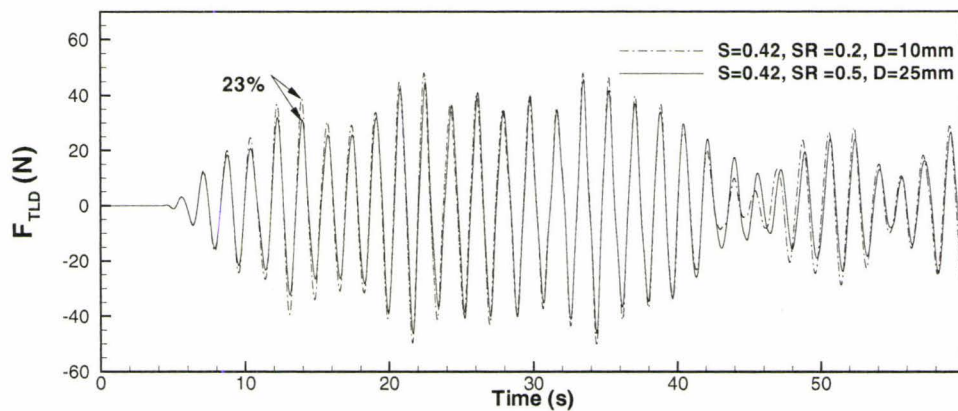


Figure 5-36: Comparison of flow pattern around the slat screens.

These large vortices caused a drop in the overall momentum of the fluid and so reduced the amplitude of the maximum deformation of the free surface, by up to 18%.

The other effect of these recirculation zones is a drop in the sloshing force generated by the fluid. Figure 5-37 shows the time history of the sloshing force inside the TLD for the two cases. Results show that the sloshing force in the case of  $SR=0.2$  is larger than  $SR=0.5$  by up to 23% which lead to smaller deflection of structure. The response of the structure for each case is shown in figure 5-38.



**Figure 5-37: Effect of SR on sloshing force inside the TLD.**

Results shown in figures 5.37 and 5.38 indicate that the slat height of 10 mm ( $SR=0.2$ ) resulted in an increase in the inherent damping of the TLD and reduced the response of the structure by about 33%. These results clearly indicate the significant effect of screen pattern on the amount of effective damping of the TLD.

When a tall flexible structure is subjected to lateral deflections under the action of fluctuating earthquake and/or wind loads, the resulting oscillatory movements could

induce a wide range of responses in the building's occupants, ranging from mild discomfort to acute nausea.

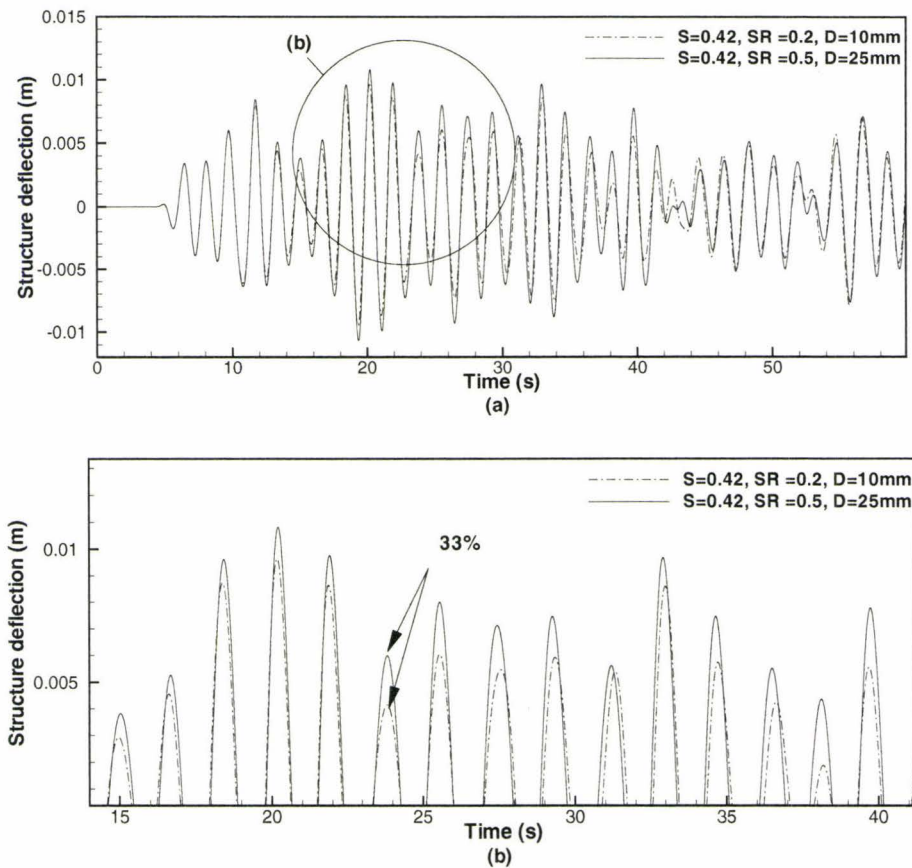
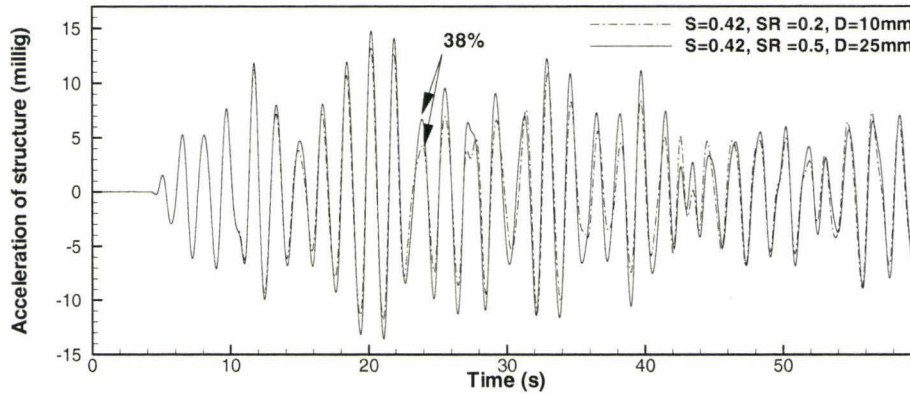


Figure 5-38: Effect of SR on structure response.

Motions that have psychological or physiological effects on the occupants may thus result in an otherwise acceptable structure becoming an undesirable or even an inhabitable building. According to the National Building Code of Canada (NBCC) the averaged acceleration of the building should be kept less than 15 milli-g. Figure 5-39 shows the acceleration of the structure coupled with a TLD equipped with two slat

screens. Results shown in figure 5-39 indicate that the structure acceleration with  $SR=0.2$  is lower than  $SR=0.5$  by up to 38%.



**Figure 5-39: Effect of SR on the acceleration of the structure.**

Regardless of the type of the external excitation, the numerical results presented in this section clearly indicate the significant effect of screen pattern on the performance of the TLD and hence on the structure response. These results are in agreement with experimental observations and data reported by Hamelin in [18] on the effect of screen pattern.

### 5.5.3 Effect of Screen Pattern on Pressure Drop through Screen

Previous numerical investigations did not resolve details of flow through screens. Rather, screens were dealt with as a hydraulic resistance and so an expression for the pressure drop using some simplifying assumptions was added to the momentum equation. Baines and Peterson (BP) [2] proposed equation (5-4) to calculate the loss coefficient of a screen using the following assumptions:

- Flow through the screen is potential.
- Flow is streamlined (i.e. with no recirculation).
- Flow velocity before and after the screen is equal to the mean free stream velocity.

$$C_{l_b} = \left( \frac{1}{C_c(1-S)} - 1 \right)^2 \quad (5-4)$$

where  $C_c$  and  $S$  are the contraction coefficient and the solidity ratio, respectively. Tait [57] proposed the following equation for the contraction coefficient for a slat screen:

$$C_c = 0.405e^{-\pi S} + 0.59 \quad (5-5)$$

The pressure drop through the screen is then calculated by using the BP loss coefficient as follows:

$$\Delta p = \frac{1}{2} \rho U_s^2 C_{l_b} \quad (5-6)$$

where  $U_s$  is the averaged velocity at the screen location. This velocity is calculated from averaging the velocity before ( $U_1$ ) and after ( $U_2$ ) the screen as follows:

$$U_s = \frac{U_1 + U_2}{2} \quad (5-7)$$

It is important to note that BP's loss coefficient equation includes the effect of the solidity ratio ( $S$ ), however, it does not account for the effect of the screen pattern (SR). Therefore, two screens with the same solidity ratio but with different patterns would result in the same pressure drop which is not necessarily true. A series of numerical simulations considering harmonic external excitation have been carried out in order to investigate the

effect of screen pattern on the value of the pressure drop through the screen. Initially, an excitation amplitude of 42 mm and a frequency of 0.54 Hz were employed. The selected solidity ratios in this study are:  $S = 0.4, 0.5$  and  $0.6$ . This range was selected because it covers the practical range in real TLD applications.

Table 5-1: Different screen patterns at  $S=0.4$ 

SR	D	$D_o$	$D_b$	$D_t$	$N_S$
0.0417	2	3	2	1	24
0.0625	3	4	6	6	16
0.0833	4	5	9	8	12
0.125	6	8	8	8	8
0.167	8	10	11	11	6
0.25	12	14	15	15	4
0.333	16	18	18	18	3
0.5	24	24	24	24	2

Table 5-2: Different screen patterns at  $S=0.5$ 

SR	D	$D_o$	$D_b$	$D_t$	$N_S$
0.033	2	2	0	0	30
0.05	3	3	2	1	20
0.0667	4	4	2	2	15
0.0833	5	5	3	2	12
0.1	6	6	3	3	10
0.167	10	10	5	5	6
0.2	12	12	6	6	5
0.25	15	15	8	7	4
0.333	20	20	10	10	3

Table 5-3: Different screen patterns at  $S=0.6$ 

SR	D	$D_o$	$D_b$	$D_t$	$N_S$
0.0417	3	2	1	1	24
0.0555	4	2	7	7	18
0.0833	6	3	8	7	12
0.1111	8	4	8	8	9
0.125	9	5	7	6	8
0.167	12	6	9	9	6
0.25	18	9	11	10	4
0.333	24	12	12	12	3
0.5	36	16	17	16	2

A wide range of slat heights were considered for each solidity ratio. The TLD properties were kept the same as those listed in table 4-4. Details of all cases considered to investigate the effect of screen pattern on pressure drop at each solidity ratio are listed in tables 5-1 to 5-3. The distance between the slats ( $D_o$ ) and also distance of the first and last slat from tank bottom ( $D_b$ ) and free surface ( $D_t$ ) at rest have been arranged in such a way that the screen is submerged in water.

The main feature that made BP's equation so popular and used in almost all previous studies is its simplicity. In the present study, two objectives were set: to check the applicability of BP's equation, and to propose some modifications to introduce the effect of screen pattern (SR) to the BP's equation.

Using the developed algorithm, the pressure drop and the velocity at the screen were calculated for different solidity ratios and slat heights. The results shown in figure 5-40 indicate that the maximum pressure drop is directly proportional to the solidity ratio.

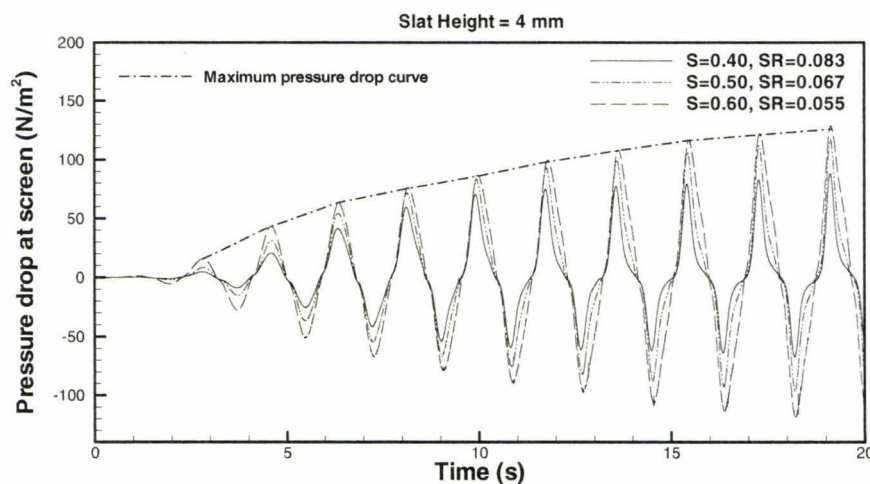


Figure 5-40: Time history of pressure drop for different solidity ratios and  $D=4\text{mm}$ .

Variation of maximum velocity at the screen with the solidity ratio is shown in figure 5-41. These results indicate that the maximum velocity at the screen decreases as the solidity ratio increases.

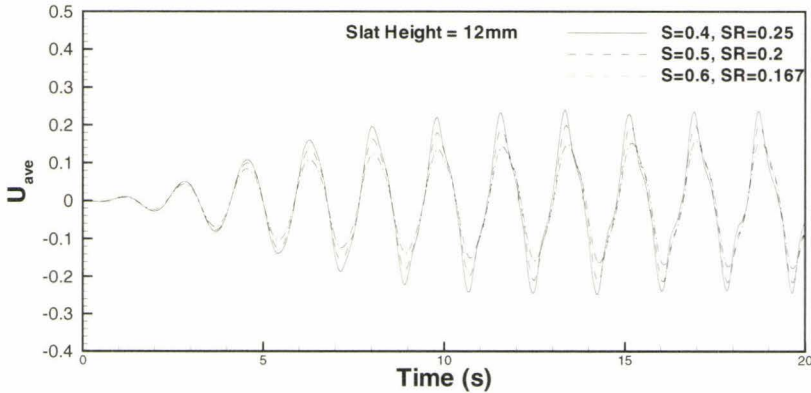


Figure 5-41: Time history of average velocity at the screen location for different solidity ratios and  $D=12mm$ .

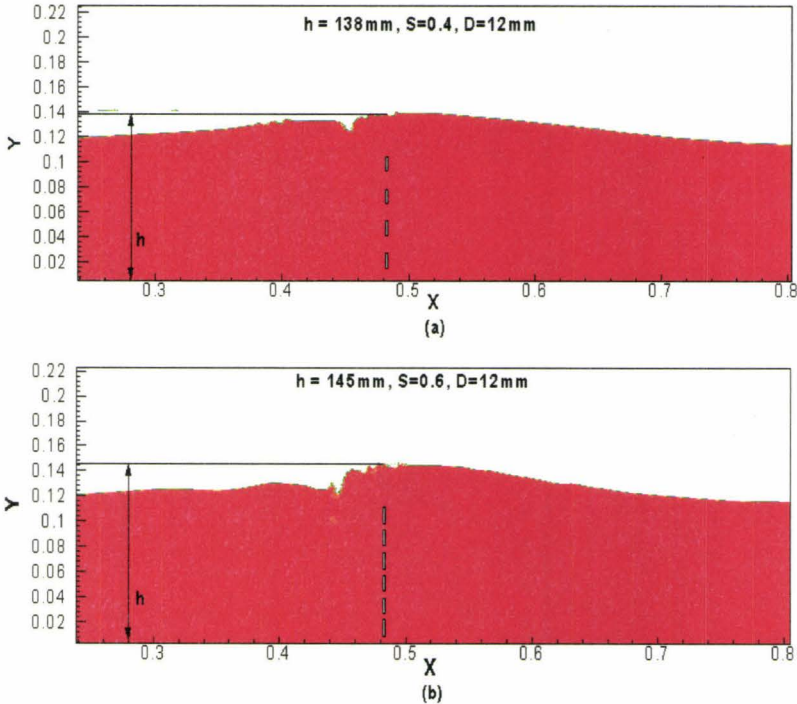


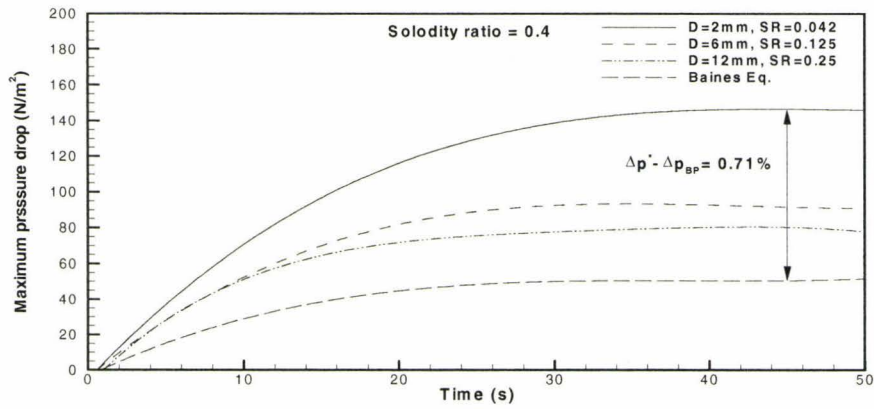
Figure 5-42: Free surface profile at  $t=59s$  for (a)  $S=0.4, SR=0.25$  and (b)  $S=0.6, SR=0.167$

This trend could be attributed to the fact that more fluid moves above the screen as the solidity increases. Results show that fluid height at the location of the screen increases as the solidity ratio increases. For the same mass flow, this subsequently leads to a lower average velocity at the screen. Figure 5-42 shows the free surface profile at  $t=59$  s for  $S=0.4$  and  $0.6$  and  $D=12$ mm.

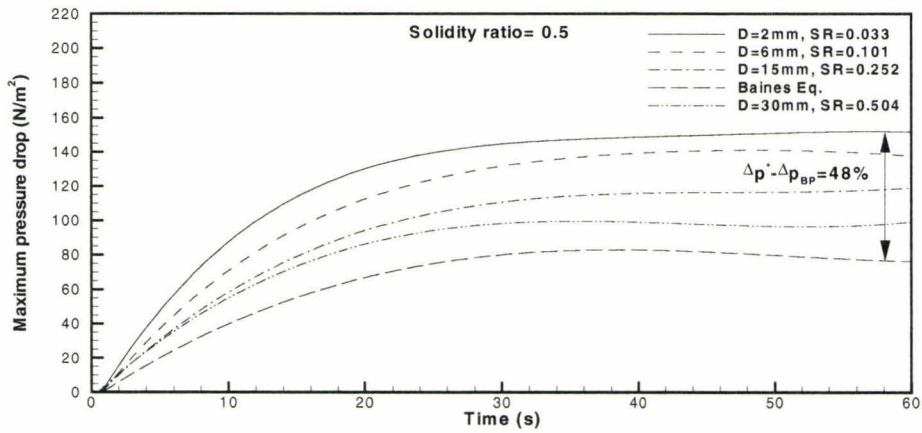
A set of numerical runs were conducted to investigate the effect of SR or D on the pressure drop at the same solidity ratio. Numerical results shown in figure 5-43 indicate that at a constant solidity ratio, reducing the slat height resulted in a higher pressure drop. Figure 5-43 shows the difference between pressure drop calculated using BP's equation,  $\Delta p_{BP}$ , and pressure drop calculated by using the present numerical algorithm,  $\Delta p^*$ .

Results indicate that  $\Delta p_{BP}$  becomes significantly lower than  $\Delta p^*$  as the slat height decreases. This trend is observed for all solidity ratios. BP's equation under predicted  $\Delta p^*$  in all cases. The difference  $(\Delta p^* - \Delta p_{BP})$  decreased as S increased and as SR increased.

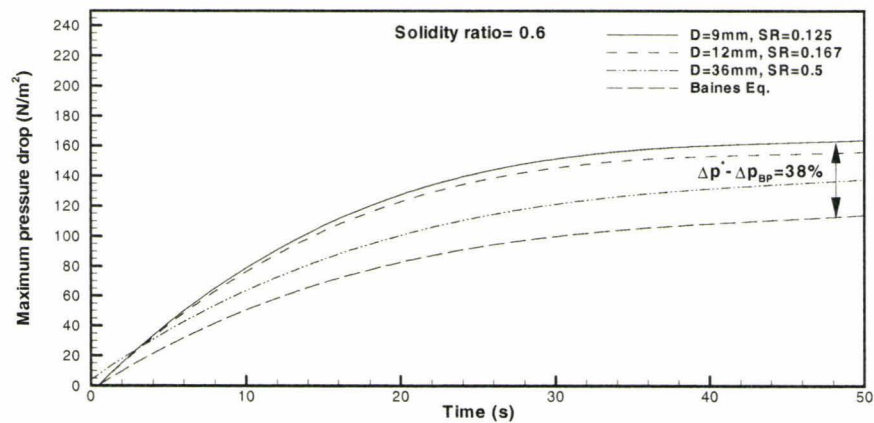
In order to understand the physical explanation of this trend, the validity of the assumptions which had been used to derive BP's equation had to be investigated. The main assumption used to obtain BP's equation was that the flow between the slats is a potential flow. The values of the vorticity in all flow fields showed that this assumption is not valid in most cases.



(a)



(b)



(c)

**Figure 5-43: Variation of the maximum pressure drop through screen with time using various solidity ratios**

Figure 5-44 shows the vorticity field for the case of  $S=0.5$  and  $D=5$  mm. A high value of vorticity (up to 100% of the maximum vorticity value generated in the whole fluid field) was found between the slats in this case.

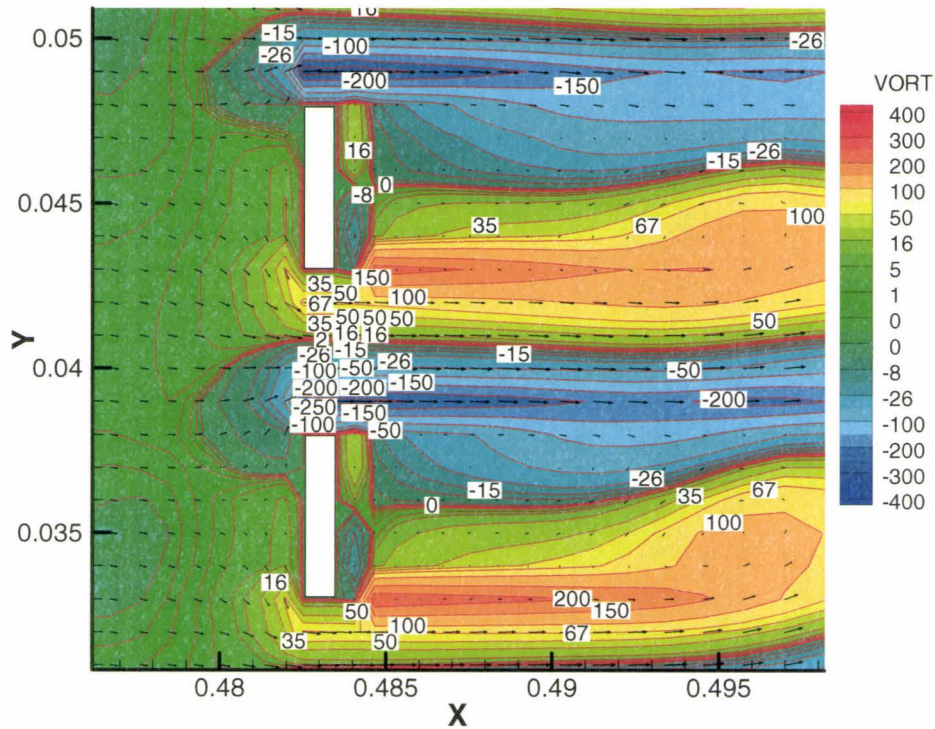


Figure 5-44: Vorticity field for the case of  $S=0.5$ ,  $D=5$  mm ( $SR=0.0833$ ).

At each solidity ratio, when the slat height ( $SR$ ) is increased, the spacing between the slats is consequently increased. This increase results in a decrease in the vorticity between the slats, and the value of the pressure drop  $\Delta p_{BP}$  becomes closer to the real values ( $\Delta p^*$ ). Figure 5-45 shows the vorticity field for the same solidity ratio,  $S=0.5$  and  $D = 30$ mm.

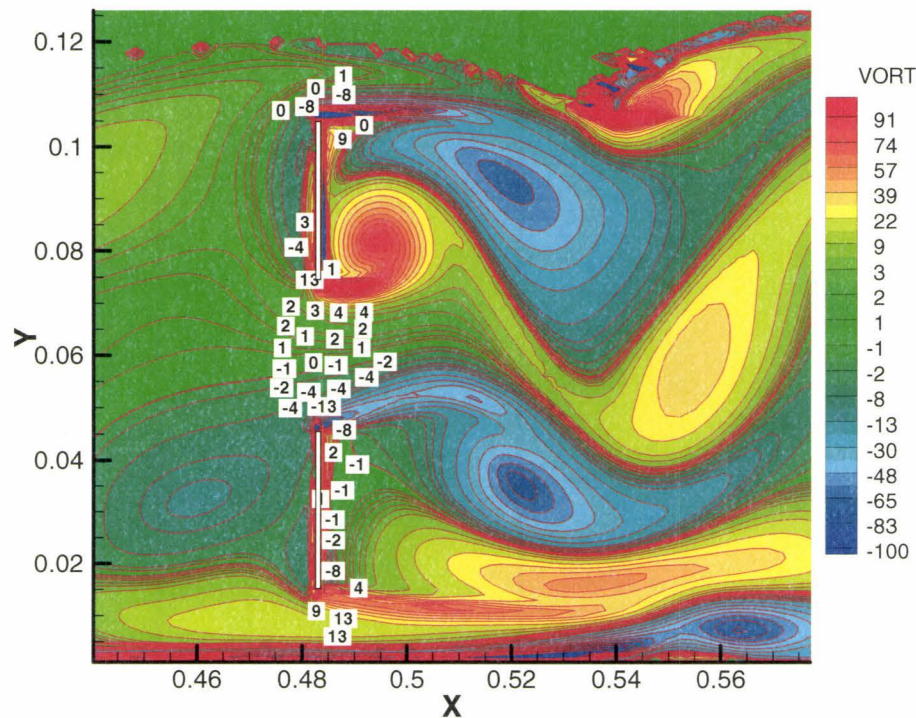


Figure 5-45: Vorticity field for the case of  $S=0.5$  and  $D=30$  mm ( $SR=0.5$ ).

At each solidity ratio and different slat heights, the vorticity field was investigated. A parameter  $L_v$  has been defined as the distance within the screen opening that represents the portion of fluid that has low vorticity. This newly introduced parameter in this study will be termed "irrotational length". In the past literature it was considered that any value for vorticity less than 14 was considered low vorticity  $v$  [43]. In this study, values less than  $\pm 10$  are considered low vorticity. Figure 5-46 shows the vorticity field for  $S=0.4$  at different slat ratios.

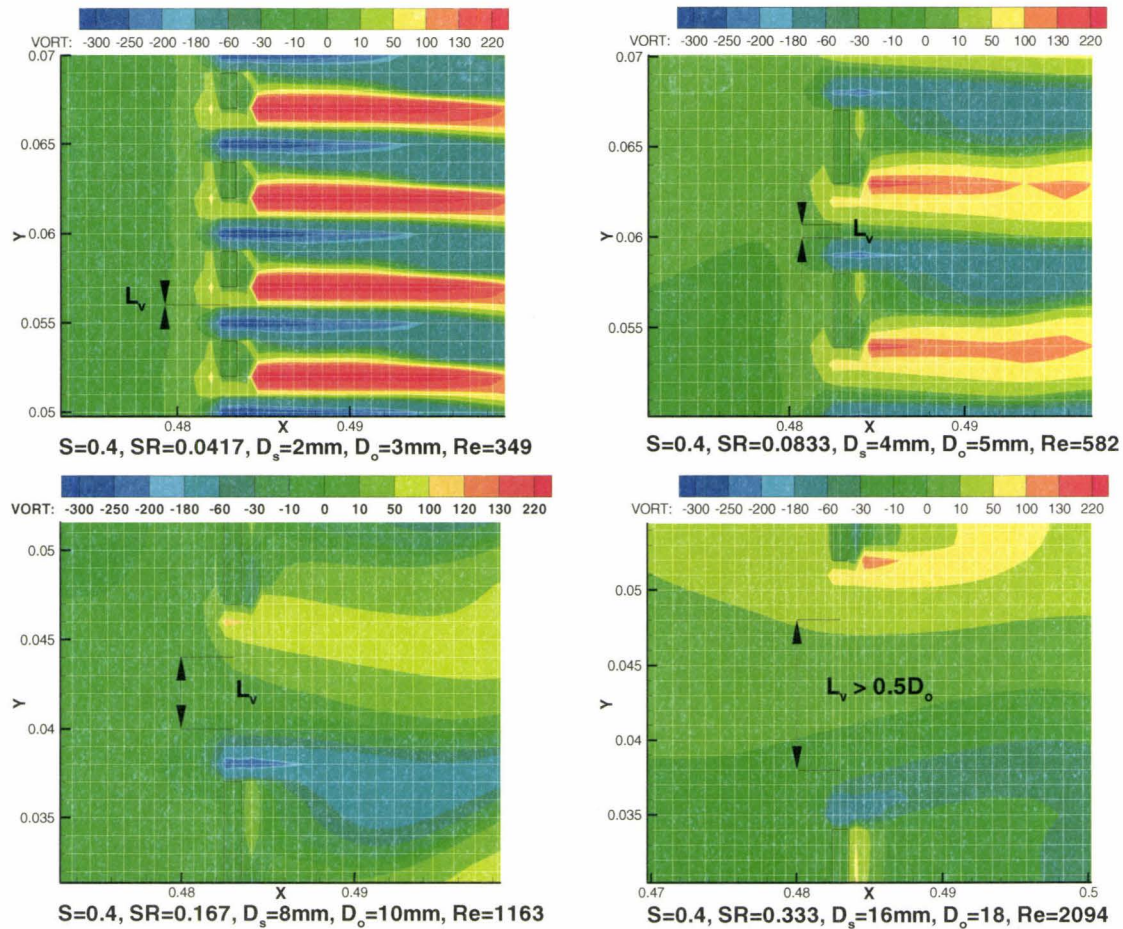


Figure 5-46: Vorticity field for  $S=0.4$

In all the slat ratios, the slat thickness in the direction parallel to the flow is constant. This fact directly leads to fluid flow regime around the edge to be similar in all the cases of slat ratios. As the slat ratios increase (i.e slat height ( $D$ ) increases and so opening height ( $D_o$ ) increases), the edges are further away from each other and Reynolds number defined based on the opening height ( $D_o$ ) becomes higher. Reynolds number is defined as:  $Re = \frac{U_c D_o}{\nu}$  where the characteristic velocity is calculated from the amplitude and frequency of the harmonic excitation as follows:

$$U_c = A.\omega \quad (5-8)$$

Figure 5-46 shows that as the Reynolds number increases due to increasing the opening height ( $D_o$ ), the irrotational length between the slats becomes larger. In that case, the high vorticity zones at each edge are further apart.

On the other hand, with slat height decrease, the edges pull closer together, and the recirculation zones around each edge disturb the flow coming through the openings to a larger extent. At a certain point, the portion of flow unaffected by high vorticity zones at the edges almost vanishes, as is seen for  $SR=0.0417$  at  $S=0.4$ .

The vorticity fields obtained for other solidity ratios ( $S=0.5$  and  $0.6$ ) indicate this fact. Figures 5-47 to 5-48 show the vorticity field for  $S=0.5$  and  $0.6$ .

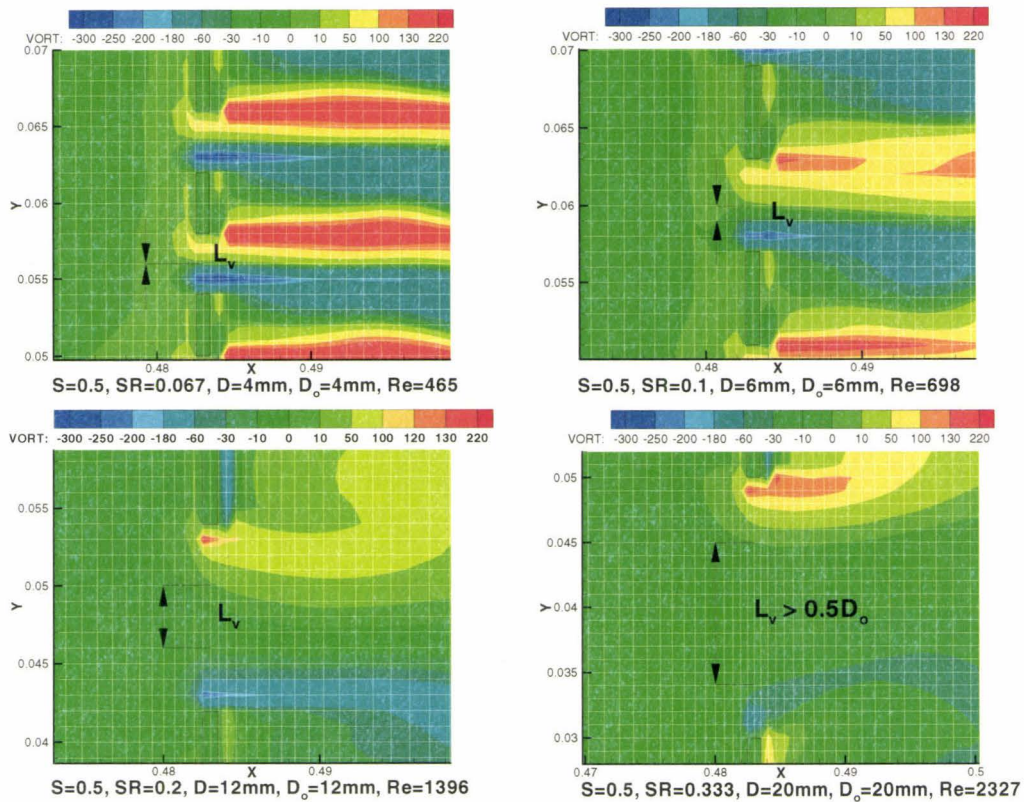


Figure 5-47: Vorticity field for  $S=0.5$

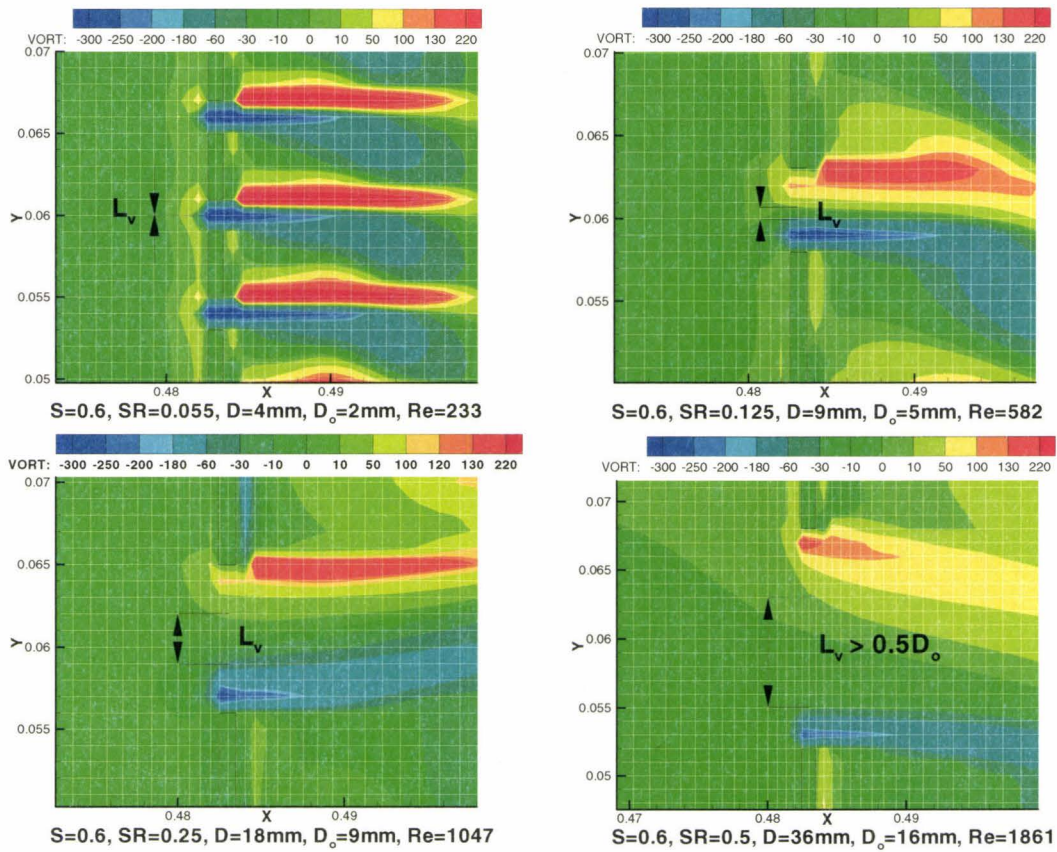


Figure 5-48: Vorticity field for  $S=0.6$

It is observed that in all solidity ratios, as the slat ratio increases the irrotational length becomes larger and so BP's equation gives a better approximation for the pressure drop due to screen.

This has led to the conclusion that a correction factor as a function of Reynolds number was needed to improve the estimate of BP's equation. In the next section, this correction factor is introduced.

### 5.5.4 Proposed Modification to Baines and Peterson's Equation

Figure 5-49 shows the pressure ratio ( $\Delta p^* / \Delta p_{BP}$ ) versus Reynolds number (Re) for solidity ratios  $S=0.4, 0.5$  and  $0.6$ .

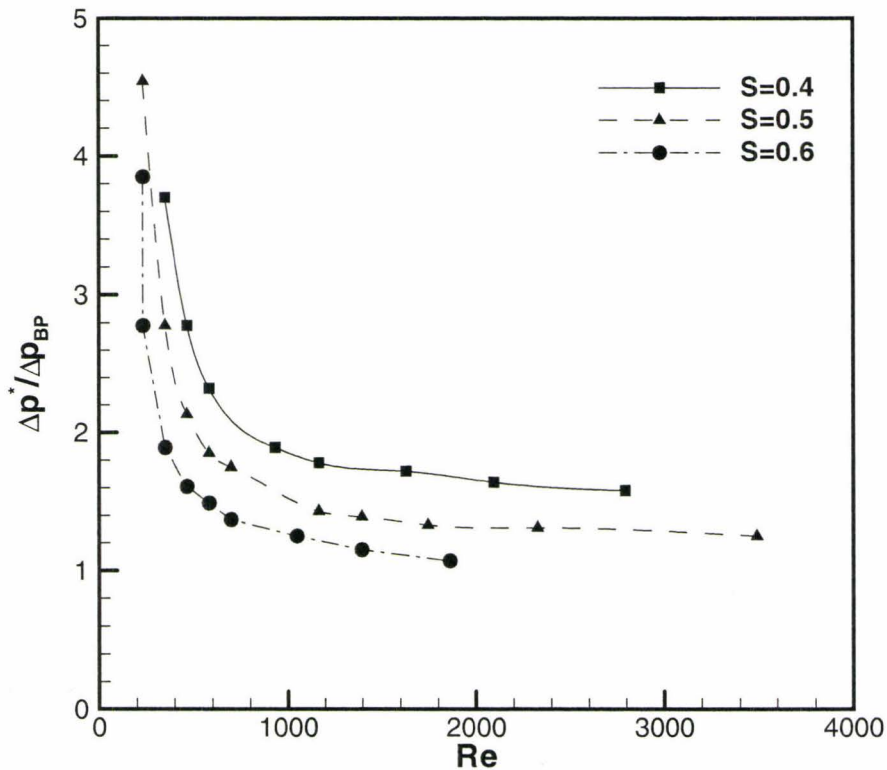


Figure 5-49: Pressure ratio curve for different solidity ratios

These results indicate that, at each  $S$ , the ratio of  $\Delta p$  calculated by using the present numerical algorithm ( $\Delta p^*$ ) and  $\Delta p$  calculated using BP's equation ( $\Delta p_{BP}$ ) decreases as Reynolds number increases. Increasing Reynolds number by increasing the opening height ( $D_o$ ), increases the irrotational length ( $L_V$ ) and so the pressure ratio shown

in figure 5-49 tends to reach unity. Scaling  $\Delta p^*/\Delta p_{BP}$  with respect to  $S=0.4$  by multiplying  $(\Delta p^*/\Delta p_{BP})$  by  $(S/0.4)$  makes all results collapse on one curve as shown in figure 5-50.

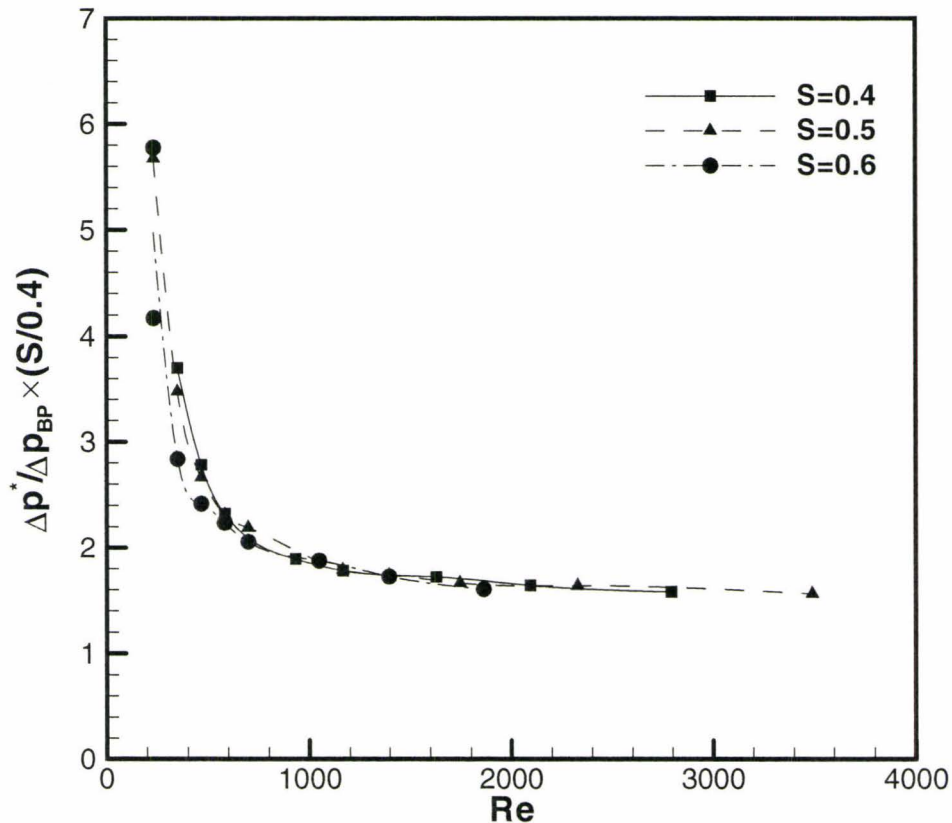


Figure 5-50: Pressure ratio scaled curve for different solidity ratios

This indicates that these results can be correlated using a correlation in terms of function of  $Re$  and  $S$ . This correlation takes the following form:

$$C_m = \frac{\Delta p^*}{\Delta p_{BP}} = \left( 1.185 - \frac{135.87}{Re} + 0.569 \ln(S) \right)^{-1} \quad (5-9)$$

As mentioned previously, the main attribute that made Baines and Peterson equation very popular is its simplicity. Introducing  $C_m$  as a correction factor for BP's equation would allow one to employ this simple equation and at the same time account for the effect of screen pattern. The validity of using  $C_m$  to calculate pressure ratio has been shown in figure 5-51 for  $S=0.4$ ,  $0.5$  and  $0.6$ . The validity of  $C_m$  has been tested for various values of SR at each  $S$ . Figure 5-51 (a) shows a comparison between the values of  $C_m$  calculated by using the numerical algorithm and the ones calculated by the proposed correlation, equation (5-9), at  $S=0.4$ .

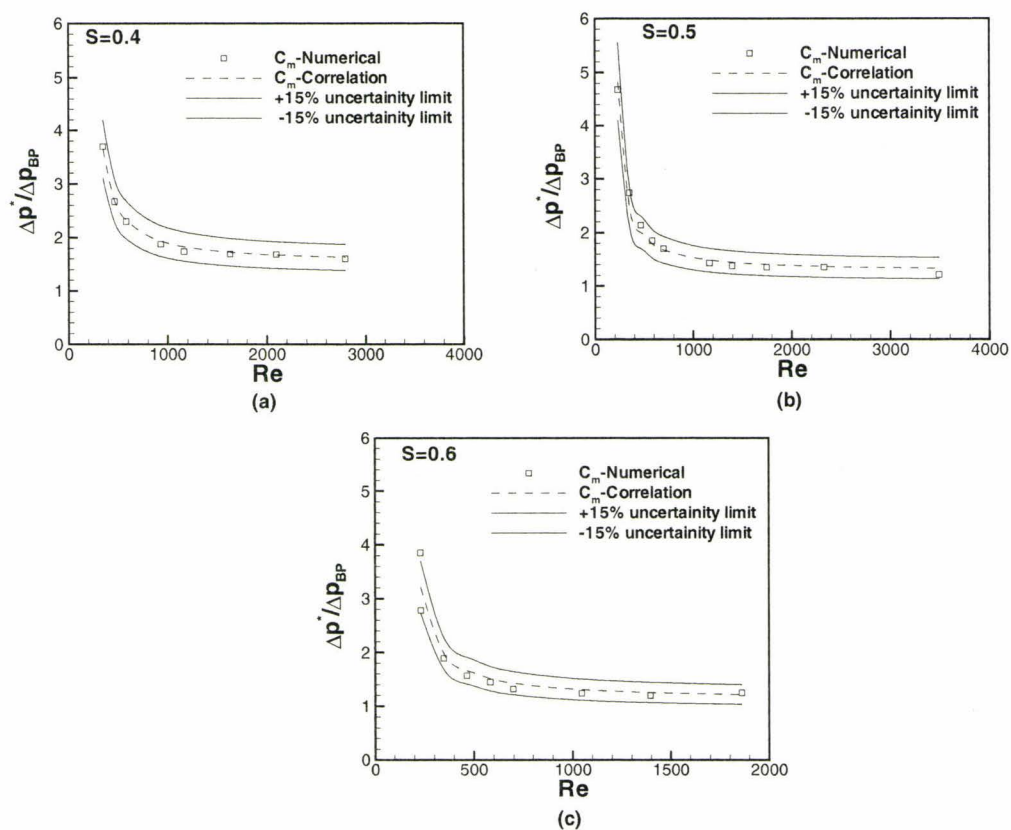


Figure 5-51: Comparison of the values of  $C_m$  determined from algorithm and the proposed correlation at different  $S$  and SR, (a)  $S=0.4$  , (b)  $S=0.5$  , (c)  $S=0.6$ .

In figures 5-51 (b) and (c), this comparison has been carried out for  $S=0.5$  and  $0.6$ , respectively. Results indicate that in all cases, the calculated pressure ratio by equation (5-9) is within  $\pm 15\%$  of the pressure ratio calculated by the present algorithm.

Equation (5-9) has been developed for harmonic excitation with amplitude excitation equals to  $42\text{ mm}$  and frequency of  $0.54\text{ Hz}$  which is very close to the natural frequency of the TLD. Figure 5-52 show the pressure drop values at other excitation amplitudes and frequencies.

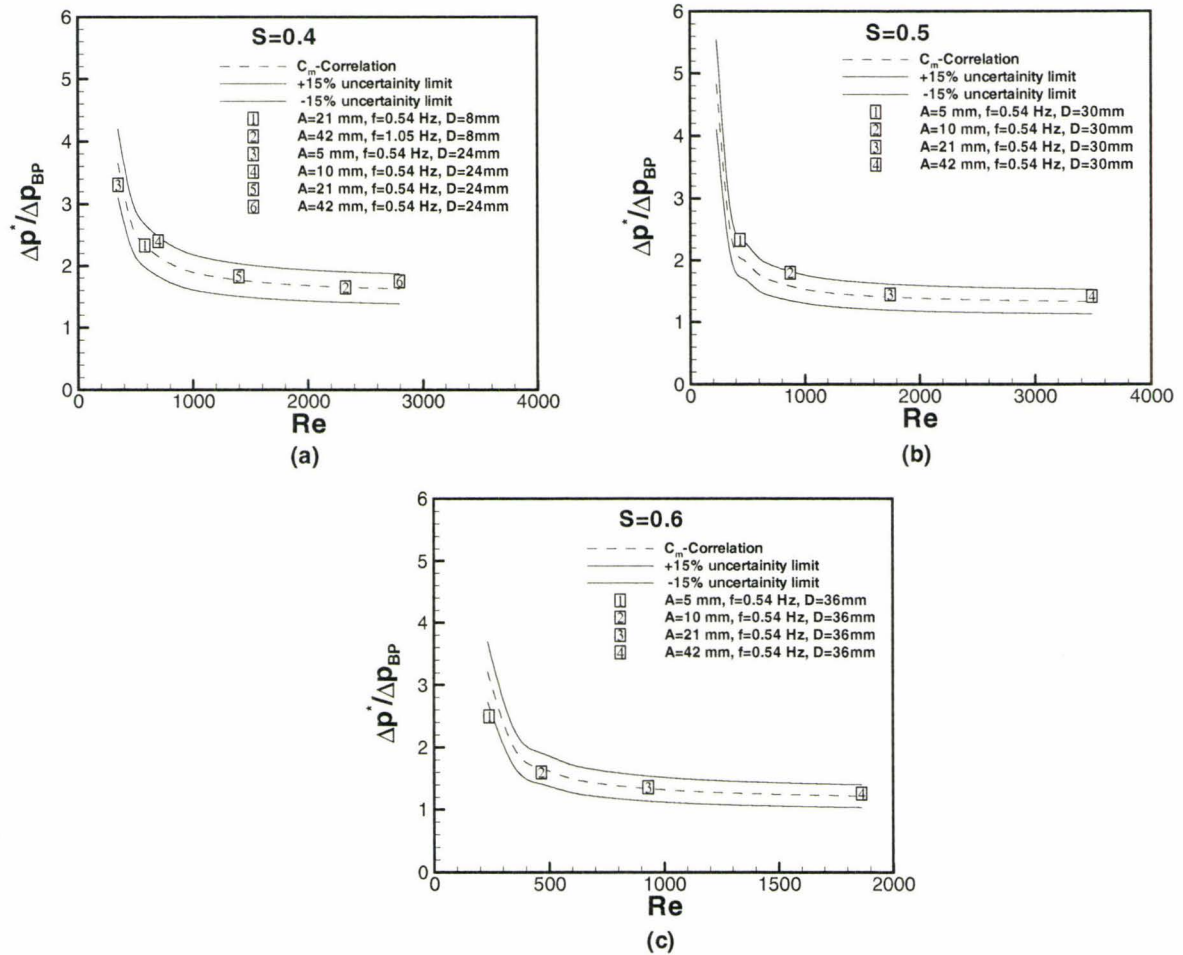


Figure 5-52: Comparison of the values of  $C_m$  determined from the present algorithm and the proposed correlation at different amplitudes and  $S$  (a)  $S=0.4$  , (b)  $S=0.5$  , (c)  $S=0.6$ .

Figure 5-52 (a) compares the pressure ratio at  $S=0.4$  for other amplitudes and frequency with the calculated  $C_m$  by equation (5-9). This comparison for  $S=0.5$  and  $0.6$  has been shown in figure 5-52 (b) and (c). Results indicate that in all cases the corrected  $\Delta p$  is within the range of uncertainty of the correlation at the corresponding value of Reynolds number.

### 5.5.5 Effect of Screen Pattern on Natural Frequency of the TLD

The natural frequency is one of the TLD design parameters. It depends on the tank length ( $L$ ) and liquid height ( $h$ ). It can be estimated using the linear wave theory according to Lamb (1932) using the following equation:

$$f_w = \frac{1}{2\pi} \sqrt{\frac{\pi g}{L} \tanh\left(\frac{\pi h}{L}\right)} \quad (5-10)$$

A TLD is considered properly tuned when its natural frequency is the same as, or at least close to, the natural frequency of the structure. Equation (5-10) does not produce the correct natural frequency of a TLD in case of any nonlinearity. Furthermore, it does not account for the effect of screens on the natural frequency of the TLD. It is worth noting here that the effect of screens and screen pattern on the TLD natural frequency has not been studied numerically before. The main goal of this section is to use the developed algorithm to calculate the actual natural frequency of the TLD considering the effect of screens and their pattern. The natural frequency could be obtained by performing what is called a discretized frequency sweep analysis.

This sweep analysis is carried out using harmonic external excitations, and the amplitude of excitation is kept constant while the frequency is varied and the maximum deflection of the free surface at a location close to the side wall ( $x = 0.05 \times L$ ) in the tank is determined at each excitation frequency.

The response of the free surface is a combination of several harmonic responses. By using the Fast Fourier Transform (FFT), the free surface response is filtered and the maximum deflection of the free surface at the first mode is determined for each frequency. The excitation frequency at which the maximum deflection reached its peak is considered as the natural frequency of the TLD.

This analysis is carried out for a TLD with a single screen placed in the middle. The solidity ratio of the screen is 0.42 and the analysis was completed for slat heights of 10 mm and 25 mm, corresponding to slat ratios of 0.2 and 0.5, respectively. The excitation function is harmonic with an amplitude of 2.5 mm. The TLD properties are the same as the ones shown in table 4.4. Figure 5-53 shows the schematic of the two cases considered in this analysis. The thickness of each slat and the distance of the first slat from the bottom of the tank are 1mm and 3mm, respectively.

Figure 5-54 shows the results of the frequency sweep analysis for the two screens. Although the solidity of the two screens is the same, the natural frequency of the TLD did change due to the change in the screen pattern. This phenomenon would not have been detected without resolving the flow field around and through the screen.

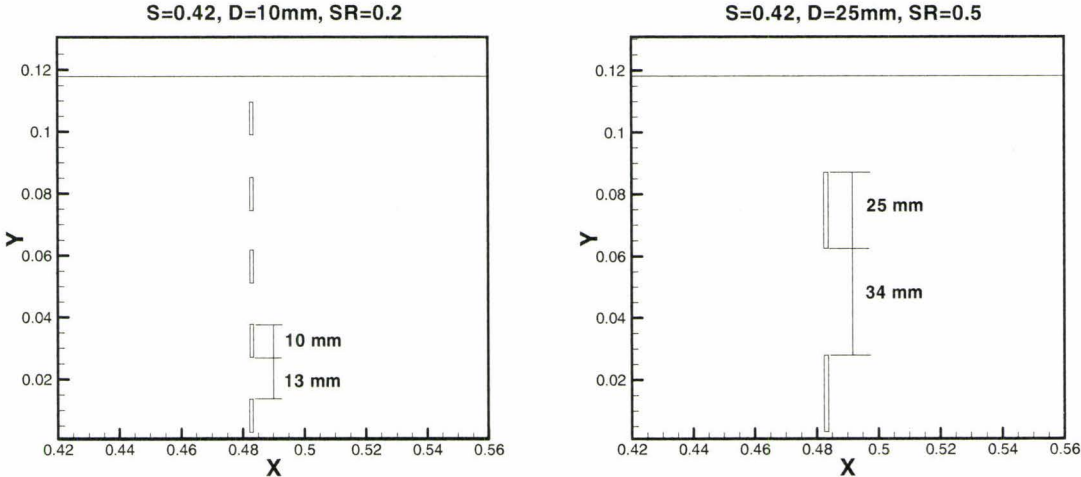


Figure 5-53: Configuration of slat screens used in the frequency sweep analysis

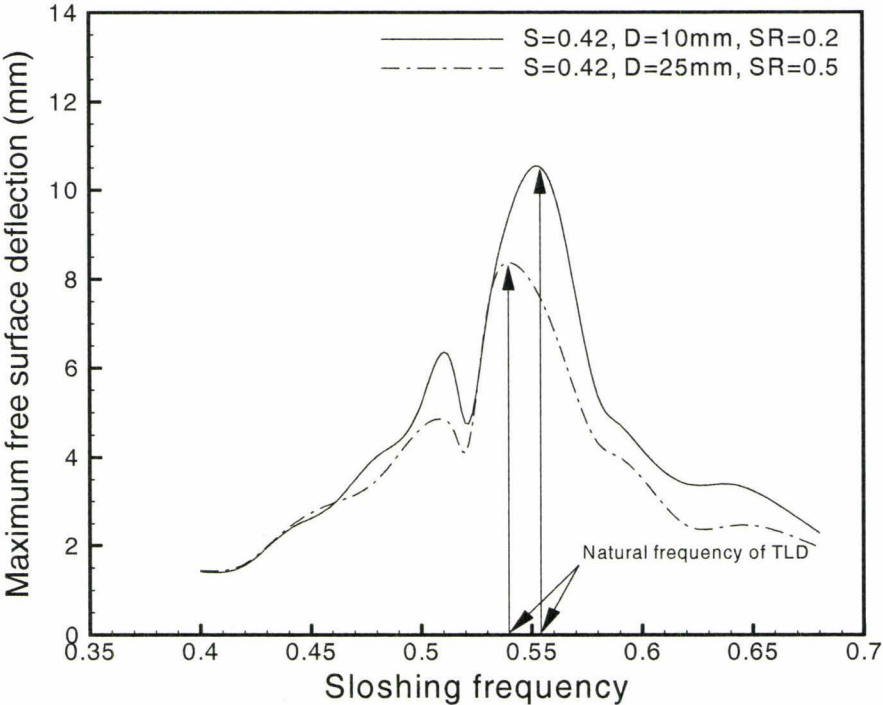


Figure 5-54: Variation of the maximum free surface deflection at x=48.3 mm as a function of frequency of external excitation for a TLD equipped with one screen having the same S and two different slat ratios.

When the slat height was changed, the size and combination of generated vortices behind each slat became different, and the merging of these vortices happened in an unpredictable way. These generated vortices changed the momentum of fluid particles, thus resulting in different free surface deflections. Figure 5-55 indicates the generated vortices for the cases of  $D=10$  mm and 25 mm at  $S=0.42$  and  $f=0.54$  Hz.

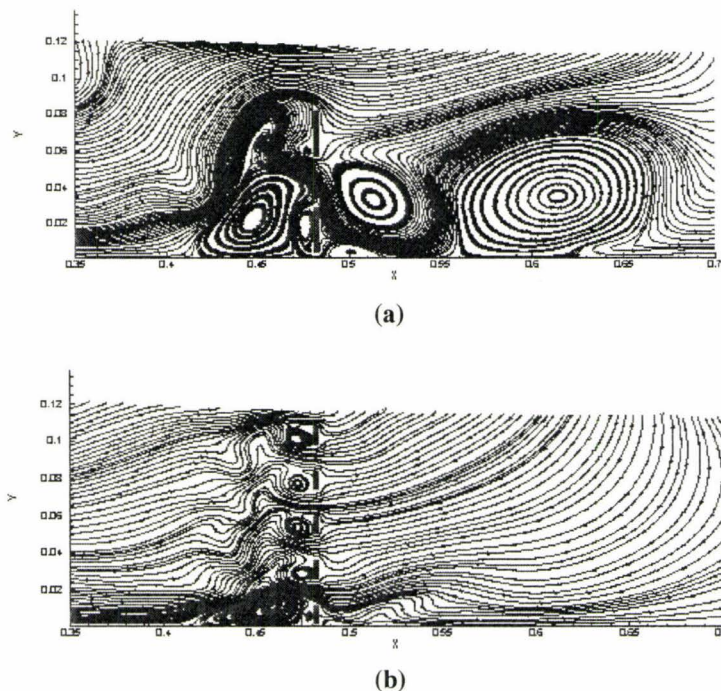
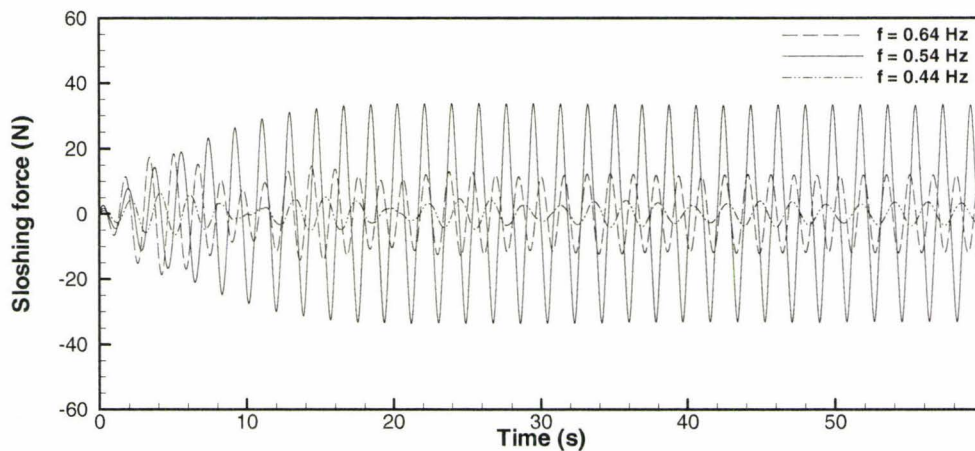


Figure 5-55: Flow pattern around the screen,  $S=0.42$ ,  $f=0.54$  Hz, (a)  $D=25$ mm, (b)  $D=10$ mm at  $t=25$  s

It is important to note that the effect of the screen pattern on the natural frequency and inherent damping of the TLD was more obvious when the momentum of fluid particles passing through the screen was high. For smaller velocities at the screen location, there was no difference in the performance of TLD for different screen patterns.

This fact can be seen clearly in figure 5-54 in the region of low frequency, where the free surface deflection was almost identical for the two screen patterns. On the other hand, the maximum difference in the free surface deflection occurred around the natural frequency of the TLD, where the momentum of fluid particles in the x- direction at the screen location was higher because of the stronger sloshing force. Figure 5-56 indicates the generated sloshing force at different frequencies for the case of screen with  $D=10\text{mm}$ . The results show that the sloshing force is significantly larger at the frequency  $f=0.54\text{ Hz}$  close to the natural frequency of TLD.



**Figure 5-56: Sloshing force at different frequencies for the case of screen with  $D=10\text{mm}$ .**

The effect of the screen pattern can be modeled by proposing a new parameter termed as the effective solidity ratio, which is introduced in this study as the sum of the physical solidity ratio of screen and an additional solidity ratio ( $S_{add}$ ), i.e.

$$S_{eff} = S_{phys} + S_{add} \quad (5-11)$$

Accordingly, the effective solidity ratio is a combination of the physical solidity of the screen and an additional factor that represents the effect of the screen pattern on the developed vortices and on the change in the momentum of the sloshing fluid.

The value of  $S_{add}$  depends on many parameters that contribute to the flow details around the screen. These parameters include: slat height, slat thickness, fluid height, tank size, the distance of the first slat from the bottom of the tank, solidity ratio, screen location, number of screens, amplitude of excitation, frequency of excitation, and excitation function. It is clear that there is no way to consider the effect of all these parameters and present a simple relation for  $S_{add}$  to accommodate these effects. Therefore, resolving the flow through the screen is the only way that would facilitate accounting for the contribution of all these parameters and present the correct effect of the screen on the performance of the TLD.

Now the question is how this additional solidity is created? Physically, under the effects of all the above mentioned parameters, some vortices are generated around the screen during the sloshing motion. Screens having higher slat ratios and the same solidity ratio have larger openings, and larger slat heights. This causes the flow to create larger vortices as shown in figure 5-57 (a). The formed large vortices become significant in deciding the fluid flow regime, as they form major obstruction zones. Thus the size of the screen opening is no longer the deciding factor of the fluid movement through the screen.

These obstruction zones reduce the momentum of the fluid at the screen. A screen with a smaller slat ratio has a smaller opening. In this case, the formed vortices and recirculation zones behind the screens are relatively small. The inertia in this case is the

dominant factor in deciding the fluid flow character, and the formed vortices decay quickly under the effect of fluid inertia, thus the size of screen opening becomes the deciding factor, figure 5-57 (b).

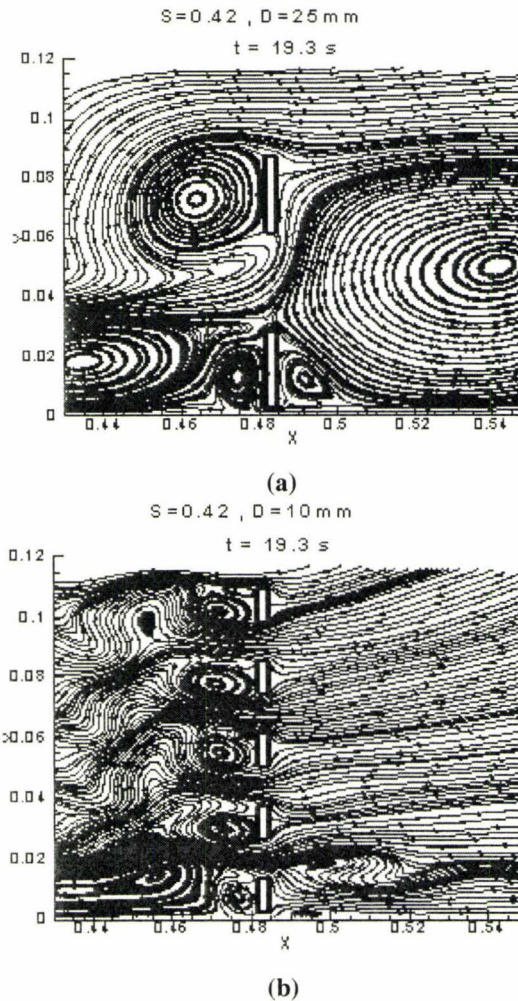


Figure 5-57: Flow patterns around two screens with the same solidity ratio and different slat ratios

(a)  $D=25\text{mm}$  and  $SR=0.5$  , (b)  $D=20\text{mm}$ ,  $SR=0.2$

Figure 5-58 shows the effect of SR on the average velocity at the screen in a TLD exposed to harmonic excitation with frequency of 0.54 Hz and amplitude of 2.5 mm. Results indicate that the higher slat height (25mm) had a lower velocity value by up to

31% at the screen because of the effect of the larger generated vortices. Consequently for this case, it was expected that free surface deflection would generally be lower in value as well. This had been shown before in figure 5-54 at the region of frequency close to the natural frequency of the TLD.

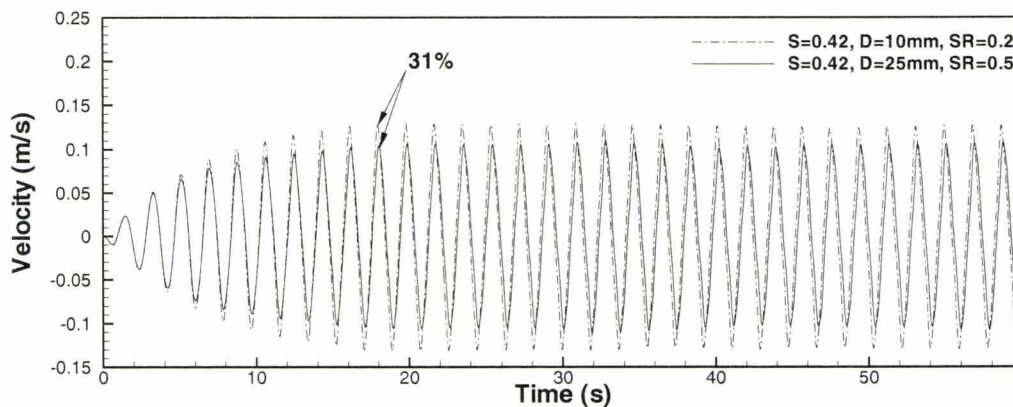


Figure 5-58: Effect of SR on the average velocity at the screen for  $f=0.54$  Hz and  $A=2.5$  mm.

Figure 5-59 shows the variation of free surface deflection at  $x=48.3$  mm with time during TLD operation under variation of the excitation frequency of 0.54 Hz and  $A=2.5$  mm for the two cases shown in figure 5-58.

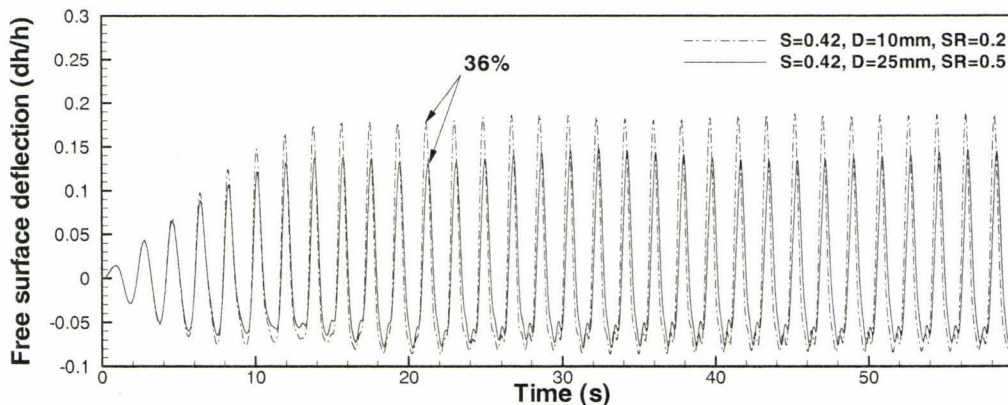


Figure 5-59: Effect of screen pattern on free surface deflection at  $x=48.3$  mm.

In agreement with figure 5-58, the free surface deflection for the slat height of 25 mm is considerably less than its value for slat height of 10 mm by up to 36%.

It was also expected that the sloshing force would increase with higher velocity values at the screen. Figure 5-60 confirmed this fact by comparing the generated sloshing force for the two slat heights, and concluding that the sloshing force for the slat height of 10 mm was higher than the one for slat height of 25 mm by up to 26%. That is equivalent to saying that smaller slat heights impose more effective damping due to having the additional solidity ratio.

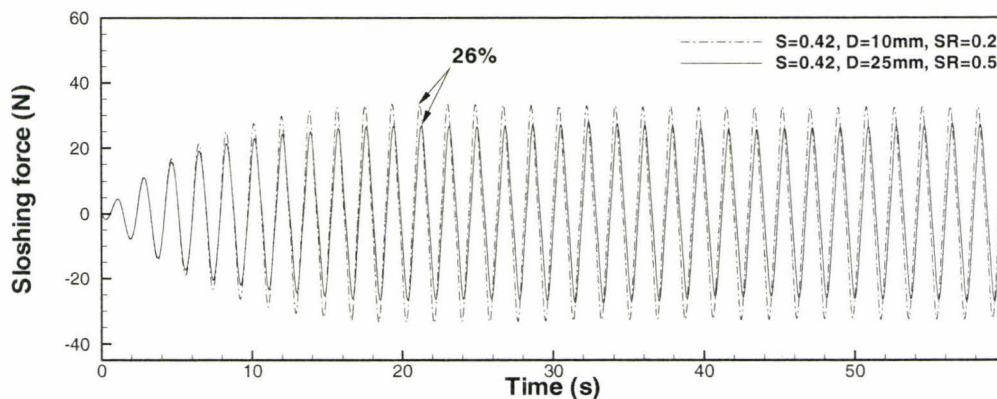


Figure 5-60: Effect of screen pattern on sloshing force for  $f=0.54$  Hz and  $A=2.5$ mm.

In order to have a better understanding of the proposed concept of additional solidity, flow patterns around the two screens are shown at different times in figures 5-61 and 5-62. Because of the dependence of the additional solidity term on the size and location of the generated vortices, which in turn change with time, the study of these flow patterns clearly reveals why the additional solidity ( $S_{add}$ ) has an unpredictable time dependant value.

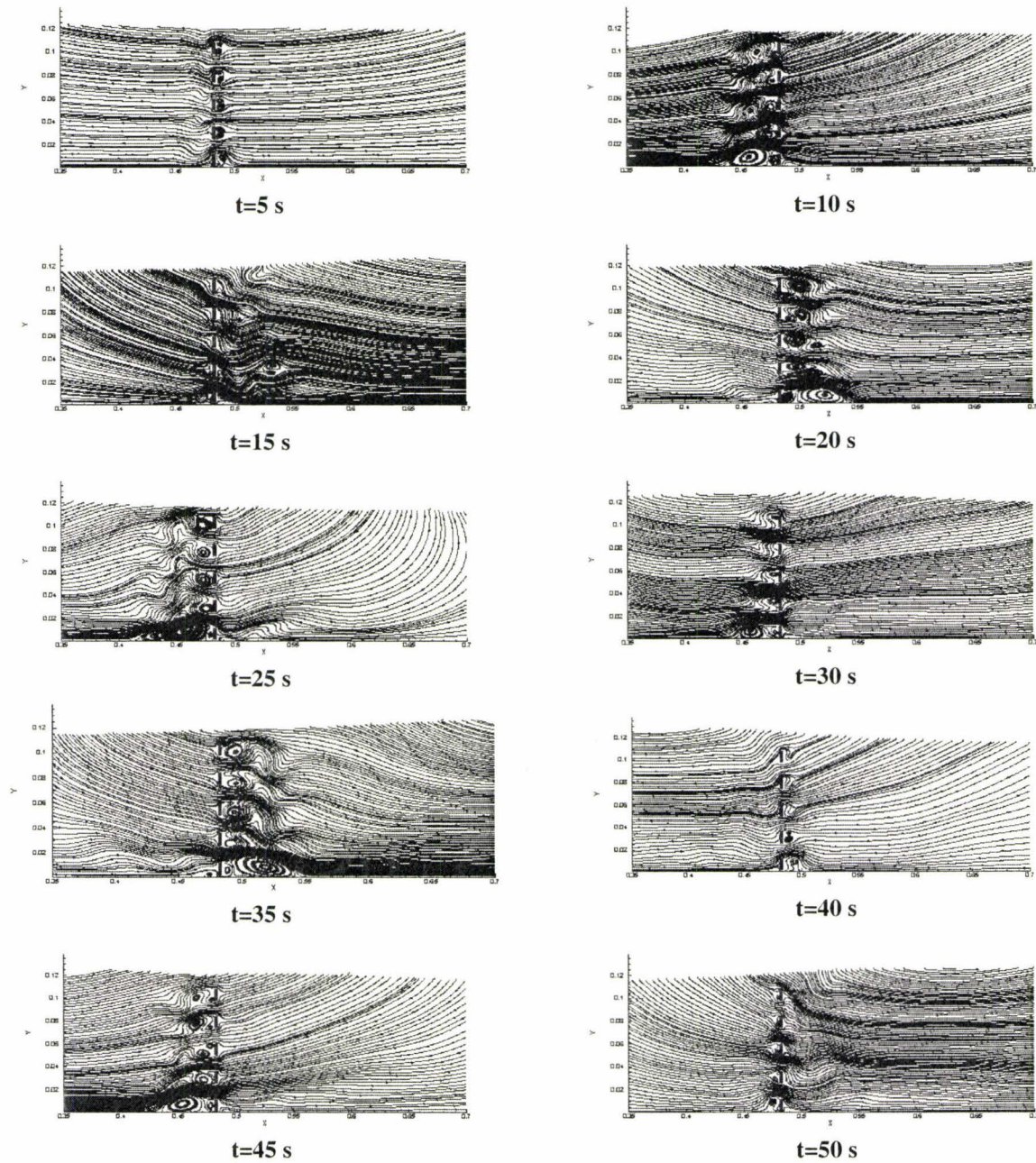


Figure 5-61: Flow patterns around the screen with  $S=0.42$  and  $D=10$ mm at different times

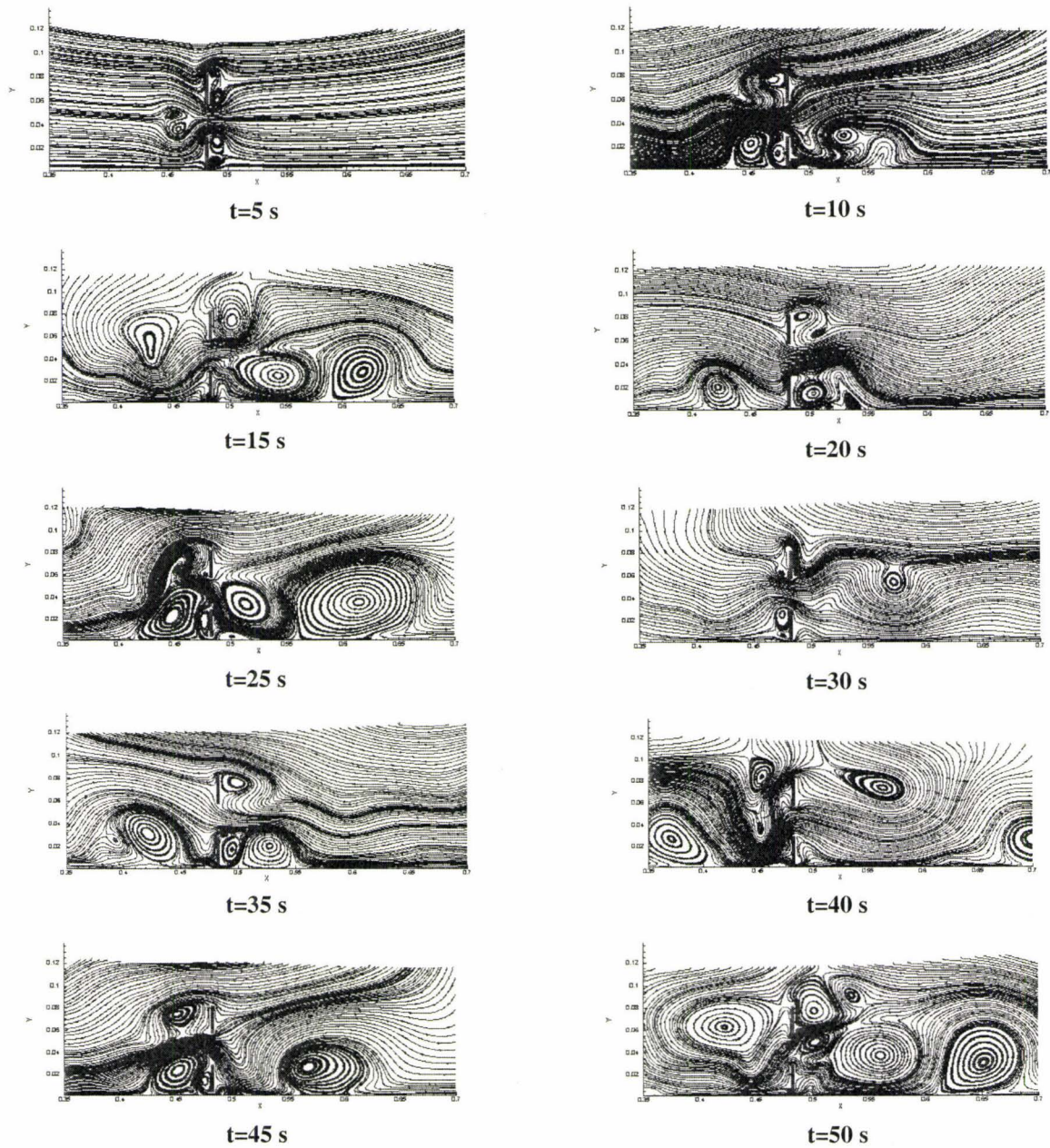


Figure 5-62: Flow patterns around the screen with  $S=0.42$  and  $D=25$ mm at different times

## 5.6 Determination of the Effective Solidity Ratio

It is important to obtain an approximate estimation of the effective solidity of screens and also for the additional solidity for a screen with a specific slat height (or slat ratio). For this purpose, the Baines and Peterson's equation with the proposed correction factor was employed to calculate the effective solidity ratio. Assuming the solidity ratio in BP's equation to be the effective solidity ratio of the screen, and equating this equation with the corrected  $C_l$  value leads to the following equation:

$$\left( \frac{1}{C_c(1-S_{eff})} - 1 \right)^2 = C_m \left( \frac{1}{C_c(1-S_{phys})} - 1 \right) \quad (5-12)$$

From this equation,  $S_{eff}$  can be determined as:

$$S_{eff} = 1 - \frac{1/C_c}{1 + \sqrt{C_m} \left( \frac{1}{C_c(1-S_{physical})} - 1 \right)} \quad (5-13)$$

where  $C_m$  is the correction factor of BP's equation presented by equation (5-9). So the additional solidity term can be approximated as:

$$S_{add} = 1 - S_{phys} - \frac{1/C_c}{1 + \sqrt{C_m} \left( \frac{1}{C_c(1-S_{phys})} - 1 \right)} \quad (5-14)$$

Using equation 5-13, the effective solidity was calculated and shown in figure 5-63. As can be seen from this figure, increasing the slat height decreased the effective solidity due to formation of the large obstruction (circulation) zones at the screen as shown in figure 5-63.

It can be concluded that decreasing the slat height, i.e. increasing the effective solidity ratio, lead to increasing the inherent damping of the screen and so the inherent damping of the TLD.

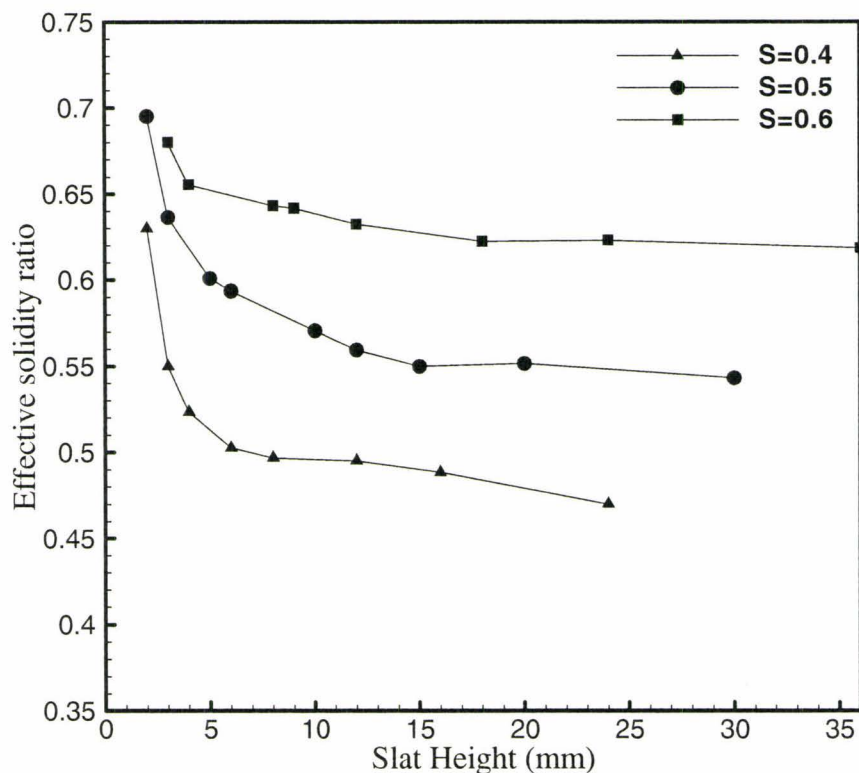


**Figure 5-63: Effective solidity ratio as function of slat height for a TLD equipped with one screen placed in the middle.**

The effective solidity ratio curves shown in figure 5-63 can be used along with BP's equation to calculate pressure drop through slat screens with different solidity ratios and slat heights. This approach would simplify the analysis because in this case a screen can be dealt with as a point resistance and it still allows one to account for the effect of screen pattern, which has been shown in this study to have a significant effect on flow pattern and the TLD performance.

## Chapter 6: Summary, Conclusion and Future Work

### 6.1 Summary and Conclusion

Installing screens in TLDs has proven to be supremely effective on many different levels. It helped bring up the inherent damping of the TLD to a desired optimal value for sufficient motion suppression in civil structures. Its introduction also imposed a more linear and predictable behavior to the sloshing motion for the fluid inside the TLD. In previous numerical efforts the effect of the screen was handled as a point hydraulic resistance inside the TLD. Upon the understanding of the importance of the screen effect, this current study's primary focus was to properly model the sloshing motion of water inside the TLD, and resolve the flow details through the screen. The slat screen type was selected in this research because changing its pattern could be done easily just by changing the slat height and the spacing. This enabled the flexibility necessary to reach the targeted amount of inherent damping for TLD. The developed numerical algorithm is an integrated fluid-structure model in which the response of the structure is determined under the effect of TLD with and without screen.

The model has been developed based on the finite-difference method. The free surface was reconstructed through the use of the volume of fluid method using a fixed grid. The donor-acceptor technique was used for tracking the volume fraction field. Details of the flow through screens have been resolved using the partial cell treatment method. The interaction of the TLD and a single degree of freedom (SDOF) structure has been taken into account and the response of the structure has been determined by solving

the structure equation of motion using the Duhamel integral method. The algorithm has been validated using several experimental sets of data.

The algorithm was able to deal with cases leading to large free surface deformation up to 75% of the initial liquid depth. The algorithm has been tested using both harmonics and random excitations. It was found that although the TLD can effectively reduce the structure deflection, however because of the lack of enough inherent damping in the TLD, the beating phenomenon makes the behavior of the TLD very nonlinear and unpredictable.

Results of this study have shown how a slat screen could increase the inherent damping of a TLD and the structure and make the behavior of the TLD more linear and predictable. Results of this study indicated that screen pattern has a considerable effect on the performance of the TLD and on the response of the structure. Results indicated that changing the slat height from 25 mm to 10mm could make change the response of the structure by up to 33%, which is quite significant.

A new physical parameter, termed as screen slat ratio (SR) has been introduced for the first time in this research, to characterize the effect of screen pattern. The developed algorithm has been used to introduce a correction factor to Baines and Peterson equation which has been widely used for the calculation of pressure drop through screens. A new parameter has been introduced as the effective solidity ratio to account for the effect of screen pattern on the calculation of the pressure drop through the screen.

It was found that for slat screens with the same physical solidity ratio, decreasing the slat height would increase the inherent damping of the TLD and consequently decrease the response of the structure. This fact led to the conclusion that decreasing the slat height results in increasing the effective solidity ratio of the screen.

Results of this study indicated that it is important to resolve flow details through the screens in order to have a complete understanding of the effect of screens on the performance of TLDs.

The contributions of this research can be summarized as follows:

- A numerical model has been developed to solve the complicated sloshing fluid motion in a TLD coupled with a single degree of freedom (SDOF) structure and equipped with slat screens.
- The effect of screen pattern on TLD performance and structure response has been investigated.
- The screen slat ratio has been introduced as a new parameter to characterize the effect of screen pattern.
- A correction factor has been introduced and correlated with Reynolds number and the screen solidity ratio.
- The Effective Solidity Ratio has been introduced as a new parameter taking the effect of screen pattern into account.

## 6.2 Future Work

The present numerical algorithm has been developed for two-dimensional flows. Extending it to handle three-dimensional flows in rectangular and cylindrical tanks will be very useful. Expanding the range of parameters considered in this study is definitely another important area for that should be considered in the future.

## References

1. Babaei, R., Abdollahi, J., Homayonifar, P., Varaharam, N., Davami, P. (2006). "Improved advection algorithm of computational modeling of free surface flow using structural grids", *Computational methods and its applications mechanical engineering*, 195, 775-795.
2. Baines, W.D., Peterson, E.G. (1951). "An investigation of flow through screens", *ASME*, Vol. 73, pp 467-480
3. Bassman M. (2000). "A three dimensional model of an impacting droplet", PhD thesis, University of Toronto, Toronto, Canada.
4. Bellet, M., Chenot, J.L. (1993). "A Lagrangian approach to fluid flow in metal casting processes", *Computational Methods for Free and Moving Boundary Problems in Heat and Fluid Flow*, Elsevier, London, pp. 287-316.
5. Celebi, M.S. and Akyildiz, H. (2002). "Nonlinear modeling of liquid sloshing in a moving rectangular tank", *Ocean Engineering*, Vol. 29, pp. 1527-53,.
6. Chan, R.K.C., Street, R.L. (1970). "A computer study of finite amplitude water waves", *Journal of Computational Physics*, 6, pp. 68-94.
7. Chen, W., Haroun, M.A. and Liu, F. (1996). "Large amplitude liquid sloshing in seismically excited tanks", *Earthquake Engineering and Structural Dynamics*, Vol. 25, pp. 653-669.
8. Chen S., Johnson D.B., Raad P.E. (1995). "Velocity boundary conditions for the simulation of free surface fluid flow", *Journal of computational physics*, Vol.116, pp.262-276.
9. Chester, W. (1968). "Resonant oscillations of water waves. II. Experiment", *Proceedings of the Royal Society of London*, Vol. A. 306, pp. 23-39.
10. Chopra. (1995). "Dynamics of structure: Theory and Application to Earthquake Engineering", Prentice Hall: NY, U.S.A
11. Clough, R.W., Niwa, A., Clough, D.P. (1978). "Experimental seismic study of cylindrical tanks", *J. Struc. Div. ASCE*, Vol. 105, pp. 2565-90.
12. Dutta, S. and Laha, M.K. (2000). "Analysis of the small amplitude sloshing of a liquid in a rigid container of arbitrary shape using a low-order boundary element method", *International Journal for Numerical Methods in Engineering*, Vol. 47, pp. 1633-48.
13. Floryan, J.M. and Rasmussen, H. (1989). "Numerical methods for viscous flows with moving boundaries", *Applied Mechanics Review*, Vol. 42, pp. 323.
14. Fujii, K., Tamura, Y., Sato, T., Wakahara, T. (1990). "Wind-induced vibration of tower and practical applications of tuned liquid damper", *Journal of Wind Engineering and Industrial Aerodynamics*, Vol. 33, pp. 263-72.
15. Fujino, Y., Pacheco, B.M., Chaiser, P., Fujii, K. (1988). "An experimental study on Tuned Liquid Damper using circular containers", *JSCE Journal of Structural Engineering*, Vol. 34A, pp. 603-616.
16. Fujino, Y., Sun, L.M., Pacheco, B.M., Chaiser, P. (1992). "Tuned liquid damper for suppressing horizontal motion of structures", *ASCE Journal of Engineering Mechanics*, Vol. 118, pp. 2017-30.
17. Hamed M.S. and Floryan J.M. (1998). "Numerical simulation of unsteady non-isothermal capillary interfaces", *Journal of computational physics*, Vol.145, pp.110-140.
18. Hamelin J. (2007). "The effect of screen geometry on the performance of a Tuned Liquid Damper", MSc. Thesis, McMaster University, Hamilton, Canada.

19. Harlow, F.H., Welch, J.E. (1965). "Numerical calculation of time dependent viscous incompressible flow with free surface", *Phys. Fluids* 8, pp. 2182-2189.
20. Hirt, C.W. and Nichols, B.D. (1981). "Volume of Fluid (VOF) Method for the Dynamics of Free Boundaries", *Journal of Comp. Phys.*, Vol.399, pp.201.
21. Kaneko, S. and Ishikawa, M. (1999). "Modeling of Tuned Liquid Damper with submerged nets", *Journal of Pressure Vessel Technology*, Vol. 121, pp. 334-341.
22. Kanok W. and Tam B.T. (1999). "Structure Fluid Interaction Model of Tuned Liquid Dampers", *International journal of numerical method in engineering*, Vol. 46, pp. 1541-58.
23. Kareem, A. and Sun, W.J. (1987). "Stochastic response of structures with fluid containing appendages", *Journal of Sound and Vibration*, Vol. 21, pp.389-408.
24. Kareem, A. and Kijewski, T. (1999). "Mitigation of motions of tall buildings with specific examples of recent applications", *Wind and Structures* 2(3): 201–2511.
25. Koh, C.G., Mahatma, S., Wang, C.M. (1994). "Theoretical and experimental studies on rectangular liquid dampers under arbitrary excitations", *Earthquake Engineering and Structural Dynamics*, Vol. 23, pp. 17-31.
26. Kothe, D.B., Mjolsness, R.C., Torrey, M.D (1994), "A computer program for incompressible flows with free surfaces", LA-12007-MS, Los Alamos National Laboratory.
27. Kothe, D.B. and Rider, W.J. (1996). "Volume Tracking of Interface Having Surface Tension in Two and Three Dimensions", *AIAA Journal*, Vol.96-0859.
28. Lemos C.M. (1992). "Wave breaking: A numerical study", *Lecture notes in engineering*.
29. Lepelletier, T.G. and Raichlen, F. (1988). "Nonlinear oscillations in rectangular tanks", *Journal of Engineering Mechanics*, Vol. 114, pp. 1-23.
30. Lin Pengzhi, (2007). "A fixed grid model for simulation of moving body in free surface flows", *Computers & Fluids*, Vol. 36, pp. 549-561.
31. Lin Pengzhi and Liu Philip L. F. (1997). "A numerical model for breaking waves: The volume of fluid method", *Technical Report*, University of Delaware, Center for applied coastal research..
32. Matsuuara, Y., Matsumoto, K., Mizuuki, M., Arima, K., Jouuchi, H., Hayashi, S. (1986). "On a mean to reduce excited vibration with the sloshing in a tank", *J. Soc. Naval. Architecture Japan*, Vol. 160, pp. 424-32.
33. Min Soo Kim. (2003). "A new VOF-based numerical scheme for the simulation of fluid flow with free surface. Part I & II: New free surface-tracking algorithm and its verification", Vol. 42, issue 7, pp. 765-812.
34. Nakayama, T. (1983). "Boundary element analysis of nonlinear water wave problems", *International Journal for Numerical Methods in Engineering*, Vol. 19, p. 953.
35. Nakayama, T. and Washizu, K. (1981). "The boundary element method applied to the analysis of two-dimensional nonlinear sloshing problems", *International Journal for Numerical Methods in Engineering*, Vol. 17, pp. 1631-46.
36. Nichols, B.D., Hirt, C.W., Hotchkiss, R.S. (1985). "SOLA-VOF: A solution algorithm for transient fluid flow with multiple free boundaries", LA-8355, Los Alamos National Laboratory.
37. Noji, T., Yoshida, H., Tatsumi, E., Kosaka, H., Hagiuda, H. (1988). "Study on vibration control damper utilizing sloshing of water", *Journal of Wind Engineering*, No. 37, pp. 557-566.
38. Ohyama, T. and Fujii, K. (1989). "A boundary element method analysis for two-dimensional nonlinear sloshing problem", *JSCE Journal of Structural Engineering*, Vol. 35A, pp. 575-584.

39. Paz M., 1980, "Structural dynamics, theory and computation", 3<sup>rd</sup> edition, Chapman and Hall: U.S.A
40. Poo J.Y and Ashgriz N. (1990). "FLAIR – Flux line segment model for advection and interface reconstruction", *Journal of computational physics*, Vol. 93, issue 2, pp. 449-468.
41. Raad P. E, Johnson D. B., Chen S. (1994). "Simulation of Impacts of Fluid Free Surfaces with Solid Boundaries", *International Journal for Numerical Methods in Fluids*, Vol. 19, pp. 153-176.
42. Ramaswamy, B., Kawahara, M., Nakayama, T. (1986). "Lagrangian finite element method for the analysis of two-dimensional sloshing problems", *International Journal for Numerical Methods in Fluids*, Vol. 6, pp. 659-670.
43. Ronald B. Stull. (1988). "An Introduction to Boundary Layer Meteorology", Dordrecht; Boston, Kluwer Academic Publishers.
44. Reed, D., Jinkyu Y., Harry, Y. (1998). "Investigation of Tuned Liquid Dampers under Large Amplitude Excitation", *Journal of Engineering Mechanics*, ASCE, Vol. 124:4, pp. 405 -413.
45. Rider, W.J. (1998). "Reconstructing Volume Tracking", *Journal of Computational Physics*, Vol.141, pp.112-152.
46. Rudman, M. (1997). "Volume tracking methods fro interfacial flow calculations", *International Journal for Numerical Methods in Fluids*, Vol.24, pp.671-691.
47. Scardovelli, R. and Zaleski, S. (1999). "Direct numerical simulation of free-surface and interfacial flow" *Annual Review of Fluid Mechanics*, Vol.31, pp.567–603.
48. Shimizu, T. and Hayama, S. (1987). "Nonlinear Response of Sloshing Based on the Shallow Water Wave theory", *JSME International Journal*, Vol. 30: 263, pp. 806-813.
49. Siddique M.R., Hamed M.S., El Damatty A.A. (2004). "A nonlinear numerical model for sloshing motion in tuned liquid dampers", *International Journal for Numerical Methods in Heat & Fluid Flow*, Vol. 15 No. 3, pp. 306-324.
50. Soong T.T. and Dargush G.F. (1997). "Passive energy dissipation systems in structural engineering", John Wiley.
51. Sun L.M. (1991). "Semi-Analytical Modeling of Tuned Liquid Damper (TLD) with Emphasis on Damping of Liquid Sloshing", Ph.D. Thesis, University of Tokyo.
52. Sun, L.M. and Fujino, Y. (1994). "A semi-analytical model for tuned liquid damper (TLD) with wave breaking", *Journal of Fluids and Structures*, Vol. 8, pp. 471-88.
53. Sun, L.M., Fujino, Y., Koga, K. (1995). "A model of tuned liquid damper for suppressing pitching motions of structure", *Earthquake Engineering and Structural Dynamics*, Vol. 24, pp. 625-36.
54. Sun, L.M., Fujino, Y., Chaiseri, P. and Pacheco (1995). "The Properties of Tuned Liquid Dampers using a TMD Analogy", *Earthquake engineering and structural dynamics*, Vol. 24, pp. 967-976.
55. Sun, L.M., Fujino, Y., Pacheco, B.M., Isabe, M. (1989). "Nonlinear waves and dynamic pressures in rectangular TLD-simulation and experimental verification", *Journal of Structural Engineering and Earthquake Engineering*, Vol. 6, pp. 251-62, Proc. JSME.
56. Tamura, Y., Fujii, K., Obtsuki, T., Wakahara, T., Kohsaka, R. (1995). "Effectiveness of Tuned Liquid Dampers under wind excitations", *Engineering Structures*, Vol. 17, No. 9, pp. 609-621.
57. Tait, M. (2004). "The Performance of 1-D and 2-D tuned Liquid Dampers", Ph.D. Thesis. University of Western Ontario, London, Canada.

58. Tait, M., El Damatty, A.A., Isyumov, N. (2005). "An Investigation of tuned liquid dampers equipped with damping screens under 2D excitation", *Earthquake Engineering and Structural Dynamics*, Vol. 34, pp. 719-735.
59. Tait, M., El Damatty, A.A., Isyumov, N. (2005). "Effectiveness of a 2D TLD and its numerical modeling", *Journal of structural engineering*, Vol. 34, pp. 79-96.
60. Tait, M., El Damatty, A.A., Isyumov, N., Siddique, M.R. (2005). "Numerical Flow Models to Simulate Tuned Liquid Dampers (TLD) with Slat Screens", *Journal of Fluids and Structures*, Vol. 20, No. 8, pp. 1007-1023.
61. Tavakoli R., Babaei R., Varahram N. (2006). "Numerical simulation of liquid/gas phase flow during mold filling", *Computational methods and its application in mechanical engineering*, Vol.196, pp.697-713.
62. Thé J.L, Raithby G.D, Stubble G.D. (1994). "Surface adaptive finite volume method for solving free surface flows", *Numerical Heat Transfer*, Vol. 26(B), pp. 367-80.
63. Torrey M. D., Cloutman L. D., Mjolsness R. C., Hirt C. W. (1986). "NASA-VOF2D: a computer program for incompressible flows with free surfaces", LA-10612-MS, Los Alamos National Lab..
64. Tosaka, N. and Sugino, R. (1991). "Boundary element analysis of potential flow with nonlinear free surface", *Proceedings of the 4th China-Japan Symposium on Boundary Element Methods*, pp. 137-144.
65. Ubbink O. (1997). "Numerical prediction of two fluid systems with sharp interface", PhD Thesis, Imperial college, London. U.K.
66. Vandiver, J.K. and Mitone, S. (1978). "Effect of liquid storage tanks on the dynamic response of offshore platforms", *Applied Ocean Research*, Vol. 1, pp. 67-74.
67. Wakahara, T., Ohyama, T., Fujii, K. (1992). "Suppression of wind-induced vibration of a tall building using tuned liquid damper", *Journal of Wind Engineering and Industrial Aerodynamics*, Vol. 41-44, pp. 1895-906.
68. Wakahara, T. (1993). "Wind-induced response of TLD-structure coupled system considering non-linearity of liquid motion", *Shimizu Tech. Res. Bull.*, Vol. 12, pp. 41-52.
69. Warnitchai P. and Pinkaew T. (1998). "Modeling of liquid sloshing in rectangular tanks with flow-dampening devices", *Engineering Structures*. Vol. 20: 7, pp. 593-600.
70. Yamamoto K, Kawahara M. (1999). "Structural oscillation control using tuned liquid damper", *Computers and Structures*, Vol. 71, pp. 435-446.
71. YU J.K. (1997). "Nonlinear characteristics of Tuned Liquid Damper", PhD thesis, University of Tokyo, Tokyo, Japan.
72. Zang, Y., Xue, S. and Kurita, S. (2000). "A boundary element method and spectral analysis model for small-amplitude viscous fluid sloshing in couple with structural vibrations", *International Journal for Numerical Methods in Fluids*, Vol. 32, pp. 79-96.

**Morteza Marivani**

#2601 – 153 Beecroft Rd, Toronto, ON M2N 7C5

[marivam@mcmaster.ca](mailto:marivam@mcmaster.ca),**PROFILE:**

- Over 10 years experience in CFD analysis both in algorithm development and using commercial CFD software in automotive industry
- Advanced knowledge in Fluid Mechanics, Heat Transfer and CFD
- Proficient in Cfdesign, Star-CD and Star-Design software
- Strong knowledge at Fortran and Pascal programming
- Experienced in Inventor, Hypermesh, Fluent, Catia, , Autocad
- Proficient in standard office applications: Excel, PowerPoint and Word
- Completed Master's degree in fluid mechanics engineering
- Hard working, Team player, Self-starter, Reliable, Organized

**EXPERIENCE:****2003- 2009 PhD Candidate****McMaster University, Mechanical Engineering Dept, Hamilton, Canada**

- Developed a numerical algorithm to simulate the behavior of the fluid sloshing motion inside a Tuned Liquid Damper (TLD) system in the presence of submerged screens.
- Introduced new formulation to calculate the pressure drop of slat screens.
- Developed a numerical algorithm to solve Navier-Stokes and Energy equations in body-fitted coordinate system to simulate flow and thermal fields in complex geometries
- Published several journal and conference papers.
- Teaching assistance of the following courses: Fluid Mechanics, Compressible and incompressible flow, Thermo-Fluid systems design and analysis.

**1996 – 2002 Research & Development Engineer, IKCO Industrial Group,  
Research and Development Center**

- Provided thermal analysis of engine cooling system through climatic wind tunnel testing and performed modification to air-inlet duct.
- Administered external flow analysis of a new car through CFD analysis and full-scale wind tunnel testing.
- Designed and performed modification to the defrost system using Defrost analysis of STAR-CD, climatic wind tunnel testing and using thermal imaging camera.
- Performed HVAC system and Climatic Control Analysis of a new model car using CFD analysis of STAR-CD and climatic wind tunnel testing.
- Implemented of an in-house general CFD code to simulate three- dimensional turbulent flows on complex geometries using general curvilinear coordinate system including solver and grid generation.
- Designed and performed modification to wheel covers through experimental data and full scale wind tunnel testing.

- Responsible for surface modeling of various parts for new designed car with CADD5 and CATIA.
- Liaison engineer between IKCO design department and fluid department of MIRA Ltd.
- Provided analysis reports based on CFD analysis results for evaluation of design specifications.

### **EDUCATION:**

- 2003 – 2009 PhD in Mechanical Engineering, McMaster University**  
(Specializing in Computational Fluid Dynamics)
- 1996 - 1998 M. Sc. in Mechanical Engineering**  
(Specializing in Computational Fluid Dynamics)
- 1987 - 1992 B. Sc. in Mechanical Engineering**  
(Specializing in Aerodynamics and Propulsion systems)

### **ACCOMPLISHMENTS:**

- Scholarship from McMaster University during the PhD program.
- Completed all required PhD courses with A+
- Dean's honor role in Master's degree.
- Award for outstanding graduate student, February 1999.
- Dean's honor role in Bachelor's degree.
- Award for outstanding student, August 1992.

### **SELECTED PUBLICATIONS:**

1. **Marivani M., Hamed M.,** Numerical Simulation of Structure Response Outfitted with a Tuned Liquid Damper, Computers and Structures, 2009.
2. **Marivani M., Hamed M.,** Numerical Modeling of Sloshing Motion in Tuned Liquid Dampers Outfitted with Submerged Slat Screens, International Journal for Numerical Methods in Fluids, 2009.
3. **Marivani M., Morsy H., Hamed M.,** Effect of A Tuned Liquid Damper Screen Configuration on Structure Response, Proceedings of ICFDP9: Ninth International Congress of Fluid Dynamics & Propulsion, December 18-21, 2008, Alexandria, Egypt
4. **Marivani M. , Morsy H., Hamed M.,** On the Dynamic Response of Structures Equipped with Tuned Liquid Dampers, Proceedings of the Fourth International Conference on, Thermal Engineering: Theory and Applications, January 12-14, 2009, Abu Dhabi, UAE.
5. **Marivani M., Hamed M.,** Numerical Investigation of the effect of screen pattern on the performance of TLD equipped by slat screens, 2009, submitted.
6. **Marivani M., Hamed M.,** New correlation factor for calculation of pressure drop at the slat screens used in the Tuned Liquid Damper, 2009, submitted.

### **REFERENCES:**

- Available Upon Request